

Extending the Scope of the Density Overlap Region Indicator

THÈSE N° 8157 (2018)

PRÉSENTÉE LE 16 JANVIER 2018

À LA FACULTÉ DES SCIENCES DE BASE

LABORATOIRE DE DESIGN MOLÉCULAIRE COMPUTATIONNEL

PROGRAMME DOCTORAL EN CHIMIE ET GÉNIE CHIMIQUE

ÉCOLE POLYTECHNIQUE FÉDÉRALE DE LAUSANNE

POUR L'OBTENTION DU GRADE DE DOCTEUR ÈS SCIENCES

PAR

Laurent Alexis Clément VANNAY

acceptée sur proposition du jury:

Prof. M. Dal Peraro, président du jury
Prof. A.-C. Corminboeuf, directrice de thèse
Prof. C. Daul, rapporteur
Dr D. Tiana, rapporteur
Prof. V. Hatzimanikatis, rapporteur



ÉCOLE POLYTECHNIQUE
FÉDÉRALE DE LAUSANNE

Suisse
2018

It is by logic that we prove,
but by intuition that we discover
J.H.Poincaré

To my family

Acknowledgements

I thank my advisor, Prof. Clémence Corminboeuf, for her constant availability and swift feedbacks to my scientific work. Her advises greatly helped my navigation in computational chemistry, and her permanent hard work was a model, in particular during the frustrating phases of scientific researches. The time she spent in improving the writing of this thesis notably influenced the final manuscript. All the members of the Laboratory for Computational Molecular Design were always supportive, in particular the scientists and post-Docs. Every day, we could argue about our ideas and share enthusiasm about our latest results. I am grateful to Matt for his help with organometallic chemistry and English wording. Piotr, thank you for developing DORI, and for helping me getting familiar with it. Jérôme and Eric, this thesis would not have been possible without your patience and efficient mentoring at its start. Thank you Anya for the insightful scientific discussions and mediations we prepared together. Ewa, Adrien, Jian-Hao, Stepan, and Giulia, thank you for sharing your different backgrounds and perspectives on computational chemistry, which helped to keep an open mind when facing new problems. It was a pleasure to share the daily life with the other PhD of the LCMD crew. Antonio, your efficiency remains inspiring, Riccardo, keep your positive attitude, Alberto, thanks for the super presentations, and Kun-Han, continue to be passionate for science and food. Raimon and Veronica, I wish you both to achieve your PhD goals! Thanks Daniel, both for maintaining the computers in good shape and for the insights you gave on bash scripting and software compilation. Benjamin, thank you for sharing your apparently unlimited motivation to overcome challenges, in science and real life alike. Your friendship was a great support, especially in the late stages of the thesis. Véronique, I really appreciated our conversations and the encouragements you provided. Durant ces années, j'ai profité du soutien de nombreuses personnes extérieures à l'EPFL. Je remercie ma famille pour m'avoir permis de faire des études supérieures et pour la motivation qu'elle a su me transmettre. Merci aux membres du club de Rock'n Roll acrobatique de Neuchâtel et de Lausanne, Bastien, Cindy, Raphaël, Angelo et Yolanda, votre coaching et votre amitié m'ont permis de décompresser, d'apprendre à monter sur scène, et à interioriser mes peurs pour briller aux moments importants de la vie. Joëlle, tu as toujours su me montrer la beauté du monde qui nous entoure, et ton amour inconditionnel était le meilleur moteur que je puisse avoir pour traverser cette étape de ma vie. I am also grateful to Vassily Hatzimanikatis, Claude Daul and Davide Tiana for having accepted to be on my jury. Finally, the Swiss NSF Grant 156001, and EPFL are respectfully acknowledged for their financial support.

Lausanne, 30 Novembre 2017

Abstract

In this thesis, original applications of the Density Overlap Region Indicator (DORI), a density dependent bonding descriptor capable of simultaneously capturing covalent and non-covalent interactions, are discussed. The use of scalar fields, such as DORI, were generally restricted to visualizing bonding situations in static gas phase molecules. Here, DORI is pushed out of its comfort zone and used to probe systems prone to electronic and geometric fluctuations, or those constrained by their condensed phase environments. The applications to challenging chemical systems highlighted within demonstrate the capabilities of DORI as a formidable tool that can be beneficial in many facets of chemistry.

Molecules in the excited state are difficult to analyze using popular bonding descriptors, primarily because the required information (orbitals) are not given by standard computational methodologies. DORI, which relies exclusively on the electron density and its derivatives, overcomes previous limitations and permits the characterization of excitation processes (charge transfer, excimer, Rydberg, ...) through visual and numerical signatures. Using DORI, the evolution of covalent and non-covalent excited state interactions were used to rationalize photoemission in BODIPY-derivatives. Certain BODIPY substituents form non-covalent intramolecular interactions in the excited state, which are crucial for stabilizing the $S_x - S_0$ intersection and prompting nonradiative decay. This application demonstrates that DORI is ideally suited for characterizing excited state phenomena.

Dynamical fluctuations represent another domain beyond the standard usage of bonding descriptors. Highly fluxional molecules, such as molecular machines or proteins, have complex multi-dimensional conformational spaces that are generally explored using a handful of geometrical collective variables (bond lengths, angles, etc.), or dimensionality reduction algorithms. DORI's covalent and non-covalent patterns are exploited as alternative sets of descriptors, which are simpler than geometrical parameters because electronic and geometrical fluctuations can be captured by a single-dimensional variable. DORI is also synergistically used alongside dimensionality reduction algorithms to reveal enhanced descriptions of the conformational spaces of a molecular rotor and a photoswitch. Thus, cost effective bonding descriptors are well adapted and beneficial in analyzing electronic and geometrical fluctuations requiring extended mapping of conformational spaces.

Finally, DORI allows for simultaneous visualization of covalent and non-covalent interactions, and is thus particularly suited to investigate their interplay, notably present in dense environments of high-pressure crystals and in protein-ligand cavities. Using actual experimental electron densities of an organic crystal, DORI exposes pressure-induced disruptions of intramolecular delocalization and identifies the directional non-covalent interactions that cause

Abstract

these perturbations. Similarly, the scalar field pinpoints the specific non-covalent protein-ligand interactions which modify the covalent regions of the ligand and facilitate the reactive process.

Overall, the examples presented in this thesis demonstrate the versatility of DORI in translating complex chemical behavior into intuitive representations, greatly extending the range of applications that benefit from visual bonding descriptors.

Key words: molecular scalar field; bonding descriptor; covalent interactions; non-covalent interactions; electron density analysis

Résumé

Cette thèse présente des applications originales du Density Overlap Region Indicator (DORI), un descripteur de liaison basé sur la densité électronique qui capture simultanément les interactions covalentes et non-covalentes. L'utilisation des champs scalaires tels que DORI est habituellement restreinte aux molécules statiques, en phase gazeuse. Ici, DORI est sorti de sa zone de confort pour inspecter des molécules exposées à des fluctuations électroniques et géométriques, ou à des contraintes de leur environnement. Ces applications démontrent que DORI est un outil formidable pouvant être profitable pour de nombreux domaines de la chimie.

Les molécules à l'état excité sont difficiles à analyser avec les descripteurs de liaisons populaires, notamment parce que les méthodes computationnelles ne délivrent pas les informations nécessaires (les orbitales). DORI, qui repose sur la densité électronique et ses dérivées, n'a pas ce problème et permet la caractérisation des types d'excitations (transfert de charge, excimer, Rydberg, ...) en se basant sur des signatures visuelles et numériques. À travers DORI, les propriétés photoémisives de molécules dérivées de BODIPY sont rationalisées en suivant l'évolution des interactions chimiques à l'état excité. Certains substituants forment des interactions intramoléculaires non-covalentes à l'état excité, qui stabilisent l'intersection $S_x - S_0$, déclenchant une désexcitation non-radiative. Ces applications prouvent que DORI est idéal pour la caractérisation des phénomènes à l'état excité.

Les fluctuations dynamiques sont également peu analysées par les descripteurs de liaisons. Les molécules très fluxionnelles, comme les machines moléculaires ou les protéines, ont des espaces conformationnels multidimensionnels qui sont souvent explorés en utilisant quelques variables géométriques (longueur de liaison, angle, *etc.*), ou des algorithmes de réduction de dimensionnalité. Les reliefs de DORI sont exploités comme des descripteurs alternatifs, qui s'avèrent plus simples que les paramètres géométriques puisque les fluctuations géométriques et électroniques sont capturées dans une seule variable. DORI est également utilisé en synergie avec les algorithmes de réduction de la dimensionnalité, montrant de meilleures descriptions de l'espace conformationnel d'un rotor moléculaire et d'un photoswitch. Ainsi, les champs scalaires sont adaptés et bénéfiques pour l'analyse des fluctuations électroniques et géométriques nécessitant une cartographie des espaces conformationnel.

Enfin, puisque DORI offre une visualisation simultanée des interactions covalentes et non-covalentes, il est particulièrement adapté pour examiner leurs interrelations, qui sont remarquables dans les environnements denses tels que les cristaux sous haute pression et les cavités protéine-ligands. En exploitant les densités expérimentales d'un cristal organique sous pression, DORI expose les ruptures dans le schéma de délocalisation, et identifie les interactions

Résumé

non-covalentes directionnelles qui causent ces perturbations. De même, le champ scalaire met en exergue les interactions non-covalentes entre la protéine et son ligand qui modifient la région covalente du ligand et facilitent le processus réactionnel. Tous ces exemples démontrent la versatilité de DORI pour traduire des comportements chimiques complexes en représentations intuitives, élargissant considérablement le champ d'application possible des descripteurs visuels.

Mots-clefs : champs scalaires moléculaires ; descripteurs de liaison ; interactions covalentes ; interaction non-covalentes ; analyse de la densité électronique

Contents

| | |
|--|------------|
| Acknowledgements | i |
| Abstract (English/Français) | iii |
| List of figures | ix |
| 1 Introduction | 1 |
| 2 Characterization of Chemical Interactions Using Molecular Scalar Fields | 5 |
| 2.1 Localization Functions | 7 |
| 2.1.1 Lodges Theory | 7 |
| 2.1.2 Electron Localization Function (ELF) | 7 |
| 2.1.3 ELF Applications | 9 |
| 2.1.4 ELF Limitations and Remedies | 10 |
| 2.1.5 ELF and Correlated Wavefunctions | 11 |
| 2.1.6 Domain-Averaged Fermi Holes (DAFH) | 12 |
| 2.1.7 Kinetic Energy Density | 12 |
| 2.2 Capturing Non-covalent Interactions | 13 |
| 2.3 Conclusion | 15 |
| 3 DORI | 17 |
| 3.1 Single Exponential Decay Detector (SEDD) | 17 |
| 3.2 Density Overlap Region Indicator (DORI) | 18 |
| 3.2.1 DORI[f] Domains | 19 |
| 3.2.2 Intramolecular Bonding | 20 |
| 3.2.3 Intermolecular Interactions | 21 |
| 3.2.4 Effects of Basis Sets and Computational Methods | 21 |
| 3.2.5 DORI Applications | 22 |
| 4 Visualizing and Quantifying Interactions in the Excited State | 25 |
| 4.1 Introduction | 25 |
| 4.2 Computational Details | 28 |
| 4.3 Results and Discussion | 28 |
| 4.3.1 Molecular Excitations | 28 |
| 4.3.2 Excited-state Complexes | 30 |

Contents

| | | |
|----------|---|-----------|
| 4.4 | Conclusion | 35 |
| 4.5 | Fluorescence Quenching in BODIPY Dyes | 36 |
| 5 | Analyzing Fluxional Molecules using DORI | 39 |
| 5.1 | Introduction | 39 |
| 5.2 | Computational Details | 42 |
| 5.3 | Results and Discussion | 44 |
| 5.3.1 | Thieno-[2,3-b]-thiophene | 44 |
| 5.3.2 | Molecular Rotor | 46 |
| 5.3.3 | Photochromic Torsional Switch | 48 |
| 5.4 | Conclusion | 50 |
| 6 | The Interplay between Covalent Bonding Patterns and Non-Covalent Interactions in Biscarbonyl[14] Annulene under Pressure | 51 |
| 6.1 | Introduction | 51 |
| 6.2 | Computational Details | 54 |
| 6.3 | Results and Discussions | 55 |
| 6.4 | Conclusions | 60 |
| 6.5 | Proteins Exploit Non-covalent - Covalent Interplays | 60 |
| 6.6 | DORI Assessing Electron Densities | 61 |
| 7 | Conclusions and Outlooks | 63 |
| A | Topological analysis in chemistry | 67 |
| B | Supplementary Information for Visualizing and Quantifying Interactions in the Excited State | 71 |
| C | Supplementary Information for Analyzing Fluxional Molecules using DORI | 77 |
| D | Supplementary Information for DORI Assessing Electron Densities | 81 |
| | Bibliography | 83 |
| | Curriculum Vitae | 99 |

List of Figures

| | | |
|-----|--|----|
| 2.1 | Isosurface of $ELF = 0.85$ for thiophene (left) and water dimer (right). | 9 |
| 2.2 | NCI=0.6 isovalue for a thiophene dimer (left) and a water dimer (right), color coded with the $sgn(\lambda_2)\rho(\mathbf{r})$ | 14 |
| 3.1 | Three-dimensional representation of SEDD=3 isovalue for thiophene (left) and NH_3 (right). | 18 |
| 3.2 | Main DORI bifurcation values for the CF_4 molecule. | 19 |
| 3.3 | DORI in-plane representation of a selection of small molecules: C_2H_6 (a), C_2H_4 (b), C_2H_2 (c), N_2 (d), O_2 (e), C_2F_4 (f), $\text{C}_4\text{H}_4\text{S}$ (g), computed on electron densities optimized at the PBE0/cc-pVTZ level. | 20 |
| 3.4 | DORI=0.9 isovalue for a thiophene dimer (left) and a water dimer (right), color coded by the $sgn(\lambda_2)\rho(\mathbf{r})$ | 21 |
| 3.5 | DORI in-plane representation of the C_2H_4 molecule using proatomic densities (a), BLYP (b), B3LYP (c), MP2 (d) and a cc-pVTZ basis set (top). B3LYP densities computed with different basis sets: STO-3G (e), cc-pVDZ (f), cc-pVTZ (g), cc-pVQZ (h) (bottom). All computations exploit B3LYP/cc-pVTZ optimized geometries. | 22 |
| 4.1 | Two-dimensional ground-state DORI maps of the argon atom (left) and in the σ_h plane of the ethene molecule (middle). Three-dimensional representation of the ground-state DORI for the parallel-displaced benzene dimer (right) plotted for $\text{DORI}[S_0]=0.95$. DORI computation uses a density self-consistently optimized at the B3LYP/TZP level. | 27 |
| 4.2 | DORI=0.85 isosurface and $\text{DORI}_{int}({}^1S_n; V_{0.85})$, $n \in \{0, 1, 2, 3\}$ for the pyrrole in its ground and the first three (Rydberg) excited-state singlets computed at the (TD)-PBE0/TZVP-aug level on the $\omega\text{B97X-D/def2-SVP}$ ground state optimized geometries. The nitrogen atom position is indicated by “N”, and DORI_{int} for molecular (A) and Rydberg (Ry) basins are given in the figure. | 29 |

- 4.3 Two-dimensional ground (top left) and excited (top right) state DORI maps in the σ_h plane of the biphenylene molecule. Isocontour lines of $\text{DORI}[\rho] \in \{0.01, 0.50, 0.99\}$ are plotted in white. All the structures are optimized at the (TD-)B3LYP/TZP level, and the relaxed densities to compute DORI are obtained at the same level. Bottom left and bottom right Lewis structures represent the two schematic electronic delocalizations estimated according to the bond length patterns in the ground and excited state, respectively. Bond lengths for ground (excited) state (in Å): a=1.38 (1.43), b=1.42 (1.38), c=1.37 (1.40), d=1.42 (1.49), e=1.51 (1.41). 30
- 4.4 Three-dimensional representation of the excited-state DORI for an anthracene excimer plotted for $\text{DORI}[\rho_{S_1}]=0.7$ (left). Two-dimensional ground- and excited-state DORI maps obtained from relaxed S_0 , $S_1(1B_{2u})$ and $S_2(1B_{2g})$ (TD-)PBE0/TZP densities (right). The excimer geometry is optimized at the TD- ω B97X-D/def2-SVP level. 31
- 4.5 DORI maps in the intermolecular plane for the benzene (top), pyrene (middle), and perylene (bottom) dimers, using the (TD-)PBE0/TZP densities computed on the S_1 excimer ω B97X-D/def2-SVP optimized geometry. 32
- 4.6 Density differences ($\rho_{S_n} - \rho_{S_0}$, $n \in \{1, 2, 3\}$) at the PBE0/cc-pVDZ level for the excimer complexes in their first singlet excited-state TD- ω B97X-D/def2-SVP optimized geometry. Isodensities=+0.0005 (red) and -0.0005 (blue). 33
- 4.7 One-dimensional ground-state (ground and excited states) DORI maps for the ionic LiF (left) and charge-transfer benzene-TCNE complex (right) plotted along the C_n axis of the system. Relaxed densities to compute DORI are obtained at the (TD-)CAM-B3LYP/cc-pVDZ level (bottom): Superposition of $\text{DORI}[\rho]=0.9$ in S_1 excited state (red) and ground state (black) for the tetracyanoethylene-benzene dimer at the (TD-)CAM-B3LYP/cc-pVDZ level. The charge transfer is shown to induce a displacement of the DORI intermolecular basin towards the donor molecule. 34
- 4.8 $\Delta\text{DORI}_{int}=[\text{DORI}_{int}(\rho_{X_1}; V_{0.85}) - \text{DORI}_{int}(\rho_{S_0}; V_{0.85})] \cdot 1000$ in millielectron ($X=S, T$) in the schematic DORI regions for Iridium (Ir), acetylacetonate (acac), and 2-(2,4-difluorophenyl)pyridine (Fppy_{a,b}) (top). Density differences for the first singlet and optimized triplet excited states; isodensities=+ 0.002(red) and -0.002(blue) (bottom). The scalar fields were computed for absorption (left, $S_0 \rightarrow S_1$ in S_0 geometry) and emission (right, $T_1 \rightarrow S_0$ in the T_1 geometry) using the relaxed (TD-)CAM-B3LYP/cc-pVDZ densities. The complexes were optimized in the ground state and first triplet at the (TD-) ω B97X-D/def2-SVP level. 35
- 4.9 Three-dimensional DORI representation (isovalue=0.995) of *tert*-butyl-BODIPY in ground state minimum (top) and near the conical intersection (bottom) geometries. In the DORI isosurfaces blue represents attractive and red repulsive interactions. The shortest hydrogen – fluorine distance [Å] is indicated by a dashed line. Computations at the MP2/ADC(2) / def2-SVP level. 36

| | | |
|------|---|----|
| 4.10 | Two-dimensional DORI map of BODIPY in S_0 (left) and MECP (right) geometries. White contour lines (DORI=0.99) indicate the bonding pattern as being quasi-aromatic for the ground state, while the bond order is reduced in the excited state. Computations at the MP2/ADC(2)/def2-SVP level. | 37 |
| 5.1 | Three-dimensional representation of the benzene plotted for ELF= 0.8 (left), two-dimensional DORI maps in the σ_h plane of the butadiene with DORI=0.99 iso-contour in white (center) and three-dimensional representation of the parallel-displaced benzene dimer for DORI=0.95 (right). Electron densities are self-consistently optimized at the B3LYP/TZP level. | 39 |
| 5.2 | Three-dimensional representation of Thieno-[2,3-b]-thiophene (1), a molecular rotor (2) and a photochromic torsional switch (3). | 42 |
| 5.3 | Two-dimensional representation of the dithiacyclophane conformers color-coded with the integral of the electron density within the intramolecular DORI domain, $\text{DORI}_{int}[0.8]$. Conformers are extracted from the DFTB trajectory at 300K. The snapshots are described based on the distance between barycenters of the π -subsystems (R), and the angle between the two planes describing the π -systems (θ) mapped in the [0,90] range. Conformers are color-coded using the integral of electron density in the intramolecular basin. DORI values are computed on electron densities relaxed at the PBE/6-31G* level on frozen DFTB3/3OB-UFF MD geometries. | 44 |
| 5.4 | Structure occurrence based on integral of the electron density ($\text{DORI}_{int}[0.8]$) within the intramolecular DORI=0.8 domain of the truncated dithiacyclophane, computed on the structures extracted from the MD (left). $\text{DORI}_{int}[0.8]$ of two optimized geometries (static # 1, # 2), the average MD geometry, and mean of DORIs from the standard MD at 300K, and from REMD@DFTB3 ^{300K} . DORI are computed on electron densities relaxed at the PBE/6-31G* level, on DFTB3/3OB-UFF (MD) geometries. | 45 |
| 5.5 | Superimposed representations of the molecular rotor and its associated $\text{DORI}[0.8]$ (blue) computed on the model system (a). Ranges of $\text{DORI}_{vol}[0.8]$ values for a given stator - rotator interaction (rotator considered for scheme colored in red) (b). Simultaneous visualization of the $\text{DORI}_{vol}[0.8]$ of the basins stemming from the two stator-rotator interactions, (I) and (II) (c). DORI are computed on electron densities relaxed at the PBE/6-31G* level on frozen DFTB3/3OB-UFF MD geometries. | 47 |
| 5.6 | Sketch-map representation of the molecular rotor, color-coded with the sum of the $\text{DORI}_{vol}[0.8]$ volumes stemming from interactions between the two stators and the rotator. | 48 |

List of Figures

| | | |
|-----|---|----|
| 5.7 | Representations of the photochromic torsional switch and its associated $DORI_{\pi}[0.9]$ (in blue) for the inter-thiophene bond (left). Correlation of the $DORI_{\pi int}[0.99]$ with the inter-thiophene bond distance (R) and the inter-thiophene \angle SCCS dihedral angle (θ), mapped in the [0,180] range. DORI are computed on electron densities relaxed at the PBE/6-31G(d) level on frozen DFTB3 / 3OB-UFF geometries from REMD. | 49 |
| 5.8 | Sketch-map representation of the photochromic torsional switch 3 , forming two distinct zones corresponding to the Z- and E-azobenzene configuration (left and right respectively). The map is color-coded with the electron density integral stemming from the $DORI_{\pi}[0.99]$ basins of the dithiophene bridging bond (a), and with the free energy computed from the molecular dynamics occurrences (b). | 50 |
| 6.1 | Conceptual Lewis representation of the syn-1,6:8,13-biscarbonyl[14] annulene at ambient and at high pressure. | 54 |
| 6.2 | Three superimposed two-dimensional DORI maps of the biscarbonyl [14] annulene (top, color-code from DORI=0 (red) to DORI=1 (blue)). DORI = 0.999 isosurfaces (blue) of the biscarbonyl [14] annulene (bottom). Both representations are given for ambient (left) and high pressure (7.7GPa, right). | 56 |
| 6.3 | Integral of the experimental electron density [a.u.] inside C-C bonding basin of the BCA molecule at ambient (blue) and high pressure (red), enclosed in the DORI=0.999 isosurfaces. | 57 |
| 6.4 | BCA geometry (a), DORI=0.995 isosurfaces displaying the network of non-covalent interactions of one single BCA molecule in crystal environment at ambient (b) and high pressure (c). Van der Waals interactions colored in blue, CH-O in red, and intramolecular in yellow. | 58 |
| 6.5 | DORI=0.999 isosurfaces capturing the CH-O interactions of one single BCA molecule in crystal environment at and high pressure. Red arrow pinpointing out-of-plane interactions. | 59 |
| 6.6 | DORI=0.9 isosurfaces color-coded with $sgn(\lambda_2)\rho(r)$ ranging from -0.02 au (red, attractive) to +0.02 au (blue, repulsive). The electron densities and binding energies (E_{bind} [kcal/mol]) between the glycine residue and the dimethylhistidine (for DMH and DMH_SAH), and the trimethylhistidine (TMH) were computed at the PBE0-dDsC/TZP level. Iterative Hirshfeld charges on nitrogen are depicted in the presence (left) or absence (right) of the Gly161 residue. | 61 |
| 6.7 | Mesh to mesh Euclidian distances [au] between DORI=0.6 isosurfaces of the BCA using DORI computed on the experimental electron density as a reference. | 62 |
| A.1 | Isosurface of $\nabla^2\rho(\mathbf{r}) = -0.4$ (left) and QTAIM colored by basins for the thiophene molecule (right) | 68 |

| | | |
|------|---|----|
| B.1 | (top) Canonical orbitals participating to the S_1 - S_3 singlet excitations (isovalues= ± 0.02), (center) DORI map in the molecular plane, (bottom) electron gain regions after excitation based on the relaxed electron density difference ($\rho(S_n) - \rho(S_0)$) computed at the (TD-)PBE0/def2-TZVP-aug level (isovalue= $+0.0005$ a.u.) on the ground state ω B97X-D/cc-pVDZ optimized geometry. | 71 |
| B.2 | (Top) DORI map in the π -region (0.5\AA below the molecular plane) for biphenylene at the (TD-)B3LYP/TZP level in the B3LYP/TZP ground state geometry for the ground (left) and first singlet excited state (right). Bottom: Lewis structures based on DORI behavior | 72 |
| B.3 | (Top) Orbitals participating to the S_1 - S_3 singlet excitations (isovalues= ± 0.03) and (bottom) DORI maps in intermolecular plane for the anthracene-anthracene dimer at the (TD-)PBE0/TZP level in its S_1 excimer TD- ω B97X-D/def2-SVP optimized geometry. | 72 |
| B.4 | Excitation energies, oscillator strengths, orbital contributions and representations (isovalue= ± 0.02) at the TD-CAM-B3LYP for the first three singlet excitations using a cc-pVDZ basis set for the tetracyanoethylene-benzene charge transfer complex in its ground state ω B97X-D/def2-SVP optimized geometry. | 72 |
| B.5 | Excitation energies, oscillator strengths, orbital contributions and representations (isovalue= ± 0.02) at the TD-CAM-B3LYP for the first three singlet excitations using a cc-pVDZ basis set for the tetracyanoethylene-naphthalene charge transfer complex in its ground state ω B97X-D/def2-SVP optimized geometry. | 73 |
| B.6 | Excitation energies, oscillator strengths, orbital contributions and representations (isovalue= ± 0.02) at the TD-CAM-B3LYP for the first three singlet excitations using a cc-pVDZ basis set for the tetracyanoethylene-anthracene charge transfer complex in its ground state ω B97X-D/def2-SVP optimized geometry. | 73 |
| B.7 | Density differences ($\rho_{S_n} - \rho_{S_0}$, $n \in \{1, 2, 3\}$) at the (TD-)CAM-B3LYP/ccpVDZ level for (top) benzene-TCNE (isovalue= 0.005), (middle) naphthalene- TCNE (isovalue= 0.005), and (bottom) anthracene-TCNE (isovalue=0.0015). Positive values in red, negative in blue. | 74 |
| B.8 | Transition energy, oscillator strength and orbital contribution for the singlet excitations for the FIr(acac) complex at the TD-CAMB3LYP/cc-pVDZ LANL2DZ level in the ground state and triplet (TD-) ω B97X-D/def2-SVP LANL2DZ optimized geometry | 74 |
| B.9 | Orbital representations (isovalue= ± 0.04) at the CAM-B3LYP level for the first singlet excitation using a cc-pVDZ and LANL2DZ basis set (Ir) for the FIr(acac) complex in its ground state ω B97X-D/def2-SVP optimized geometry | 75 |
| B.10 | Orbital representations (isovalue= ± 0.04) at the CAM-B3LYP level for the first triplet excitation using a cc-pVDZ and LANL2DZ basis set for the FIr(acac) complex in the TD- ω B97XD/def2-SVP optimized T_1 geometry | 75 |

List of Figures

| | | |
|-----|---|----|
| C.1 | Three dimensional representation of Thieno-[2,3-b]-thiophene (1), the molecular rotor (2) and the photochromic torsional switch (3). Molecular dynamics trajectories were run on full systems (a), DORI was computed on truncated systems (b), to accelerate the DORI analysis. | 77 |
| C.2 | All sixteen AdNDP π -orbitals of the PTS system used for DORI π computations. Orbital order is arbitrary within AdNDP framework. | 78 |
| C.3 | Integral of the electron density (DORI _{int} [0.8]) within the intramolecular DORI=0.8 domain of the truncated dithiocyclophane, for all 54 MD trajectories merged together. DORI are computed on electron densities relaxed at the PBE/6-31G* level, on frozen DFTB3/3OB-UFF MD geometries. | 79 |
| D.1 | Mesh to mesh Euclidian distances [au] between DORI=0.6 isosurfaces of the 3-acetylcoumarin using DORI computed on the experimental electron density as a reference. | 81 |
| D.2 | Mesh to mesh Euclidian distances [au] between DORI=0.6 isosurfaces of the tetrafluoroterephthalonitrile using DORI computed on the experimental electron density as a reference. | 82 |

1 Introduction

The behavior of electrons governs chemical interactions between atoms and molecules. The Schrödinger equation provides the theoretical foundation for describing electronic structures. However, this equation is solvable analytically only for few simple systems. To model realistic chemical or biological systems of interest, theoretical chemistry offers a range of powerful approximations, such as Density Functional Theory (DFT), or the extended family of post-Hartree-Fock methods. These starting points enable chemists to investigate the intricate quantum behavior of electrons not only in the static structures in the gas phase, but also in conjunction with the dynamical treatment of nuclei, condensed phases effects, or molecules under perturbation by external fields (*e.g.*, light).

Considerable advances in computer science, including both the rise of hardware capabilities and the algorithms efficiency, extended the applicability of computational chemistry to high-level methods and larger systems, unlocking rich and diverse information about the energetics, structures and properties of systems ranging from small organic molecules to proteins and nanoparticles. The joint evolution of computer science and theoretical chemistry resulted in numerous tools and methods that helped understanding, designing and predicting the chemical phenomena - invaluable achievements, which were recognized with two Nobel prizes in chemistry over the past 20 years (1998 and 2013).

Today, there is little doubt that quantum computations are both authoritative and widely applicable. However, following Parr's dictum, "to compute is not to understand".¹ Computational chemistry relies upon such quantities as the electron density and the wavefunction, which are challenging to rationalize in terms of insightful chemical concepts.²⁻⁴ Consequently, interpretative rather than simply quantitative methods are required to gain fundamental comprehension and recover chemical intuition.

Description of the different types of covalent and non-covalent interactions colorfully illustrates this *conundrum*. Their traditional classification based on bond order, covalency, *etc.* rely on non-unique definitions and are often imprecise. In quantum chemistry, visualizing, categorizing, and, ultimately, understanding chemical interactions remains a long-standing quest. On one hand, some of the classical concepts entail no proper definitions, and cannot be

unambiguously recovered from rigorous theoretical foundations. On the other hand, the difficulties in interpreting the wavefunction and the electron density complicate their translation into sound chemical concepts.

The emergence of molecular scalar fields, such as the Electron Localization Function (ELF),^{5,6} became a breakthrough in this *status quo*. These mathematical functions ably represent the chemical interactions as intuitive 3D-models, typically similar to the classical VSEPR or Lewis picture of bonding. As molecular scalar fields exploit the wavefunction and/or electron density (matrices), they allow (re)defining the physically rigorous concepts linked with traditional definitions, or even designing new rationales.⁷

Two recurrent pathologies of the available molecular scalar fields are (i) their inadequacy in simultaneously capturing the whole range of existing chemical interactions, and (ii) their limited compatibility with certain electronic structure methods. De Silva and Corminboeuf addressed both problems with the Density Overlap Region Indicator (DORI),⁸ an intuitive molecular scalar field, which captures covalent and non-covalent interactions simultaneously, exploiting the routinely available electron densities. DORI's performance has already been validated for static model monomers and dimers in the gas phase at 0 K - the standard playground for many other scalar fields. However, chemistry stretches far beyond simplified, rigid, isolated, unperturbed molecules, its many facets encompass intriguing phenomena involving dynamic and flexible systems in complex environments. The aim of this thesis is to drive DORI out of its comfort zone and model systems in photoexcited states, follow the dynamical behavior of highly fluxional molecules, and monitor chemical interactions under geometrical constraints imposed by either protein environment or organic crystal packing under high pressure.

As DORI is mostly used as an intuitive visual tool, **Chapter 2** presents other key molecular scalar fields already exploited as visual bonding descriptors. The Electron Localization Function (ELF),⁵ which is probably the most popular bonding descriptor, is introduced first *via* its original definitions for Hartree-Fock (HF) and DFT methodologies. These ELF definitions are generally inappropriate when applied outside of the HF or DFT framework, thus several ELF flavors, as well as ELF-like functions, are then presented. Finally, ELF and its relatives are not designed to capture non-covalent interactions. Thus, alternative bonding descriptors, such as the Non-Covalent Interaction index,^{9,10} were recently exploited and are presented in the last part of the chapter. Each function is introduced with a particular emphasis on its strengths and limitations based on its applicability to computational or experimental methods, its intuitiveness, and the range of molecular interactions it captures.

The visual descriptors presented in **Chapter 2** lack versatility to monitor covalent and non-covalent interactions simultaneously, and generally rely on the wavefunction, which is impractical when, for example, (i) a sufficiently accurate wavefunction is not available, (ii) orbital free computational approaches are concerned, or (iii) the information about the system comes from experimental electron densities. **Chapter 3** describes the advent of the Density Over-

lap Region Indicator (DORI), a function that is based solely on the electron density and its derivatives, and that captures covalent and non-covalent interactions on an equal footing. We start with DORI genesis from the closely related Single Exponential Decay Detector (SEDD) devised by De Silva *et al.*¹¹ before presenting its key features - covalent bonds of various nature, π -delocalized bonds, and inter-molecular interactions- for illustrative molecules.

Chapter 4 presents our first endeavor outside the traditional applications of scalar fields in general, and DORI in particular - the domain of photoexcited states. Typical methodologies for excited state modelling, such as the Time-Dependent-DFT, provide the excited state electron density, but lack information about the excited state wavefunction. On the other hand, many popular visual bonding descriptor (*e.g.*, ELF) formally depend on the wavefunction, thus the visual characterization of covalent and non-covalent interactions in excited state has never been performed properly. DORI, which relies on the electron density and its derivatives only, is however perfectly suited to analyze excited states. In **Chapter 4**, we pinpoint DORI's ability to expose excited-state signatures (*e.g.*, Rydberg, $\pi - \pi^*$, excimer and charge transfer) for selected archetypal molecules and complexes, encompassing also organic and metal-organic examples. This work is published in Chemistry- A European Journal.¹²

Dynamic fluctuations are another domain often underexploited by scalar fields. In particular, the analysis of highly fluxional systems such as molecular switches and rotors, generally requires investigating the chemical interactions occurring across a molecular dynamic trajectory to properly rationalize the properties of the systems of interest. These interactions are typically probed using collective variables derived from geometrical parameters or from dimensionality reduction algorithms based on machine learning. In **Chapter 5**, we use DORI to monitor the interactions in highly fluxional molecules, and compare the obtained density-based analysis with standard and state-of-the-art structural information. We analyze the fluxional behavior of a dithiocyclophane molecule, which is dominated by several conformations featuring varying π -overlaps. We also pinpoint the DORI fingerprints associated with CH- π and π - π interactions in a molecular rotor, and examine the fluctuating π -conjugation pathway of a photochromic torsional switch.

Finally, applying high pressure on crystals triggers phase transition, polymorphism, dramatic changes in electronic structures or even chemical reactions, and thus present an interesting, but challenging case for the DORI descriptor. Pressure-induced modifications have been recently monitored using experimental X-ray diffraction, which allows retrieving high resolution electron densities. In **Chapter 6** we exploit DORI to investigate the evolution of intra and intermolecular interactions in an organic crystal under high pressure. In contrast to the ambient pressure conditions, a strong interplay between covalent and non-covalent interactions is observed at high pressure. Notably, the crystal anisotropy translates to intramolecular region and causes the observed symmetry breaking of molecules inside the crystal, and a peculiar $\overset{\text{C}}{\text{H}} - \text{O}$ interaction, pointing directly towards the C-H bond, enforces the disruption of intramolecular electron delocalization. This chapter pioneers DORI's application to experimental electron densities, and presents the first visual interaction analysis of high-pressure organic crystals.

To conclude, **Chapter 7** summarizes the non-trivial applications of DORI in areas typically overlooked by other visual bonding descriptors. Future directions are presented, including using DORI to discover electron density-based chemical patterns in molecular databases of *e.g.*, metal-organic frameworks, and to improve libraries of electron density fragments for building molecular electron densities. Besides, possible applications exploiting a recently developed quantum mechanics/molecular mechanics partitioning based on DORI are outlined.

2 Characterization of Chemical Interactions Using Molecular Scalar Fields

Computing quantum physical data is now routinely possible, but deriving a formal classification of chemical bonds and interactions based on computations remains intricate due to (i) the lack of intuitive information, and (ii) the fuzzy (or even ill-defined) nature of classical chemical concepts such as chemical bonding.

One way to recover chemical intuition is to visualize chemical interactions. The electron density ($\rho(\mathbf{r})$) seems particularly well suited for this task, as (i) it is directly representable in real space, (ii) is widely available from theoretical and experimental frameworks, and (iii) is formally able to describe many-body effects like chemical bonding through the Hohenberg and Kohn theorem.¹³ In practice, $\rho(\mathbf{r})$ is rather featureless, which prevents its use for intuitive representations. In particular, $\rho(\mathbf{r})$ generally lacks sensitivity to properly describe non-covalent interactions such as van der Waals,⁴ except in peculiar systems with high polarizability density or low dimensionalities.¹⁴

Another popular visual descriptor is the molecular electrostatic potentials, $V(\mathbf{r})$,¹⁵ represented as a map of variably charged regions on a given $\rho(\mathbf{r})$ isosurface. Applications of $V(\mathbf{r})$ generally target interactions with a significant electrostatic contribution such as hydrogen or halogen bonds,^{16–19} or in the study of substituent effects on $\pi - \pi$ interactions.^{20,21} Unfortunately, $V(\mathbf{r})$ is not designed for capturing interactions with weak electrostatic contributions, possibly leading to misinterpretations.²²

One-electron orbitals are commonly available in single-determinantal computational methods like Hartree-Fock (HF) or Density Functional Theory (DFT), and are straightforward to visualize in real space. Many chemically intuitive interpretations can be devised based on their shape and position, effectively rationalizing covalent bonding, reactivity, ... Their drawbacks are their lack of proper definition in quantum mechanics, their delocalized nature, and their representation of a single pair of electrons per orbital, leading to non-trivial interpretations when electrons from different orbitals significantly contribute to a given interaction (*e.g.*, in cation- π or van der Waals interactions).

An alternative to the aforementioned descriptors is the family of molecular scalar fields, which

Chapter 2. Characterization of Chemical Interactions Using Molecular Scalar Fields

are mathematical functions specifically designed to reveal chemical interactions based on quantum computations. These functions are typically analyzed following two philosophies: the first exploit the rigorous mathematical frameworks of topology,²³ while the second favors flexible interpretations of intuitive real-space representations.

The topological approach provides for a handy real space partitioning: molecules are divided into basins, usually corresponding to individual atoms and/or bonding domains. The contributions of the obtained fragments to a given property might be computed, allowing to redefine classical concepts (bonds, atoms, charges, ...) within the rigorous mathematical framework of topology. This methodology, pioneered by Bader in its analysis of the electron density,²⁴ (see Appendix A) has been successfully applied to the Laplacian of the electron density, the electrostatic potential, the intracule density, the Ehrenfest force field or the Electron Localization Function (ELF). However, the mathematical rigor stemming from the topological analysis of the scalar field generally comes at the expense of intuitiveness: the definitions of our invaluable classical chemical concepts typically change, or disappear. Instead, a new definition is generated, which now depends on the real space partitioning, that is, on the chosen molecular scalar field, possibly leading to confusions.^{25–28}

The second class of molecular scalar fields favors heuristic representations of chemical interactions, with a typical relation the intuitive Lewis and VSEPR bonding theories. These scalar fields generally offer a versatile bridge between quantum computations and traditional chemical concepts. However, this flexibility might cause difficulties when relating with fuzzy, and possibly ill-defined concepts (*e.g.*, aromaticity, atomic charges, ...). With intuitive scalar fields, the risk of over-interpretation becomes tangible, possibly leading to a method becoming as imprecise as the concepts it might recover.

Note that this classification is based on how a scalar field is used and developed. The topological analysis remains formally possible on any scalar field, while the choice between heuristic or mathematical arguments is possible for scalar fields combining both approaches (*e.g.*, ELF).^{5,29}

Regardless of the chosen philosophy, several features remain desirable in any molecular scalar field. The functions should be broadly applicable to both theoretical and experimental frameworks, and thus rely on easily available quantum data. Furthermore, they should cover as much content as possible, *i.e.*, capture most or all of the bonding and non-bonding interactions, while keeping some distinctive patterns allowing to characterize interactions. Finally, the computational cost of the scalar field should also be considered, in order to apply it to (possibly large) systems of interest.

This chapter gives an overview of the main molecular scalar fields used as visual descriptor for chemical interactions, pinpointing their relative strengths and weaknesses. Emphasis is given towards intuitive scalar fields, as this approach is followed for the applications of the Density Overlap Region Indicator presented in this thesis.

2.1 Localization Functions

Since the seminal work of Lewis on the chemical bond, chemists have extensively exploited the concept of electron pairs to rationalize chemical bonding. This thinking has also repercussions in the development of molecular scalar fields, where several descriptors focused on finding regions of space where electrons form pairs.

2.1.1 Lodges Theory

The search of regions where electrons are located can be traced back to the pioneering work of Daudel on the lodges theory.^{30,31} This theory introduces the idea of using theoretical methods to partition the real space around molecules into regions connected with the Lewis picture. Lodges are defined by looking at the probability $P_n(\Omega)$ to find n -electrons inside a spatial domain Ω , called lodge, while all other $(N-n)$ electrons are located elsewhere :

$$I(\Omega) = - \sum_n P_n(\Omega) \ln(P_n(\Omega)) \quad (2.1)$$

The lodge location and size are defined by the user, allowing to position lodges centers at atomic positions and bond midpoints, leading to intuitive space partitioning into core and bonding regions.

This idea was further exploited by Bader and Stephens,^{32,33} who investigated the fluctuation of the electron population in a region Ω :

$$\Lambda(\Omega) = \sum_n n^2 P_n(\Omega) - \left[\sum_n n P_n(\Omega) \right]^2 \quad (2.2)$$

Both lodge definitions allow for real space partitioning between bonding and atomic regions, with a particular emphasis on electron pair localization in Bader and Stephens' works. However, these methods suffer from their expensive computational scaling and algorithmic difficulties when applied to larger systems.

More recently, Savin *and co.* reused the lodge idea to define maximum probability domains.³⁴ The resulting domains can be connected with chemical descriptors like bonds, lone pairs and cores,³⁵⁻³⁸ but the determination of these domains remains a demanding task for real-life applications.³⁹ Furthermore, the lodges show a high sensitivity to the theoretical model employed, with marked difference when passing from single determinantal methods (like DFT or HF), to correlated wave functions.^{37,40}

2.1.2 Electron Localization Function (ELF)

Instead of computing the expensive lodges, Becke and Edgecombe proposed a measure able to retrieve regions where electrons pairs are located, the Electron Localization Function (ELF),⁵

Chapter 2. Characterization of Chemical Interactions Using Molecular Scalar Fields

which is nowadays one of the most popular bonding descriptor. ELF evaluates the electron localization by analyzing the local behavior of the HF parallel-spin pair probability. This probability is approximated using the leading term of the Taylor expansion of the spherically averaged conditional pair probability:^{41,42}

$$P_{cond}(\mathbf{r}, s) \approx \frac{1}{3} \left[\tau - \frac{1}{4} \frac{(\nabla \rho(\mathbf{r}))^2}{\rho(\mathbf{r})} \right] s^2 \quad (2.3)$$

where $\tau = \sum_i |\nabla \psi_i|^2$ is the kinetic energy density in the HF formalism. The smaller the probability of finding another electron of same spin, the higher the localization of the reference electron. The conditional pair probability gives a physical ground to ELF, as it is related to the Fermi hole curvature where effects of the Pauli repulsion are directly reflected.^{33,43–45} While $P_{cond}(\mathbf{r}, s)$ retrieves localization in space, it is inconvenient to visualize.⁵ A calibration was added to include "somewhat more desirable features"⁵ using a reference to the uniform electron gas (UEG) and a Lorentzian mapping of the function in the [0,1] interval:

$$ELF = \left(1 + \left(\frac{D}{D^0} \right)^2 \right)^{-1} \quad (2.4)$$

where $D^0 = \frac{3}{5}(6\pi^2)^{\frac{2}{3}}\rho^{\frac{5}{3}}$, is the corresponding probability in a UEG with density equal to $\rho(\mathbf{r})$ and $D = \tau - \frac{1}{4} \frac{(\nabla \rho)^2}{\rho}$. Thanks to this calibration, the resulting ELF function becomes dimensionless and system independent, *i.e.*, having the same range of values for all systems. Furthermore, low and high ELF values now correspond to domains of low and high electron localization, respectively. Finally, ELF remains independent from unitary transformation of canonical molecular orbitals, which allowed for ELF interpretations using orbital-based arguments.^{46–48}

ELF reformulation The ELF formulation of Becke and Edgecombe is based on electron pair interactions, which are intricate to retrieve in the popular DFT formalism.^{49,50} To circumvent this limitation, Savin proposed an alternative ELF definition^{51,52} using kinetic energy densities $\tau = \frac{1}{2} \sum_i |\nabla \psi_i|^2$ computed with Kohn-Sham orbitals. This allows to rewrite the ELF numerator according to:

$$D = \frac{1}{2} \sum_i |\nabla \psi_i|^2 - \frac{1}{8} \frac{|\nabla \rho(\mathbf{r})|^2}{\rho(\mathbf{r})} \quad (2.5)$$

which can be formally interpreted as the Pauli kinetic energy density τ_P .⁵² Both ELF definitions of Silvi and Savin,^{51,52} and Becke and Edgecombe,⁵ provide for identical real space functions for closed shell systems, and will hence not be distinguished in the applications discussed herein.

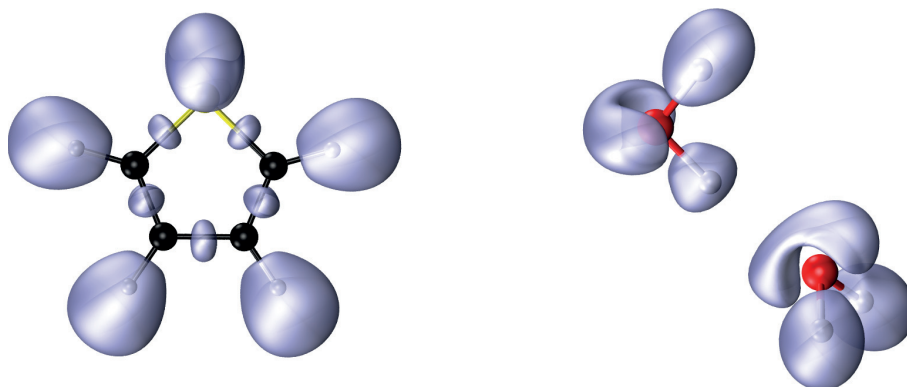


Figure 2.1 – Isosurface of $ELF = 0.85$ for thiophene (left) and water dimer (right).

2.1.3 ELF Applications

Part of the ELF success comes from its intuitive 3D-representation of domains where electrons are localized.^{29,53} (see Figure 2.1). ELF basins cover the traditional position for chemical bonds, and allow for a formal classification of bonds based on quantum mechanical function.⁶ Lone pairs are also revealed by ELF as individual basins, completing the traditional Lewis or VSEPR models. Besides, core electrons are separated according to the shell they belong.⁵

In general, the visual interpretation of ELF domains must be handled with care as the resulting picture depends on the f -localization isovalue chosen. Indeed, as the ELF value is lowered, basins start to merge together, encompassing several ELF attractors, and the global picture of a given molecule might change.^{54,55} A common practice is either to analyze the basin behavior at different isovalues, generating a bifurcation diagram,⁵⁴ or to choose an isovalue known as a useful standard (*e.g.*, $ELF=0.8$ for covalent bonds in organic molecules).⁵³ With this in mind, the analysis of the shape of these basins allows for the characterization of a wide range of bonding situations. In particular, ELF distinguishes bond multiplicities, multicenter bonds, delocalization effects and resonances structures. Visual examples are nicely summarized in the recent ELF perspective of Grin *et al.*²⁹

ELF quantitative analysis is based on topological tools similar to the Quantum Theory of Atoms and Molecules²⁴ (*i.e.*, based on the Hessian of ELF, see Appendix A for more details). Such analysis have been used to rationalize bond multiplicity,⁵⁶ polarity,⁵⁷ delocalization,^{58–60} three-electrons bonds,^{61,62} charge-shift bonds,⁶³ transition metals and metal-metal interactions,^{53,64,65} or the participation of mesomers to a given electronic structure.^{66,67} They also tackled the delicate task of indicating if an interaction is "chemical" or not (*e.g.*, in the context of H-bond)^{68–71} effectively categorizing a broad range of interactions, including many electron-shared and some electron-unshared interactions.^{72,73}

2.1.4 ELF Limitations and Remedies

While ELF is a well-established and versatile tool, it is not free from some inconveniences. The first one concerns the more or less arbitrary scaling based on the UEG,^{45,53,74} which was at the aim of certain criticisms (*e.g.*, from Bader and Popelier⁷⁵) and interpretative misconceptions.^{47,76} Furthermore, the UEG reference is sometimes a tedious reference, like in excited state or when using multi-reference methods, where no UEG counterpart exists.

The second limiting step is the computation of the parallel-spin electron pair probability using the kinetic energy density τ , which is typically computed using orbitals. This feature is troublesome in all situations where the wavefunction is not directly available, including (i) densities obtained from experiments (X-ray diffraction), (ii) excited states computed by traditional (unconstrained) Time-Dependent DFT,^{77,78} and (iii) orbital-free approaches.^{79,80}

Orbitals from $\rho(\mathbf{r})$ Since τ is generally computed using orbitals, but electron densities are more widely available than orbitals, one solution is to reconstruct orbitals from $\rho(\mathbf{r})$. One emergent method is the X-ray constrained wavefunction of Jayatilaka *et al.*^{81–83} This technique is based on the structure factor obtainable either directly from experiment,^{84–86} or from computed densities.⁸⁷ However, this method remains computationally expensive, and requires a high expertise from its user. Alternatively, it is always possible to generate a Kohn-Sham potential corresponding to a given density,⁸⁸ which allows to generate orbitals by solving the Kohn-Sham equations using this potential.⁸⁹

Density-based ELF Limitations due to orbital dependence might also be addressed by re-defining the ELF function. Gadre *et al.*⁹⁰ proposed to approximate the conditional pair probability density using the nonlocal density approximation.⁹¹ Within this framework, they were able to derive an approximate ELF as a function of the density only. The resulting DELF shows similar topologies to ELF, although differing quantitatively. In particular, DELF should not be interpreted from its contour values, due to its inherent overestimation of delocalization.⁹⁰

Other approaches maintain ELF definition, and computes τ using orbital-free approximations. Fuentealba *et al.* proposed to describe τ using the electron density, the electrostatic potential, and the exchange energy density.⁹² The obtained ELF derivative, called ESP-ELF, keeps most of ELF features, except near nuclei where ESP-ELF \approx 0 and ELF \approx 1. Likewise, Tsirelson and Stash computed τ using the second-order gradient expansion of the kinetic energy density.⁹³ However this approach proved to diverge near nuclei, where the Laplacian of the electron density diverges. Finally, Ayers examined several possible approximations to compute τ without orbitals,⁹⁴ including the Thomas-Fermi, Weizsäcker, and the gradient expansion models. Ayers noted that, conversely to the gradient expansion, the Weizsäcker expression is accurate in the vicinity of nuclei, where the 1s orbital mostly contributes to the kinetic energy. In other regions, the gradient expansion model provides for more reliable values. Hence, Ayers proposed a range-separated model where the short-range is handled by the Weizsäcker model,

while the rest is computed using the gradient expansion, using a switching function based on the atomic number.⁹⁴

Despite the invested efforts to find good approximations for τ without referring to orbitals, the resulting ELF-like functions inevitably differ from the original ELF. In particular, the physical interpretation of density-based ELF in term of electron pair probabilities is no more possible.^{92,93} Furthermore, while all the obtained functions showed topological features similar to ELF, they still significantly differ in their absolute values, notably obscuring the shell structure.⁹⁴

2.1.5 ELF and Correlated Wavefunctions

Since ELF is ill-defined at the correlated level of theory, due to complications related to both the UEG and to the kinetic energy density definitions,^{76,95–98} alternative functions were developed.

Electron Localizability Indicator (ELI) Kohout *et al.* proposed the Electron Localizability Indicator (ELI),⁷⁴ based on the electron pair density. The pair density is computed using the ω -restricted partitioning of the real space, with the condition that each domain encloses the same amount of electron pair(s).^{74,99} This definition completely avoid the reference to the UEG and the computation of the kinetic energy density, and is suitable for correlated wave functions. Furthermore, different partitionings are available depending on the electron pair chosen (*e.g.*, same-spin, opposite-spin, ...), leading to several complementary scalar fields.^{76,100–103} At the uncorrelated level, ELI keeps the same topology as the ELF function, and its visualization through space is intuitive. However, while ELI is more generally applicable than ELF, it still relies on electron pair information, which is not directly obtainable from the electron density alone. Furthermore, ELI and its variants are not bounded from above, which complicates comparison between different systems.

Electron Pair Localization Function (EPLF) The Electron Pair Localization Function¹⁰⁴ is another suitable descriptor for correlated wavefunctions. Given an electron position \mathbf{r} , it computes the average distance with the closest same-spin ($d_{\sigma\sigma}(\mathbf{r})$) and opposite spin electron ($d_{\sigma\bar{\sigma}}(\mathbf{r})$):

$$EPLF = \frac{d_{\sigma\sigma}(\mathbf{r}) - d_{\sigma\bar{\sigma}}(\mathbf{r})}{d_{\sigma\sigma}(\mathbf{r}) + d_{\sigma\bar{\sigma}}(\mathbf{r})} \quad (2.6)$$

EPLF provides for insights into the nature of the pairing and localization of electrons, and to understand the role of the dynamical and nondynamical near-degeneracy correlation effects.^{37,97,105} EPLF is directly applicable to the highly accurate quantum Monte Carlo methods, further extending the range of possible applications for visual bonding descriptors. At the

uncorrelated level of theory (*e.g.*, DFT or HF), EPLF shares high similarities with ELF for closed shell systems,⁹⁷ confirming its ability to retrieve regions where electrons localize.

2.1.6 Domain-Averaged Fermi Holes (DAFH)

Functions based on one- and two-particle density matrices might be ideally used at the correlated level of theory. The domain-averaged Fermi hole (DAFH)¹⁰⁶ analysis belong to this category, relying on the correlation function $C(\mathbf{r}_1, \mathbf{r}_2)$, defined using pair $(\rho(\mathbf{r}_1, \mathbf{r}_2))$ and one-electron densities $(\rho(\mathbf{r}_1))$:

$$C(\mathbf{r}_1, \mathbf{r}_2) = 2\rho(\mathbf{r}_1, \mathbf{r}_2) - \rho(\mathbf{r}_1)\rho(\mathbf{r}_2) \quad (2.7)$$

which can be integrated over a finite domain Ω_B to yield the DAFH:

$$g_B(\mathbf{r}_1) = - \int_{\Omega_B} C(\mathbf{r}_1, \mathbf{r}_2) d\mathbf{r}_2 \quad (2.8)$$

where the finite domain might be completely arbitrary, but generally exploit the Atoms In Molecules partitioning.¹⁰⁷

DAFH give insights on the mutual coupling of electrons, which is exploited to describe bond formation and dissociation of organic and organometallic compounds, and can shed more light on the effect of dynamical electron correlation in the bond description.^{107–109}

2.1.7 Kinetic Energy Density

The Localized Orbital Locator (LOL)¹¹⁰ is a variation of ELF without reference to the von-Weizacker term:

$$LOL = \frac{1}{1 + \frac{\tau}{D_0}} \quad (2.9)$$

The resulting function thus only compare the kinetic energy of an electron in the evaluated system with the local kinetic energy of a UEG. LOL clearly depicts the location of classic VSEPR electric group, showing topological features similar to ELF. The simpler function LOL may be easily interpreted in terms of fast and slow electrons (*i.e.*, localized electrons, having low LOL values, and delocalized electrons with high LOL values). More importantly, this work emphasizes the chemical content of the kinetic energy density, instead of the conditional pair probability of ELF.

Kinetic energy densities were further exploited by Finzel *et al.* in their research for density based ansatz to kinetic energy density functionals.¹¹¹ It was shown that several expressions behind localization functions could be understood as modifying functions to describe $\tau(\mathbf{r})$ using references to the kinetic energy density of two model systems: the ground state bosonic system and the homogeneous electron gas. All the functions derived in this way were able to

retrieve atomic shells, a descriptor often exploited to assess the possibilities of a given scalar field.

2.2 Capturing Non-covalent Interactions

Regions where electron localize are not the only interesting domains in chemical systems. For example, most of the non-covalent interactions take place in regions where electrons are not localized. Localization functions, by their construction, are not designed to retrieve such information, and new molecular scalar fields philosophies are required to properly capture the wide range of possible non-covalent interactions.^{112,113} It is noteworthy to mention at this point that QTAIM can in principle handle non-covalent interactions, but define them using QTAIM bond paths which are identical for both covalent and non-covalent patterns. This is unpractical when considering non-directional interactions such as van der Waals, which are not intuitively represented using QTAIM bond paths.⁴

The local-wave vector

The common rationale for most of the actual density-based functions able to capture non-covalent interactions is the local-wave vector $-\mathbf{k}(\mathbf{r}) = \frac{\nabla\rho(\mathbf{r})}{\rho(\mathbf{r})}$. One strength of $\mathbf{k}(\mathbf{r})$ is that the information of $\rho(\mathbf{r})$ and $\nabla(\rho(\mathbf{r}))$ are added up,¹¹⁴ and reveal atomic shell structure.^{114,115} From the information theory point of view, a physical interpretation of $\mathbf{k}(\mathbf{r})$ has been given in terms of Shannon's or Fisher's information per particle.¹¹⁵⁻¹¹⁷ $\mathbf{k}(\mathbf{r})$ is also related to the kinetic energy density in the absence of the Pauli principle $\left(\tau_{\omega}(\mathbf{r}) = \frac{\rho(\mathbf{r})|\mathbf{k}(\mathbf{r})|^2}{8}\right)$.

Localized Electron Detector (LED)

Conscious that QTAIM is both computationally demanding and sometimes cryptic to visualize, Bohorquez and Boyd proposed the Localized Electron Detector (LED) as a complementary tool to QTAIM:¹¹⁸

$$\mathbf{P} = -\frac{\hbar}{2} \frac{\nabla\rho(\mathbf{r})}{\rho(\mathbf{r})} \quad (2.10)$$

\mathbf{P} is a vector field, pointing in the direction of maximum decrease of electron density. Its values, obtained through the modulus of the vector field ($|\mathbf{P}|$), are related to the local charge depletion. LED values are bounded between 0 at critical points of $\rho(\mathbf{r})$ and Z_A near the nucleus, where Z_A is the atomic number of the considered nucleus. This behavior is exploited in practice to visualize separately bonding and atomic regions, as they appear at different LED values.

LED is applicable to any level of theory, thanks to its formulation depending on the electron density and derivatives only. Furthermore, LED detects both covalent and non-covalent regions, making it a highly versatile tool. However, the 3D-representations of non-covalent

interactions tend to lack clarity, as the covalent region dominates the plot.¹¹⁸

Non-covalent interaction index (NCI)

NCI is a recently developed tool which emphasizes the possible use of the reduced density gradient $s(\mathbf{r})$ to monitor non-covalent interactions:^{9,10}

$$s(\mathbf{r}) = c \frac{|\nabla \rho(\mathbf{r})|}{\rho(\mathbf{r})^{\frac{4}{3}}} \quad (2.11)$$

where $c = 2(3\pi^2)^{\frac{1}{3}}$ is the Fermi constant, and the 4/3 exponent on the electron density ensure the dimensionless character of $s(\mathbf{r})$. While NCI developed the visual analysis based on $s(\mathbf{r})$, the properties of $s(\mathbf{r})$, and in particular its ability to capture the deviation from a homogeneous electron distribution, were already scrutinized in the process of developing accurate DFT functionals.^{119–122}

The analysis of 2D plots consisting in $s(\mathbf{r})$ versus $\rho(\mathbf{r})$, can set an emphasis on regions of low density to reveal non-covalent interactions.^{9,10} By selecting values of $s(\mathbf{r})$ in regions of low electron density, NCI is able to visualize only non-covalent interactions in real space (see Figure 2.2).^{9,10} NCI also incorporates the QTAIM λ_2 analysis (see Appendix A) in its toolbox. The sign of λ_2 is known to qualitatively indicate whether an interaction is attractive ($\lambda_2 < 0$) or repulsive ($\lambda_2 > 0$) at the QTAIM critical point. When the sign of λ_2 is multiplied by the value of $\rho(\mathbf{r})$, it provides for qualitative interaction strengths. Non-covalent interactions revealed by $s(\mathbf{r})$ may be color-coded by the electron density multiplied by the sign of λ_2 : $\text{sgn}(\lambda_2)\rho(\mathbf{r})$. This allows for a quick visualization of attractive (red) and repulsive (blue) non-covalent interactions, even in large systems.¹²³

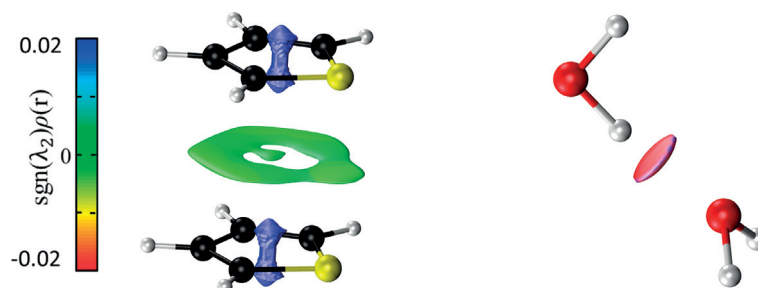


Figure 2.2 – NCI=0.6 isovalue for a thiophene dimer (left) and a water dimer (right), color coded with the $\text{sgn}(\lambda_2)\rho(\mathbf{r})$.

In principle, $s(\mathbf{r})$ is also able to describe covalent interactions,¹²⁴ although this aspect was not covered in the original publications.^{9,10} The motivation came from the observed deviations from the exponential behavior when $s(\mathbf{r})$ is plotted versus $\rho(\mathbf{r})$ for interacting systems. A rationalization of the ability of $s(\mathbf{r})$ to describe bonding regions was given in terms of the kinetic energy density in the absence of the Pauli principle.¹²⁴ However, the practical applications in the covalent domain remains sparse, and still require applying an arbitrary threshold on $\rho(\mathbf{r})$

values. Furthermore, for large systems (*i.e.*, larger than diatomic), bonding information are not retrievable from 2D-representations of NCI.

2.3 Conclusion

Many interpretative tools are now available and generate intuitive representations from quantum computations. These tools cover both intermolecular and intramolecular interactions allowing for a complete overview of molecular interactions by coupling different scalar fields. This strategy was recently adopted to follow chemical reactions by coupling ELF and NCI, effectively considering covalent bonding and non-covalent interactions.^{125,126}

Coupling interpretative techniques is, however, not free from some risks. Both scalar fields have values in the whole space, and possibly give conflicting information about an interaction. This might be avoided by user-defined partitioning, where different regions of space are attributed to different scalar fields, but at the risk of inducing bias in the chemical interpretation.

Hence, a widely applicable scalar field able to grasp simultaneously intra- and intermolecular interactions in intuitive representations remains desirable.

3 DORI

3.1 Single Exponential Decay Detector (SEDD)

Density-based molecular scalar fields benefit from being well defined at any level of theory and can spontaneously describe densities coming from experiments, which is not the case of their wavefunction-based counterparts (*e.g.*, ELF). However, density-dependent bonding descriptors are not so many, and the existing ones (*e.g.*, the Quantum Theory of Atoms in Molecules)²⁴ are typically less intuitive than the popular ELF.⁵

The Single Exponential Decay Detector (SEDD),¹¹ derived by De Silva and Wesolowski, is a notable exception to the cryptic nature of density-based descriptors. In its philosophy, SEDD induces a paradigm shift with respect to localization descriptor: it searches for mathematical, rather than physical, properties of electron densities. The track for mathematical features of the electron density starts from the observation that regions of increased electron localization are well-described using a single orbital, which implies that $\rho(\mathbf{r}) \sim e^{-\lambda|r-r_0|}$. In such regions, the wave vector $k(\mathbf{r}) = \frac{-|\nabla\rho(\mathbf{r})|}{\rho(\mathbf{r})}$ is constant,¹¹⁴ or expressed differently: $\nabla\left(\frac{\nabla\rho(\mathbf{r})}{\rho(\mathbf{r})}\right)^2 = 0$.

To generate a universal detector, the expression $\nabla\left(\frac{\nabla\rho(\mathbf{r})}{\rho(\mathbf{r})}\right)^2$ was further calibrated^{11,127} to become dimensionless as well as more convenient to visualize, leading to the final SEDD equation:

$$SEDD(\mathbf{r}) = \ln \left[1 + \left(\frac{\nabla\left(\frac{\nabla\rho(\mathbf{r})}{\rho(\mathbf{r})}\right)^2}{\rho(\mathbf{r})} \right)^2 \right] \quad (3.1)$$

SEDD takes low values in regions attributed with electron shells, bonds and lone pairs, and goes to infinity otherwise (*e.g.*, far from molecules). A physical interpretation for SEDD was given in terms of the local wave vector $k(\mathbf{r})$ and the homogeneous electron gas taken as a reference system.¹²⁷

One key advantage of SEDD is its ability to recover essentially the same information as ELF using only the electron density and its derivatives: atomic shells, lone electron pairs and

covalent bonds are all characterized by SEDD signatures.^{11,128} The population of SEDD-defined atomic shell stays in close agreement with the Aufbau principle,¹²⁷ a criterion generally proposed as indicative of the quality of a given scalar field.^{5,129}

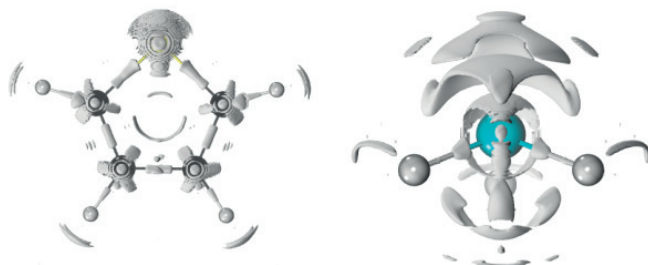


Figure 3.1 – Three-dimensional representation of SEDD=3 isovalue for thiophene (left) and NH₃ (right).

Although most SEDD applications focused on covalent regions, a decrease of SEDD values is observed in the non-covalent region between molecules.¹¹ Hence, SEDD captures simultaneously covalent and non-covalent interactions. In practice, however, the regions of low density suffer from strong basis set dependence, rapidly inducing numerical noise in the SEDD evaluation. Another inconvenience concerns the $[0, +\infty]$ range, with covalent and non-covalent regions appearing at different SEDD values. Thus, the insightful SEDD isovalues must be evaluated in a case by case fashion for different systems and/or interactions.

3.2 Density Overlap Region Indicator (DORI)

Owing to the SEDD difficulties for visualizing simultaneously covalent and non-covalent interactions, the function was modified by De Silva and Corminboeuf in 2014.¹³⁰ The construction of DORI starts from the observation that, for exponential densities, the SEDD kernel $\left(\frac{\nabla \mathbf{k}^2(\mathbf{r})}{\rho(\mathbf{r})}\right)^2$ is proportional to $\left(\frac{\nabla \rho(\mathbf{r})}{(k_F^3)^2}\right)^2$,¹²⁷ where $\nabla \mathbf{k}(\mathbf{r}) = \frac{\nabla \rho(\mathbf{r})}{\rho(\mathbf{r})}$ is the local wave vector^{114–116} and $k_F = (3\pi^2\rho)^{1/3}$ is the Fermi wave vector of the UEG model. The UEG reference is often exploited to generate dimensionless indicators, but is problematic in certain cases (see section 2.1.4). Another choice is the function self-reference at the proper power:

$$\theta(\mathbf{r}) = \frac{(\nabla \mathbf{k}^2(\mathbf{r}))^2}{(\mathbf{k}^2(\mathbf{r}))^3} = \frac{\left(\nabla \left(\frac{\nabla \rho(\mathbf{r})}{\rho(\mathbf{r})}\right)^2\right)^2}{\left(\frac{\nabla \rho(\mathbf{r})}{\rho(\mathbf{r})}\right)^6} \quad (3.2)$$

$\theta(\mathbf{r})$ is exactly zero for single exponential densities, like close to the nuclei ($\rho(\mathbf{r}) \sim e^{-2Z_a|\mathbf{r}-\mathbf{r}_a|}$),¹³¹ and far from the molecule ($\rho(\mathbf{r}) \sim e^{-2(2I)^{1/2}|\mathbf{r}|}$).¹³² In bonding regions, the gradient of the density is typically small ($\nabla \rho(\mathbf{r}) = 0$ at the bond critical point) which makes the numerator and denominator of $\theta(\mathbf{r})$ to tend towards zero. As the denominator decays faster than the numera-

tor, $\theta(\mathbf{r}) \rightarrow +\infty$ at the bond critical point. Thus, $\theta(\mathbf{r})$ behaves differently in bonding regions and in regions with single exponential densities (near nuclei and far from molecules), which designate θ as a possible bonding descriptor. Since unbound values are typically disadvantageous for visualization purposes, $\theta(\mathbf{r})$ was rescaled in the $[0,1]$ interval using a Lorentzian mapping:

$$DORI = \frac{\theta(\mathbf{r})}{1 + \theta(\mathbf{r})} \quad (3.3)$$

which is final DORI expression. Like SEDD, DORI is not a localization function, but tracks instead the geometrical features of the electron density by revealing the disruption of the (piecewise) exponential behavior of $\rho(\mathbf{r})$ due to interactions between electrons. The independence from localization is easily shown by looking at the contrasting DORI values near the nuclei ($DORI \rightarrow 0$) and the bonding regions ($DORI \rightarrow 1$), both having substantially localized electrons. In this aspect, it follows the SEDD philosophy to probe regions where the density deviates from a single exponential behavior due to the overlap of electron densities coming from distinct atoms or molecules. In the process, DORI naturally recovers regions typically associated with covalent bonds, non-covalent interactions, and density overlaps between different atomic shells (see Figure 3.3).

3.2.1 DORI[f] Domains

The representation of any scalar fields in real space requires to select a single value of the function. The resulting figure displays $[f]$ -domains, where f is the selected isovalue, and typically highlight different regions of space depending on the chosen value. This feature is common to all scalar fields, and appropriate isovalues are either chosen according to educated guesses, or by looking at bifurcation diagrams.¹³³ A bifurcation is achieved when new basins appear, or when two different basins merge together (see Appendix A). DORI bifurcation diagrams can be qualitatively built by looking at the basins evolution when changing the values of the function, as presented in Figure 3.2 for CF_4 .

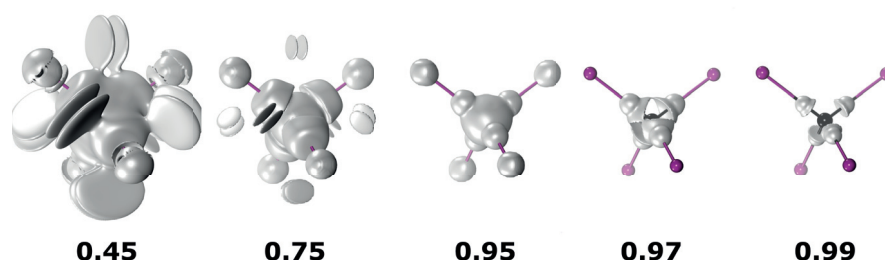


Figure 3.2 – Main DORI bifurcation values for the CF_4 molecule.

Basins stemming from CF bonds are the first visible basins when scanning from $DORI=1$ to $DORI=0$. They rapidly evolve in one global basin surrounding the carbon atom at $DORI[0.97]$, where they merge with the valence-core separation domain around the carbon. At $DORI[0.95]$,

the four valence-core domains of the Fluorine atom appear, while density overlaps stemming from F–F contacts appear as discotic shapes around DORI[0.75]. Finally, most basins are merged together when $\text{DORI} < 0.5$. Thus, the appearance of DORI domains corresponding to chemical interactions are readily visible, allowing for an easy selection of the appropriate DORI[f]-isovalue.

3.2.2 Intramolecular Bonding

An alternative to DORI[f] domains are two dimensional maps color-coded according to DORI values (see Figure 3.3). Such representations are particularly suited for planar systems, which can be visualized in a single 2D representation.

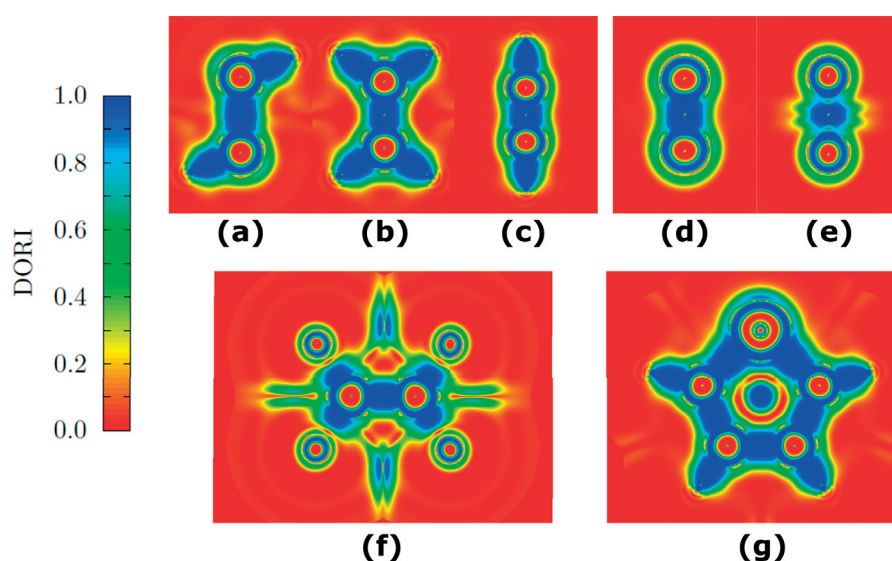


Figure 3.3 – DORI in-plane representation of a selection of small molecules: C_2H_6 (a), C_2H_4 (b), C_2H_2 (c), N_2 (d), O_2 (e), C_2F_4 (f), $\text{C}_4\text{H}_4\text{S}$ (g), computed on electron densities optimized at the PBE0/cc-pVTZ level.

DORI two-dimensional representations provide for intuitive pictures, which allows to qualitatively characterize covalent bonding.⁸ Bond multiplicities are visible within DORI: while C–C single bond are rather lenticular, the DORI basins become more cylindrical with double and triple bonds (see Figure 3.3, a-c). Similarly, the difference between N_2 and (triplet) O_2 bonding is captured by DORI: the bonding basin merges with the shell-valence electron overlap in N_2 , while it barely connects in O_2 (see Figure 3.3 d,e), denoting a weaker covalency for the later. Covalent polar bonds are characterized by bonding basins shifting towards the less electronegative atom, where they merge with its core-valence density overlap, as visible for C_2F_4 (see Figure 3.3 f). The effect is much less pronounced for the Sulfur atom of the thiophene, pinpointing a weakly polar bond between Carbon and Sulfur (see Figure 3.3, g).

Since DORI is based on density overlaps, π -bonds are generally not visible, as atomic densities overlap strongly in the bond axis. Similarly, lone pairs have no DORI signatures, as they don't

form electron density overlaps. However, any interactions with the π -regions or lone pairs still form characteristic basins (see Figure 3.4).

3.2.3 Intermolecular Interactions

DORI evaluates density overlaps regardless of the magnitude of the electron density. This was nicely demonstrated by a scan on the H_2 molecule in DORI's original article,⁸ and is visible in any molecule featuring covalent and non-covalent interactions. For example, while $\rho(\mathbf{r})$ values certainly differ in the covalent and non-covalent regions of a parallel thiophene dimer, DORI=0.9 domains are simultaneously visible in both regions (see Figure 3.4).

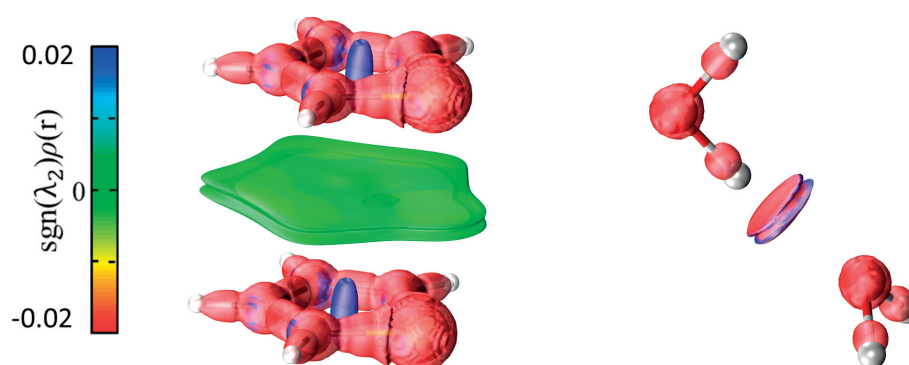


Figure 3.4 – DORI=0.9 isovalue for a thiophene dimer (left) and a water dimer (right), color coded by the $sgn(\lambda_2)\rho(\mathbf{r})$.

As NCI,¹²³ DORI isosurfaces can be color-coded using the sign of the density Hessian second eigenvalue, λ_2 , multiplied by $\rho(\mathbf{r})$. The resulting $sgn(\lambda_2)\rho(\mathbf{r})$ quantity qualitatively displays interactions of attractive or repulsive nature. For example, DORI ring clashes, found at the center of each thiophene in Figure 3.4, appear in blue, hinting the repulsive nature of this density overlap. Conversely, hydrogen bonds and covalent bonds are represented in red, showing attractive interactions. Conclusions exploiting this color-code should be taken with care, especially when considering geometries away from the gas phase equilibrium. For example, molecules might be pushed closer to each other by their environment, and will display higher $sgn(\lambda_2)\rho(\mathbf{r})$ values in intermolecular regions (as $\rho(\mathbf{r})$ becomes larger than in gas phase). However, interaction energies do not necessarily become more attractive.

3.2.4 Effects of Basis Sets and Computational Methods

All computational methods tested, from crude proatomic densities to more elaborate DFT functionals or post-HF methods, and exploiting small or large basis set, provide for comparable DORI signatures: each carbon nuclei (red circle) is bonded with two hydrogen atoms and with the other carbon. Proatomic densities show however quite different patterns than optimized densities (see Figure 3.5), preventing their general use for covalent regions.

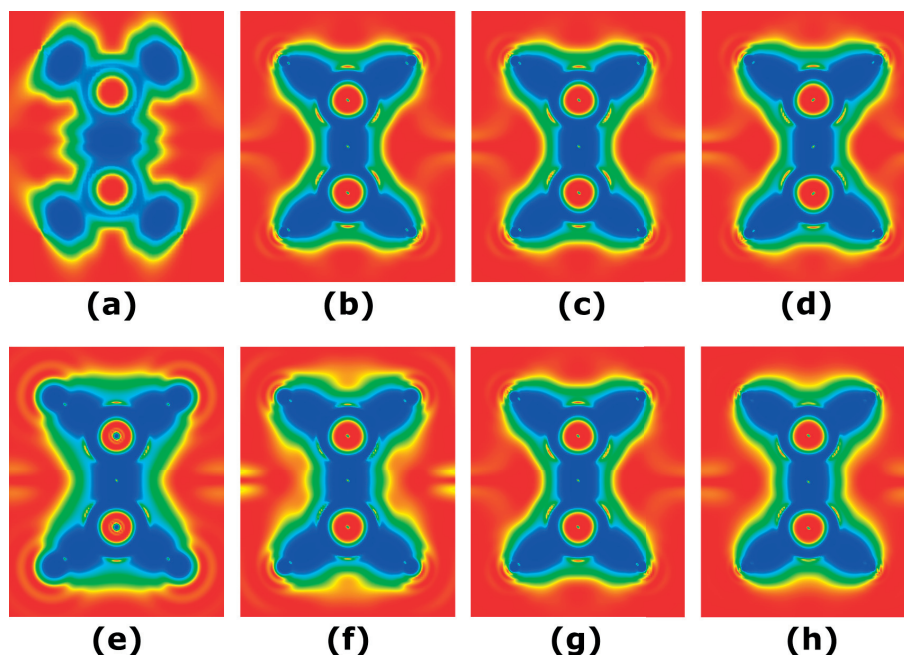


Figure 3.5 – DORI in-plane representation of the C_2H_4 molecule using proatomic densities (a), BLYP (b), B3LYP (c), MP2 (d) and a cc-pVTZ basis set (top). B3LYP densities computed with different basis sets: STO-3G (e), cc-pVDZ (f), cc-pVTZ (g), cc-pVQZ (h) (bottom). All computations exploit B3LYP/cc-pVTZ optimized geometries.

Interestingly, optimizing an electron density with a coarse basis set like STO-3G still provide for reasonably close two-dimensional DORI maps compared with the larger cc-pVQZ basis. Similarly, the use of generalized gradient approximations (GGA), hybrid functionals, or post-HF methods such as MP2 doesn't alter significantly the DORI patterns. Hence, DORI shows a weak sensitivity towards the computational method if the electron density is relaxed, allowing for DORI computation using cost-efficient methods like GGA/double- ζ combination.

3.2.5 DORI Applications

Despite its recent apparition, the range of DORI applications is already broad. Without considering the examples presented in this thesis (Chapter 4-6), our group exploited DORI to construct local hybrid¹³⁴ and meta-generalized gradient approximation functionals.¹³⁰ The electronic compactness, introduced in the original DORI article for organic crystals,⁸ was further applied to indicate a potentially larger transfer rate in organic nanowires.^{135,136}

Other laboratories also showed marked interest for DORI, mostly to investigate chemical interactions. Pertinent examples include (i) the rationalization of CO_2 sequestration by Triazolyldiene-derived N-heterocyclic olefins,¹³⁷ (ii) the evaluation of the conformations present in small bio-organic molecules,¹³⁸ and the assessment of hapticities and hydrogen-hydrogen contacts in Zirconocene related compounds.¹³⁹ Besides its use as visual bonding

3.2. Density Overlap Region Indicator (DORI)

descriptor, DORI was selected as ingredient for quantum mechanics/ molecular mechanics partitioning, where the separation is decided according to chemical interactions captured by DORI patterns.¹⁴⁰

4 Visualizing and Quantifying Interactions in the Excited State

This chapter is based on following publication:

Visualizing and Quantifying Interactions in the Excited State. Laurent Vannay, Eric Brémond, Piotr de Silva and Clémence Corminboeuf, *Chem. Eur. J.* **2016**, 22, 18442 – 18449

4.1 Introduction

The analysis of covalent bonding patterns and intermolecular interactions through electronic structure methods has helped rationalizing a myriad of chemical phenomena. Within this context, the direct analysis of the wavefunction that is an eigenstate of an electronic Hamiltonian provides the complete information about the corresponding stationary state, and thus of the electronic structure of the system (in this particular state). Unfortunately, the wavefunction is an extremely complex object, which depends on the positions and spins of all the electrons; therefore, analyzing details or comparing many-electron wavefunctions is virtually impossible owing to various practical difficulties. To remedy this inconvenience, much effort has been put into connecting electronic structure theory with classical chemical concepts, of which chemical bonding is the most prominent example. The most fundamental approach is to analyze molecular orbitals, a set of one-particle wavefunctions, which appear in most of the electronic structure methods. Another strategy is to condense the relevant information into a single three-dimensional function of space, a molecular scalar field. The common rationale for constructing such fields is to define a measure of electron localization,^{5,6,74,110} which links the results of computations to concepts like bonds, electron cores, and lone pairs. Such descriptors are based on some local representation of the kinetic energy, which is typically computed from molecular orbitals. Whereas these functions have become very insightful for probing the structure of ground states, similar analysis of bonding in the excited state is a field relatively unexplored. Exceptions are the lowest triplet or quintet states^{141–144} of single organic molecules and coordination compounds (*i.e.*, ground-state computations enforcing triplet- or quintet-spin state), and the analysis of benzene and naphthalene excimers¹⁴⁵ by means of the non-covalent interaction index (NCI)⁹ or alternative real-space partitioning (*e.g.*, quantum theory of atoms in molecules QTAIM^{24,146} or the parity function¹⁴⁷), which are

somewhat more cumbersome to interpret.^{148–151} The analysis of excited states using localization functions is limited by the dependence on molecular orbitals, which are not well defined in the excited state. Most popular descriptors like the electron localization function (ELF)⁵ and localized orbital locator (LOL)¹¹⁰ also make a reference to the homogenous electron gas (HEG) model to achieve a dimensionless quantity. These dependencies render the extension beyond ground state situations non-trivial.¹⁵² More recently, methods capable of simulating orbitals in the excited state have been proposed,^{153,154} but they are not yet extensively available. 3D or 2D representation of alternative functions that rely on the electron density and its derivatives and are thus orbital-free have also been proposed,^{9,11,118,123,127,128} but they have yet to be applied to the excited states, as emphasized in this work.

Even if the application of localization functions to excited states was straightforward, the comparison of the ground- and excited-state pictures of localization functions would not necessarily help characterize the nature of an electronic transition. In particular, it would not reveal much information about the changes occurring in regions where the electrons are not well localized (*e.g.*, Rydberg or excimeric states). Often, the relevant question to ask about the excited state is not where the electrons are localized, but rather where they have moved to upon excitation. Answering this question makes it possible to determine the character of the excited state, and thus to distinguish between, for example, local, Rydberg, or charge transfer excitations. Akin to the ground state's analysis, it is a common practice to look at the occupied and virtual canonical orbitals involved in the excitation, but such analysis is very much basis set dependent.¹⁵⁵ A set of powerful methods for analysis of electronic transitions is based on diagonalization of transition and difference density matrices. The examples are natural transition orbitals,^{156–158} and the so-called attachment/detachment densities¹⁵⁹ (see refs. 160 and 161 for an excellent review). Insights into the excited-state characters can also be retrieved from excitation localization distribution,^{162,163} transition dipole moments, and more scarcely from computations in the framework of conceptual density functional theory (*e.g.*, state-specific dual descriptor).¹⁶⁴

As outlined above, the majority of localization descriptors and electronic transition analysis methods rely in practice on the one-electron basis, either directly through orbitals or one-particle density matrices. This is a very convenient representation, as it can directly relate to the particle-hole picture of an excitation. Nevertheless, it is tantalizing to ask what can be learned about an excited state solely from its electron density. This appears to be a much more challenging task because the density itself is rather featureless; its direct analysis does not bring much information about the character of the transition because all the relevant densities look very similar. One possible way of extracting information is to look at density difference, which requires only densities of the excited and ground states. Density difference gives information about the character of the transition, but provides no insight into the bonding and interactions in the excited state. Here, we make a first attempt to unify the description of interatomic and intermolecular interactions with the elucidation of the transition's character by analysis of the geometric features of the electron density. To this end, we employ the density overlap region indicator (DORI),¹²⁷ a bonding descriptor recently proposed by two of us. DORI is a

dimensionless scalar field that depends solely on the electron density, $\rho(\mathbf{r})$, and its derivatives:

$$DORI = \frac{\theta(\mathbf{r})}{1 + \theta(\mathbf{r})} \quad (4.1)$$

where:

$$\theta(\mathbf{r}) = \frac{\left(\nabla \left(\frac{\nabla \rho(\mathbf{r})}{\rho(\mathbf{r})} \right)^2 \right)^2}{\left(\frac{\nabla \rho(\mathbf{r})}{\rho(\mathbf{r})} \right)^6} \quad (4.2)$$

Its values in the $[0,1]$ range make it straightforward to use as well as system independent. Since $DORI=0$ for the hydrogen atom and $DORI=1$ for the uniform electron gas, the values of DORI can be interpreted as a measure of the density inhomogeneity on a range going between these two paradigm densities. Its ability to reveal regions of clash between molecular, atomic, or shell densities (see Figure 4.1) stems from the fact that the density tails of finite systems decay exponentially (hydrogen-like). The overlap of two finite systems (even non-interacting) perturbs the density, which then deviates from the single-exponential behavior and becomes more uniform. Hence, DORI discovers both covalent bonding patterns and non-covalent interactions, and is thus very convenient to analyze both ground- and excited-state phenomena. Recent examples of DORI applications can be found in refs. 138 and 139. It is also worth mentioning that DORI has been successfully used as an ingredient of semi-local and local hybrid exchange-correlation functionals.^{130,134}

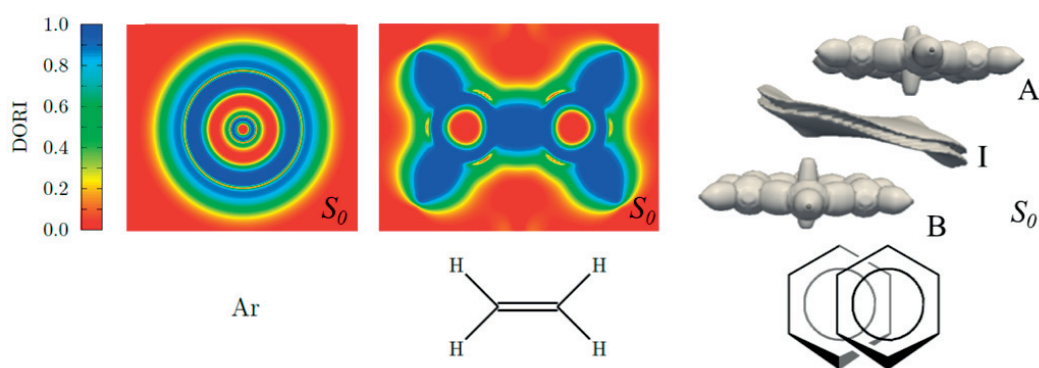


Figure 4.1 – Two-dimensional ground-state DORI maps of the argon atom (left) and in the σ_h plane of the ethene molecule (middle). Three-dimensional representation of the ground-state DORI for the parallel-displaced benzene dimer (right) plotted for $DORI[S_0]=0.95$. DORI computation uses a density self-consistently optimized at the B3LYP/TZP level.

Here, we anticipate that differences in density overlaps will carry information about the character of the excited state, either by appearance of new overlap regions or detectable changes in those already present in the ground state. More specifically, we use DORI to

visualize and quantify the electronic and geometric changes affecting molecular systems upon electronic excitations. For this purpose, we selected prototypical molecules and complexes that exhibit clear excited-state signatures (*e.g.*, Rydberg, $\pi - \pi$, excimer, charge transfer). These examples include pyrrole, aromatic chameleons,¹⁶⁵ excimers formed by (poly-)aromatic hydrocarbons, donor–acceptor complexes, and an iridium dye. The excited state densities are retrieved from time-dependent density functional theory (TDDFT)¹⁶⁶ computations (see computational details). Note that the forthcoming discussion focuses on the use of DORI to characterize the nature of electronic excitation, and not on the problematic energy ordering of these excitations within TDDFT (*e.g.*, Rydberg and charge-transfer states). Still, we verified that the density-based trends that are presented herein are valid regardless of these shortcomings. We also insist that a density-based descriptor like DORI does not rely on any one-particle basis and is thus applicable at any level of theory or even experimental densities. It is compatible with any density computed from wavefunction-theory based methods (*e.g.*, CASSCF, CC,ADC (see *e.g.*, 4.9)), orbital-free approaches, or computations that do not use atom-centered basis sets (*e.g.*, plane-waves, grids).

4.2 Computational Details

Monomers were optimized in their ground states at the ω B97X-D/def2-SVP level^{167,168} in Gaussian09¹⁶⁹ except for the polyaromatic hydrocarbons, which were optimized in the ADF2013.01 code^{170–172} at the B3LYP/TZP level.^{173,174} Excimer geometries were obtained through optimizing the first excited singlet state at the ω B97X-D/def2-SVP level starting from a parallel arrangement of the two monomers at 3.2 Å. The charge-transfer complexes and the iridium dye were optimized at the ω B97X-D/def2-SVP level. The LANL2DZ basis set was used to describe the iridium atom. All the ground-state DFT densities were self-consistently optimized with standard convergence criteria by a Kohn–Sham procedure as implemented in ADF2013 and Gaussian09. With each software, excited-state densities were obtained by adding to the converged DFT wavefunction the necessary Z-vector contribution derived from a coupled-perturbed Kohn–Sham (CPKS) calculation to produce the relaxed density for state N.^{78,175} The DORI_{int} values were computed by a numerical integration of the density within a DORI basin using a 0.1 au mesh grid with a locally modified version of DGRID[53] available on demand. The Paraview software¹⁷⁶ was used to obtain a visual representation of the DORI function. Alternatively, DORI is now available for ground states in ADF2016.¹⁷⁷

4.3 Results and Discussion

4.3.1 Molecular Excitations

Rydberg excitations provide the first illustrative class of patterns elegantly captured by DORI. Taking pyrrole as a prototypical example,^{178–180} we show that those diffuse excitations are easily recognizable by the formation of a characteristic DORI basin located around the molecule

(Figure 4.2).

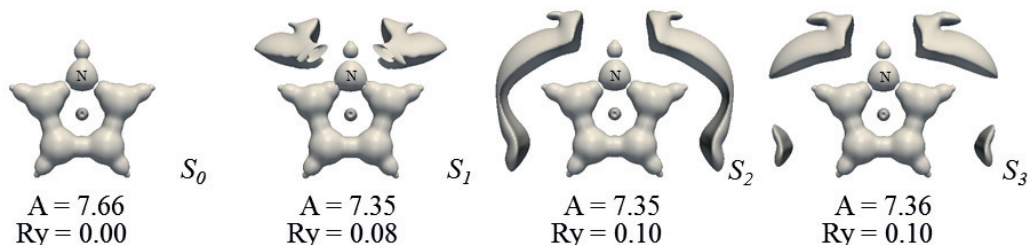


Figure 4.2 – DORI=0.85 isosurface and $DORI_{int}(^1S_n; V_{0.85})$, $n \in \{0, 1, 2, 3\}$ for the pyrrole in its ground and the first three (Rydberg) excited-state singlets computed at the (TD)-PBE0/TZVP-aug level on the ω B97X-D/def2-SVP ground state optimized geometries. The nitrogen atom position is indicated by “N”, and $DORI_{int}$ for molecular (A) and Rydberg (Ry) basins are given in the figure.

This density clash originates from the overlap between the newly populated Rydberg region and the valence electrons. At the chosen TD-PBE0¹⁸¹/TZVP-aug level (see ref. 182 for additional discussion), the first three excited-state singlets of pyrrole have a Rydberg signature (see Figure B.1 in Appendix B for molecular orbitals and density differences). The clash of the first excited state S_1 (1A_2) (HOMO (π) LUMO (3s)) is essentially localized around the nitrogen atom. The DORI picture after excitation to S_2 (1B_1) or S_3 (2A_2) reveals a dominant Rydberg 3p_y and 3p_z character, respectively, in line with the molecular orbital picture. Beside the typical Rydberg domains, DORI is also capable of probing the pyrrole covalent bonding regions that remain basically unchanged upon excitation. Along with the visual signature, a more quantitative analysis can be achieved through integrating the electron density, $\rho(\mathbf{r})$, within the molecular or Rydberg regions defined by a DORI isosurface V_{iso} such as:

$$DORI_{int}(V_{iso}) = \int_{V_{iso}} \rho(\mathbf{r}) d\mathbf{r} \quad (4.3)$$

Upon excitation to a Rydberg state, $DORI_{int}$ is compatible with a loss of electrons in the molecular basin (A) (within an isosurface) in favor of the Rydberg basin(s) (Ry). While the obtained numbers obviously depend on the chosen isovalue, the trend for different excited states at the same isovalue reflects the change in density rearrangement as compared to the ground state.

The electronic structure of the ground (S_0) and first $\pi - \pi$ singlet-excited (S_1) states of biphenylene is a related study case with more pronounced visual changes. As depicted in Figure 4.3, the ground state of biphenylene closely resembles two isolated benzene rings with equalized bond length connected by two single bonds. The DORI isocontour map reveals an imperfect conjugation,

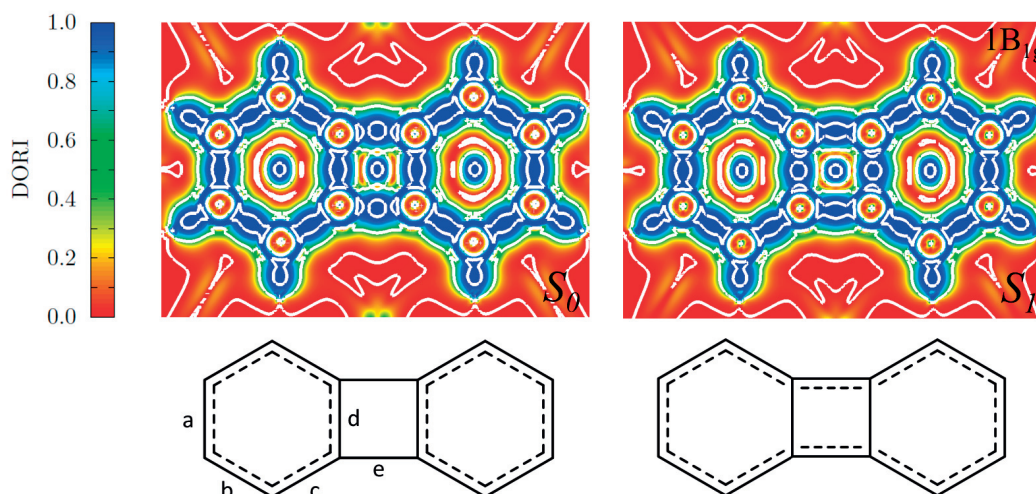


Figure 4.3 – Two-dimensional ground (top left) and excited (top right) state DORI maps in the σ_h plane of the biphenylene molecule. Isocontour lines of $\text{DORI}[\rho] \in \{0.01, 0.50, 0.99\}$ are plotted in white. All the structures are optimized at the (TD-)B3LYP/TZP level, and the relaxed densities to compute DORI are obtained at the same level. Bottom left and bottom right Lewis structures represent the two schematic electronic delocalizations estimated according to the bond length patterns in the ground and excited state, respectively. Bond lengths for ground (excited) state (in \AA): a=1.38 (1.43), b=1.42 (1.38), c=1.37 (1.40), d=1.42 (1.49), e=1.51 (1.41).

which arises from a compromise between maximizing the conjugation behavior in the 6-membered ring and diminishing the antiaromatic behavior in the central cyclobutadiene. In sharp contrast, the adiabatic excitation to the first singlet $\pi - \pi$ state leads to a Baird-aromatic 12π electron ring, illustrated by the equalized carbon–carbon-bond DORI domains in the periphery. This result is in line with Baird's rules¹⁸³ and previous experimental and computational studies¹⁸⁴ (see also the exhaustive review¹⁶⁵), which ascribe an aromatic character to excited-state biphenylene and related molecules.^{185–188} The structural rearrangement is pronounced, but the pure electronic effects visible upon vertical excitation are non-negligible, especially in the region of large π density (see Figure B.2 in Appendix B). The biphenylene example convincingly shows that information on the bonding patterns in the excited state can be obtained solely from the electron density.

4.3.2 Excited-state Complexes

The formation of excimers and exciplexes are alternative typical examples of excited-state phenomena occurring between molecules. These excited-state complexes, which are more strongly bound than their van der Waals ground state minima, possess characteristic lifetimes and light emission properties.^{189,190} The binding energy is nevertheless rather weak, in the order of $5\text{--}20 \text{ kcal mol}^{-1}$ in polyaromatic hydrocarbons (PAHs), and strongly depends upon the geometrical arrangement of the two involved monomers.^{191–198} DORI is used to provide

a characteristic fingerprint for the formation of excimers, and to identify the nature of the interactions between molecules. Hence, the focus is on the intermolecular DORI domain, where the excimer interaction does occur. Figure 4.4 displays color-coded DORI taken in the plane parallel to the intermolecular domain of the anthracene dimer.

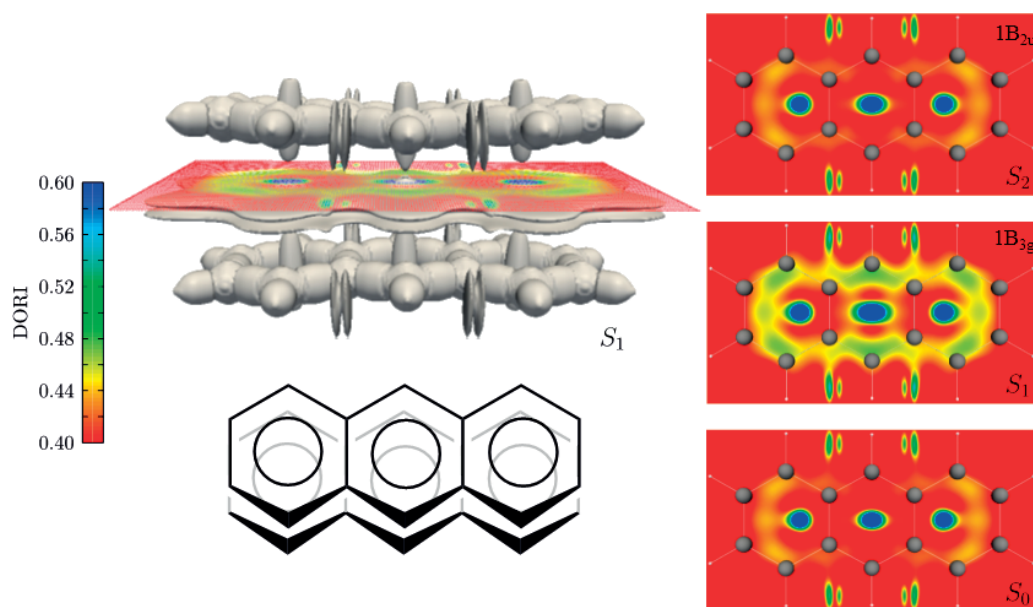


Figure 4.4 – Three-dimensional representation of the excited-state DORI for an anthracene excimer plotted for $\text{DORI}[\rho_{S_1}] = 0.7$ (left). Two-dimensional ground- and excited-state DORI maps obtained from relaxed S_0 , S_1 ($1B_{2g}$) and S_2 ($1B_{2u}$) (TD-)PBE0/TZP densities (right). The excimer geometry is optimized at the TD- ω B97X-D/def2-SVP level.

In order to decouple the geometrical and electronic effects, the optimized geometry of the excimer was kept frozen in the S_1 (*i.e.*, first excimeric) state, and the DORI maps plotted for the S_0 , S_1 (HOMO–LUMO, at the TD-PBE0/TZP level,¹⁸¹ see Figure B.3 in Appendix B for the orbital pictures), and S_2 (mixed excitation HOMO-1 LUMO and HOMO LUMO) electronic states of the anthracene dimer. The S_1 state has a typical DORI signature, arising from the clearly visible density overlap increase in the intermolecular region. The enhanced π -density overlap is especially apparent above the carbon perimeter (green region, Figure 4.4), with little participation from the two central bonds. The same pattern characterizes the excimeric states of other PAHs such as pyrene, perylene, or benzene (see Figure 4.5). In contrast, the DORI maps for the ground and non-excimeric S_2 excited states of anthracene show a much weaker density overlap. The insights provided by DORI are in line with the electron density difference shown in Figure 4.6, but somewhat easier to interpret. Note that the stronger transannular interactions in the excimeric states identified here were not captured in the QTAIM and NCI analyses mentioned earlier.¹⁴⁵ The integral values within the intermolecular domain have already served to compare the DORI-based electronic compactness in quatertiphenylene crystals.⁸ In the present case, we compare the DORI_{int} within three domains, the individual

molecules and the intermolecular regions (see A, B, and I in Figure 4.1), in the ground and excited states. The integral variations between the two states can be readily interpreted as a change in the electron number in each region (within an isosurface). As the data in Table 4.1 shows, all the excimeric states are characterized by a significant loss of electron in the monomers and an increase in the intermolecular region when compared to the ground state. This trend, which is of purely electronic origin, is reflective of the formation and even the magnitude of a bonding region between the dimers.

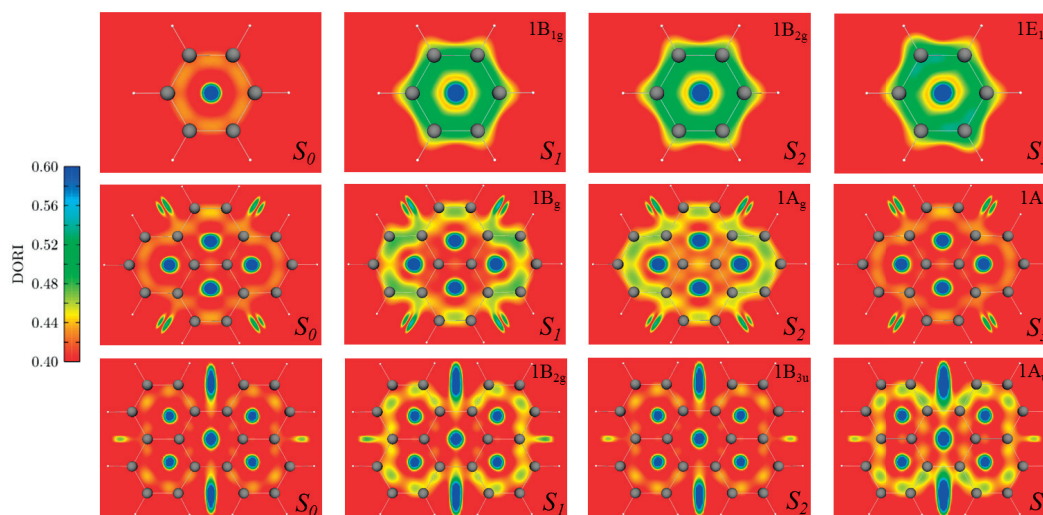


Figure 4.5 – DORI maps in the intermolecular plane for the benzene (top), pyrene (middle), and perylene (bottom) dimers, using the (TD-)PBE0/TZP densities computed on the S_1 excimer ω B97X-D/def2-SVP optimized geometry.

From the integral values, it can also be deduced that the three lowest singlet excited states of the benzene dimer are excimeric, with a stronger interaction between the two monomers (large integral values), whereas negligible integral values (<0.5) are found in the intermolecular domain (I) of the local excitations of other complexes (*e.g.*, S2 and S3 in pyrene–pyrene and anthracene–anthracene). These variations are also visible in the DORI maps (see Figure 4.5).

Charge transfer (CT) excited states between donor (D) and acceptor (A) organic molecules along with metal-to-ligand charge transfer (MLCT) transitions in an iridium(III) dye are the last test cases investigated in this study. In this context, DORI is complementary to other indexes, which serve to measure the spatial extent of charge transfer within molecules.^{199–204} We first consider complexes formed by an aromatic donor (benzene, naphthalene, and anthracene) and the tetracyanoethylene (TCNE) acceptor. For these complexes, the density-based descriptor naturally provides an intermolecular zone that can serve to identify charge-transfer excitations. This intermolecular DORI clashing region shifts toward the charge-depleted donor upon the formation of the $[D^+A^-]^*$ excited complex.

This is consistent with the fact that the acceptor's density expands after excitation because it carries more electrons. A similar pattern is obtained for ionic bonds (see, for example, LiF in

Table 4.1 – $\Delta DORI_{int} = [DORI_{int}(\rho_{S_n}; V_{0.85}) - DORI_{int}(\rho_{S_0}; V_{0.85})]$ in millielectrons are computed for molecular (A,B) and intermolecular (I) basins for a series of excimer and charge transfer complexes using relaxed (TD-)PBE0/cc-pVDZ and (TD-)CAMB3LYP/cc-pVDZ densities, respectively. All charge transfer ground state structures and the excimer first excited state structure were optimized at the (TD-) ω B97X-D/def2-SVP level. The geometries of the first excimeric states optimized at the (TD-) ω B97X-D/def2-SVP level are used for the excimers.

| Systems | S_1 | | | S_2 | | | S_3 | | |
|---|--------|-------|-------|--------|-------|-------|--------|-------|-------|
| | A | I | B | A | I | B | A | I | B |
| benzene _(A) -benzene _(B) ^[a] | -37.5 | 37.3 | -37.5 | -46.9 | 39.6 | -46.9 | -43.2 | 40.4 | -43.2 |
| anthracene _(A) -anthracene _(B) ^[a] | -40.5 | 28.2 | -40.5 | -12.1 | 4.5 | -12.1 | -36.3 | 28.6 | -36.3 |
| pyrene _(A) -pyrene _(B) ^[a] | -53.5 | 19.8 | -53.5 | -41.8 | 25.6 | -41.8 | -13.4 | 1.0 | -13.4 |
| perylene _(A) -perylene _(B) ^[a] | -29.4 | 22.7 | -29.4 | -4.6 | 4.0 | -4.6 | -43.0 | 31.9 | -43.0 |
| benzene _(A) -TCNE _(B) ^[b] | -191.6 | -49.8 | 62.8 | -164.8 | -52.7 | 58.8 | 1.7 | -15.4 | -57.9 |
| naphthalene _(A) -TCNE _(B) ^[b] | -152.1 | -26.5 | 57.4 | -160.0 | -25.4 | 60.5 | -147.7 | -19.1 | 53.2 |
| anthracene _(A) -TCNE _(B) ^[b] | -68.4 | -47.6 | 47.7 | -126.2 | -55.5 | 58.5 | -13.8 | 2.8 | 0.0 |

[a] Excimer type. [b] Charge-transfer type.

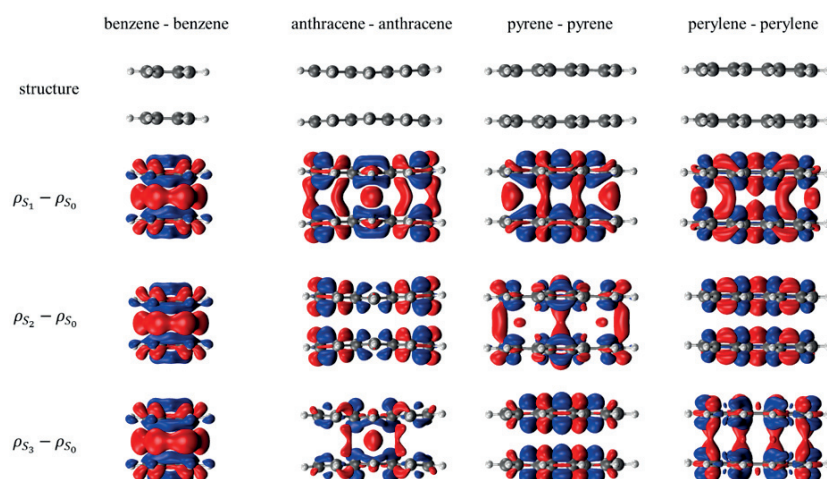


Figure 4.6 – Density differences ($\rho_{S_n} - \rho_{S_0}$, $n \in \{1, 2, 3\}$) at the PBE0/cc-pVDZ level for the excimer complexes in their first singlet excited-state TD- ω B97X-D/def2-SVP optimized geometry. Isodensities=+0.0005 (red) and -0.0005 (blue).

Figure 4.7) and ground-state charge-transfer complexes. Taking the benzene-TCNE complex as an illustration, Figure 4.7 shows that the overlap of the two molecular density tails, and consequently the DORI clashing region, is shifted towards the donor in the $\pi - \pi^*$ charge-transfer excited states (S_1) (see Figures B.4–B.7 in the Appendix B for the density differences and the molecular orbital pictures). This qualitative picture is nicely complemented by the integration of the electron density within the three DORI domains (Table 4.1).

For the three considered charge-transfer complexes, the trend is highly systematic and insightful: overall, the charge-transfer excited states coincide with a decrease/increase in the number of electron within the donor/acceptor (A/B) in comparison with the ground state. Concurrently, the "I" integral decreases, thus reflecting the fact that the domain moves towards the electron donor, which has lost electron density. In a sense, this clash now reveals a concrete loss of electronic charge near the donor. Amongst the nine excited states investigated in Table

4.1, only the S_3 of the benzene–TCNE and anthracene–TCNE complexes correspond to a local excitation.

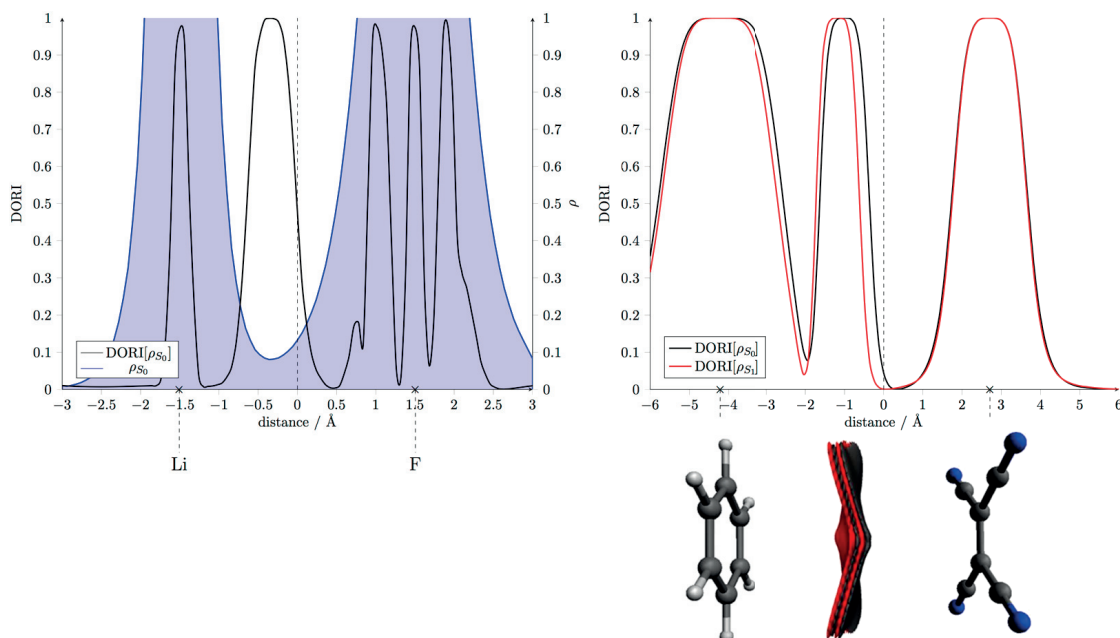


Figure 4.7 – One-dimensional ground-state (ground and excited states) DORI maps for the ionic LiF (left) and charge-transfer benzene–TCNE complex (right) plotted along the C_n axis of the system. Relaxed densities to compute DORI are obtained at the (TD-)CAM-B3LYP/cc-pVDZ level (bottom): Superposition of $\text{DORI}[\rho]=0.9$ in S_1 excited state (red) and ground state (black) for the tetracyanoethylene–benzene dimer at the (TD-)CAM-B3LYP/cc-pVDZ level. The charge transfer is shown to induce a displacement of the DORI intermolecular basin towards the donor molecule.

These excitations, located on the TCNE and anthracene, respectively (see electron density picture), are well captured by the DORI integrals that show a significant variation on the domain in which the local excitation occurs, but no change in the other molecular moiety or in the intermolecular domain. A somewhat weaker charge-transfer character of S_1 in anthracene–TCNE is also detected both by the DORI_{int} and the electron-density difference.

Similar analyses enable the identification of $^1\text{MLCT}$ excitations, such as those relevant to typical cyclometalated iridium(III) dyes. In the representative case visible in Figure 4.8, the $^1\text{MLCT}$ nature of the first allowed transition (3.6 eV, $f=0.1$) can be identified by considering the metal- (M) and ligand- (L) centered DORI integrals. The DORI integrals on the metal domain decrease upon excitation to S_1 , whereas the one on the pyridine-containing ligand increases significantly.

In contrast, the character associated with the phosphorescence from the (optimized) T_1 states is essentially of ligand-centered character (see, for example, ref. 205) with no significant change in the DORI integrals associated with the iridium atom. This interpretation can indeed

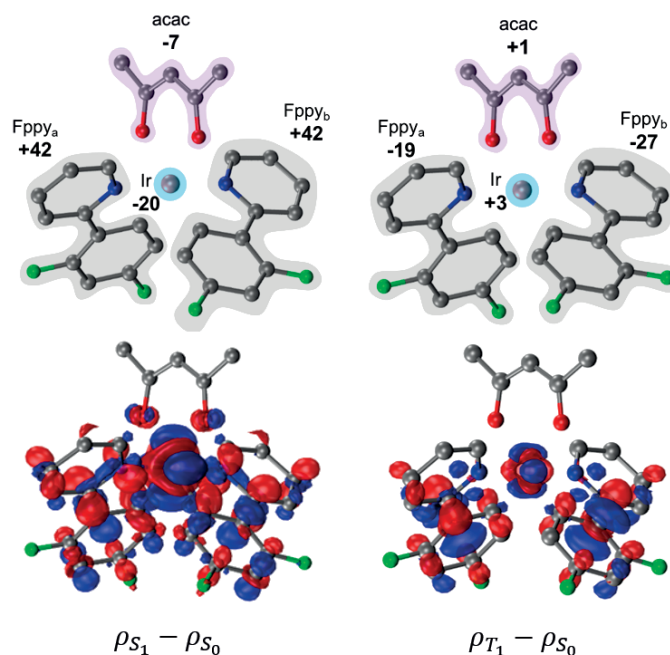


Figure 4.8 – $\Delta DORI_{int} = [DORI_{int}(\rho_{X_1}; V_{0.85}) - DORI_{int}(\rho_{S_0}; V_{0.85})] \cdot 1000$ in millielectron (X=S,T) in the schematic DORI regions for Iridium (Ir), acetylacetonate (acac), and 2-(2,4-difluorophenyl)pyridine (Fppy_{a,b}) (top). Density differences for the first singlet and optimized triplet excited states; isodensities = + 0.002 (red) and -0.002 (blue) (bottom). The scalar fields were computed for absorption (left, S₀ → S₁ in S₀ geometry) and emission (right, T₁ → S₀ in the T₁ geometry) using the relaxed (TD-)CAM-B3LYP/cc-pVDZ densities. The complexes were optimized in the ground state and first triplet at the (TD-)ωB97X-D/def2-SVP level.

be validated by the electron-density difference (Figure 4.8, bottom) and by the molecular orbital pictures (see Figures B.9 and B.10 in Appendix B). Overall, it is very appealing to see that the consideration of the three DORI integrals can be used to distinguish between different excited-state characters without relying upon the orbital picture.

4.4 Conclusion

The first application of DORI to excited-state situations is appealing. It allows an intuitive representation of the electronic and geometric modification occurring after electronic excitation processes in organic molecules solely based on their electronic density and its derivatives. The character of single-molecule excitations is easily identifiable. Similarly, excimer formation can clearly be captured through a visual fingerprint derived from DORI scalar fields, giving insights into the stacking behavior of these complexes. The impact of the intra- or intermolecular excited-state processes on the density can also be analyzed through integration of the (inter)molecular DORI basin, which is altered upon excitation. A net-electron loss or gain is observed in the DORI basins characteristics of the transition, providing a straightforward tool for the analysis of excited-state complexes.

4.5 Fluorescence Quenching in BODIPY Dyes

This paragraph is based on the following publication: Fluorescence Quenching in BODIPY Dyes: The Role of Intramolecular Interactions and Charge Transfer Antonio Prlj, Laurent Vannay, Clemence Corminboeuf *Helv. Chim. Acta*, **2017**, 100, 6, e1700093.

Previous applications validated DORI as an ideal descriptor for characterizing excited state phenomena, which prompted its use to rationalize puzzling photoemission properties of BODIPY derivatives. Functionalization of BODIPY significantly alters its fluorescence properties: quantum yield, Φ_f , can be increased by attaching an alkyl-, alkynyl-, or halosubstituent to the *meso* position, or decreased through the attachment of alkenyl- or aryl- groups.

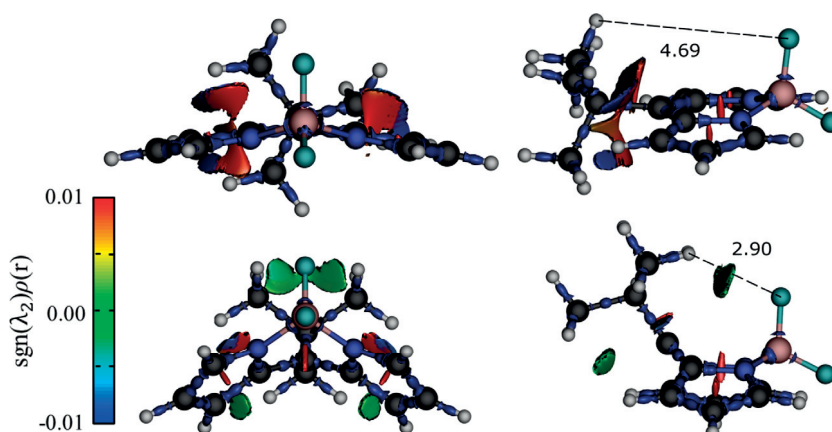


Figure 4.9 – Three-dimensional DORI representation (isovalue=0.995) of *tert*-butyl-BODIPY in ground state minimum (top) and near the conical intersection (bottom) geometries. In the DORI isosurfaces blue represents attractive and red repulsive interactions. The shortest hydrogen – fluorine distance [Å] is indicated by a dashed line. Computations at the MP2/ADC(2) / def2-SVP level.

Meso-substituted *tert*-butyl-BODIPY is a notable exception, however, since it bears a low Φ_f , large Stokes shifts and broad fluorescence peak, which contrasts typical BODIPY and alkyl-BODIPY fluorescence. Computed excited state energy profiles at both the CASSCF²⁰⁶ and ADC(2)²⁰⁷ levels reveal that *tert*-butyl-BODIPY directly relaxes from the S_1 to S_0 without an energy minimum. The minimum energy crossing point (MECP) lies lower than the FC, resulting in fluorescence quenching.

The origins of the low-lying MECP have been revealed using DORI. In the S_0 geometry, steric clashes are present between the BODIPY ring and the bulky *tert*-butyl groups (Figure 4.9, red domains), which destabilize the ground state and the Franck-Condon region in excited state. At the crossing geometry, the *tert*-butyl groups are splayed from the BODIPY core, which reduces steric clashes. Moreover, DORI finds a new interaction between the two *tert*-butyl groups and the BODIPY fluorine atom (Figure 4.9, blue-green domains) near the MECP

structure. This primarily directional electrostatic interaction further reduces the MECP energy relative to the FC region, resulting in a favored non-radiative deactivation pathway.

Both the reduction in steric clash and CH₃-F interactions in *tert*-butyl-BODIPY are enhanced by the distorted structure found near the MECP, typical of BODIPY and its derivatives. DORI maps of the BODIPY rings at the *S*₀ and MECP geometries indicate that the principle driving force for this bending is a reduction in the CC bond order (particularly for the *meso*-C atoms) near the MECP (Figure 4.10).

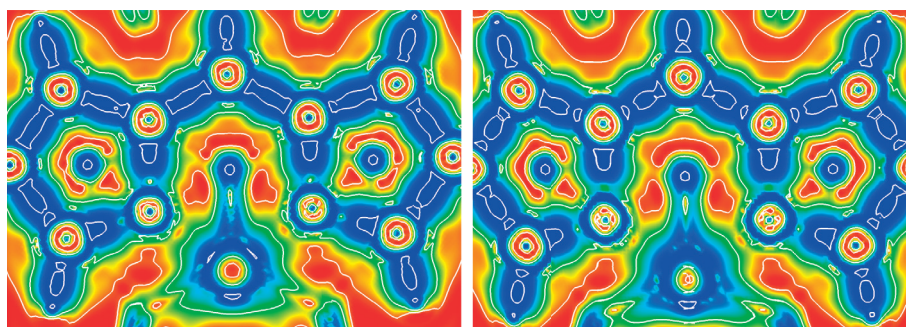


Figure 4.10 – Two-dimensional DORI map of BODIPY in *S*₀ (left) and MECP (right) geometries. White contour lines (DORI=0.99) indicate the bonding pattern as being quasi-aromatic for the ground state, while the bond order is reduced in the excited state. Computations at the MP2/ADC(2)/def2-SVP level.

The bending that occurs near MECP of BODIPY and its derivatives typically increases the energy of the conical intersection and hampers nonradiative decay. However, some *meso*-substituents are able to stabilize the MECP structures, which promotes internal conversion processes and quenches the fluorescence. DORI was able to rationalize this behavior by pinpointing (i) a reduction in steric clashes and (ii) formation of a new CH₃-F intramolecular non-covalent interaction near the MECP of *tert*-butyl-BODIPY.

5 Analyzing Fluxional Molecules using DORI

This chapter is based on following publication:

Analyzing Fluxional Molecules using DORI. Laurent Vannay, Benjamin Meyer, Riccardo Petraglia, Giuseppe Sforazzini, Michele Ceriotti and Clémence Corminboeuf, *submitted*

L. Vannay did the DORI analysis, using MD trajectories from R. Petraglia. Sketchmap were computed by M. Ceriotti. B. Meyer did the AdNDP orbital localization.

5.1 Introduction

Quantum chemical approaches generally rely upon the wavefunction or the electron density, which are both intricate to interpret. The wavefunction is indeed a complex multidimensional object, while the electron density is rather featureless.^{3,7,208–213} One way to overcome this conundrum is to take advantage of molecular scalar fields, which condense the chemically relevant information obtained from quantum calculations into one single intuitive real space function (see Figure 5.1).

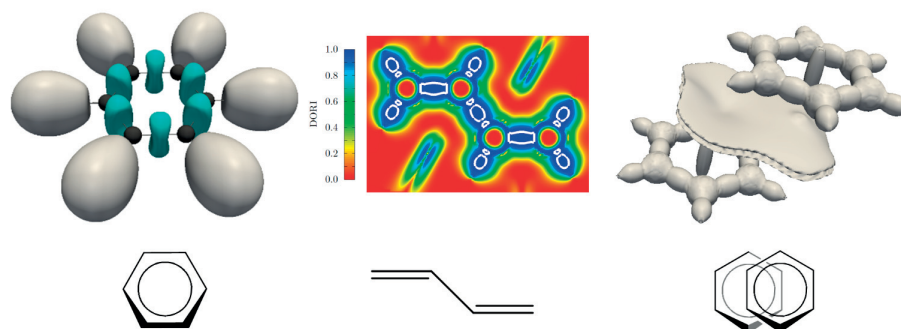


Figure 5.1 – Three-dimensional representation of the benzene plotted for ELF= 0.8 (left), two-dimensional DORI maps in the σ_h plane of the butadiene with DORI=0.99 isocontour in white (center) and three-dimensional representation of the parallel-displaced benzene dimer for DORI=0.95 (right). Electron densities are self-consistently optimized at the B3LYP/TZP level.

The most illustrative molecular scalar field is certainly the Electron Localization Function (ELF),^{5,6,51} which identifies regions where electrons locate⁵ and classify chemical bonds.⁶ Different localization measures such as the Localized Orbital Locator (LOL),¹¹⁰ the Parity Function (P),^{147,214} the Electron Pair Localization Function (EPLF),¹⁰⁴ the Localized Electron Detector (LED),¹¹⁸ the Electron Localizability Indicator (ELI)⁷⁴ or the single exponential decay detector (SEDD)¹¹ have reinforced the interpretative power of scalar fields, while also extending their range of applications to post-Hartree-Fock (*e.g.*, ELI),⁷⁴ quantum Monte Carlo (*e.g.*, EPLF)¹⁰⁴ and orbital free formalisms (*e.g.*, LED, SEDD).^{11,118}

The aforementioned scalar fields identify regions where electrons locate, which by design, precludes their identification of non-covalent regions where electrons are not well localized. The Non Covalent Interaction index (NCI)⁹ was developed to fill this gap by specifically highlighting regions of low electron density gradient and low densities. Other approaches revealing covalent bonding patterns and non-covalent interactions simultaneously also exist, either through coupling different scalar fields (*e.g.*, ELF and NCI)^{125,126} or through stand-alone methods like the versatile Quantum Theory of Atoms and Molecules (QTAIM).^{24,43,146,215} This work exploits another powerful scalar field, the Density Overlap Region Indicator (DORI),⁸ introduced by de Silva and Corminboeuf, which was derived from the single exponential decay detector.^{11,127,128} In short, DORI captures regions of space where the electron density between atoms, molecules or atomic shells clashes. Such regions are characteristic of covalent and non-covalent interactions, both of which are revealed by DORI in the same value range. The scalar field probes geometrical features of the electron density in these overlapping regions by measuring the deviation from a single-exponential decay. The descriptor is dimensionless and solely dependent upon the electron density and its derivatives:

$$DORI = \frac{\theta(\mathbf{r})}{1 + \theta(\mathbf{r})} \quad (5.1)$$

where

$$\theta(\mathbf{r}) = \frac{\left(\nabla \left(\frac{\nabla \rho(\mathbf{r})}{\rho(\mathbf{r})} \right)^2 \right)^2}{\left(\frac{\nabla \rho(\mathbf{r})}{\rho(\mathbf{r})} \right)^6} \quad (5.2)$$

Thus, DORI is well defined at any level of theory, and can also be exploited with orbital-free approaches as well as proatomic and experimental densities.²¹⁶ It is worth noting that a physical interpretation of DORI has been provided in terms of the local wavevector,^{115–117} which reflects the shape of the electron density.

Molecular scalar fields have generally proved to be both insightful and reliable in a comprehensive range of applications. They can distinguish between different classes of chemical bonds^{58,60} including metal-metal,^{217,218} metal-ligands,^{219,220} organic,^{75,138,139,221–223} ionic,³⁸ or multicenter.⁶² Moreover, they also reveal non-bonding interactions such as *e.g.*, hydrogen^{69,71,123} or halogen bonds.^{224–227} and have helped rationalize chemical reactivity involving

e.g., cycloaddition,²²⁸ hydrogen transfer,²²⁹ or electron transfer²³⁰ mechanisms, in systems ranging from organic^{229,231–233} to metallic.^{234,235}

The range of DORI applications is comparably broad and includes: the construction of different classes of exchange-correlation functionals^{130,134} and adaptive QM/MM schemes,¹⁴⁰ the characterization of nanomaterials,¹³⁵ the classification of excited states,^{12,207} the identification of fingerprints associated with CO₂ sequestration by organic molecules¹³⁷ the conformational behavior of small bio-organic molecules,¹³⁸ hydrogen-hydrogen contacts in zincocene related compounds.¹³⁹

Each of the aforementioned applications essentially rely upon a traditional “static” quantum chemistry picture, in which only one or a handful of gas phase 0K structures are considered. Yet, aside from a few cases involving small and rigid molecules, static representations of chemical processes may not provide a comprehensive picture. Indeed, there are many interesting phenomena that involve highly fluxional molecules where thermal motion heavily influence molecular properties. Examples include the subtle relative energy prediction of polymorphic crystal structures of floppy molecules,²³⁶ the world of molecular actuators^{237–243} as well as organocatalytic processes,²³⁶ each of which all evolve on complex potential energy surfaces.

For those systems, the static description are insufficient¹³⁶ and molecular dynamic (MD) trajectories become necessary. Of course, fluxional processes could still benefit from insights provided by molecular scalar fields as has been occasionally shown. One relevant example is Bonding Evolution Theory (BET),^{244,245} which is a combination of ELF and the catastrophe theory²⁴⁶ used to discriminate specific events during a reaction processes (*e.g.*, bond formation or dissociation) and can be used to discriminate specific events during a reaction processes (*e.g.*, bond formation or dissociation). Given the importance of non-covalent interactions an ELF/NCI cross interpretative BET strategy was also recently employed to monitor the full range of interactions.¹²⁵ While BET does add significant insight into chemical reaction,^{232,247,248} its applications have been constrained to intrinsic reaction coordinates, which facilitate easy understanding of reaction mechanisms, but does not necessarily reflect dynamical processes. As mentioned by Piquemal and *co.*¹²⁵ BET is, in principle, applicable to MD trajectories, but this possibility awaits further exploration.

The averaged NCI index (aNCI),²⁴⁹ an extension of the existing NCI framework, is another strategy, which accounts for the fluctuation of the environment around a target molecule. Within aNCI, the environment is allowed to fluctuate while the geometry of the solute molecule is kept frozen. As such, aNCI effectively samples the solute-solvent fluxional interactions for a given solute geometry, but is unable to describe the inherent fluxionality of a solute molecule.

The only example exploring the effects of dynamical fluctuations on ELF and QTAIM was a prototypical SN₂ reaction by Adamo and co-workers.²⁵⁰ In this work, the “crucial role of the electron charge transfers during the formation of the ion-dipole complex”²⁵⁰ was properly described only by the dynamical analysis. Still, the system investigated (chlorine exchange in chloroform) had a limited number of degrees of freedom. Along a similar line, the pioneering

ELF investigation of Marx and Savin,¹³³ on the elusive bonding of the “highly fluxional” CH_5^+ molecule should be mentioned. The authors analyzed a “statistical sample” of 64 molecules extracted from an MD trajectory to clearly distinguish between the three-center, two-electron H_2 -C bond, from the remaining three two-center, two-electron CH bonds.

This number of examples present in the literature already illustrates the suitability of using bonding descriptors beyond traditional static quantum chemical situations. The present work goes one step further and demonstrate the usefulness of DORI⁸ to analyze covalent bonding patterns and non-covalent interactions in three highly fluxional systems (5.2).

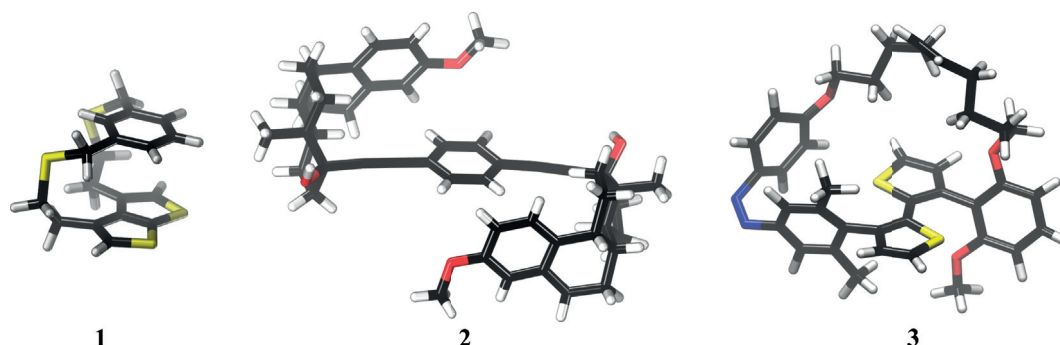


Figure 5.2 – Three-dimensional representation of Thieno-[2,3-b]-thiophene (**1**), a molecular rotor (**2**) and a photochromic torsional switch (**3**).

The first example is a dithiacyclophane (**1**)^{251–253} that is dominated by low energy conformations characterized by different extent of π -stacking interactions that are well described by DORI. For the molecular rotor (**2**),^{253,254} DORI is used to fingerprint and discriminate between the compact enthalpy-driven structures and the disordered conformations. Finally, DORI is used to examine the fluctuating π -conjugation pathway of a photochromic torsional switch (PTS, **3**).²⁵⁵

5.2 Computational Details

The molecular dynamics trajectories of 1-3 were performed using Born-Oppenheimer MD (BOMD) at the DFTB3 level,^{256–258} as well as the REMD@DFTB variant,^{255,259} that combines Density Functional Tight Binding (DFTB3) in DFTB+²⁶⁰ with Replica Exchange Molecular Dynamics (REMD, parallel tempering) powered by i-PI.^{261,262}

REMD performs several molecular dynamic trajectories (*i.e.*, replica) at different temperature with each replica being able to exchange its atomic positions and velocities each of the other replicas. The algorithm dictating the exchange keeps all the replicas in the respective canonical ensemble for the targeted temperature. For **1** and **2**, the trajectories were taken directly from ref. 253, while for **3** trajectories are based on from ref. 255. We analyzed the gas phase trajectories at 300K for **1** and **3**, and at 310K for **2**.

The BOMD trajectories of **1** ran for 5.4×10^6 steps assembled from 54 equivalent simulations initiated with random configurations generated from previous BOMD. REMD temperature ranges from 300K to 1500K with 16 replicas (2×10^5 steps/replica) for **1**, and 48 replicas (1.5×10^5 steps/replica) for **2**. A Langevin thermostat with a time constant of 100 fs kept each replica at a constant temperature. For **3**, the REMD temperature ranged from 300K to 1200K using 32 replicas (1.5×10^5 steps/replica), and a GLE thermostat²⁶³ to improve the mapping. For all three systems, a time step of 0.25 fs was found to be sufficient to avoid any drift in the conserved quantity while integrating the Newton equations. All forces were computed at the DFTB3/3OB level,^{264,265} with the dispersion correction based on the Universal Force Field parameters²⁶⁶ as implemented in the DFTB+ code.²⁶⁰

The REMD@DFTB3 trajectories at the targeted temperature are then post-processed exploiting DORI. All electron densities used for DORI were computed at the PBE/6-31G* level in Gaussian09 on a subset of random snapshots extracted from the REMD or MD trajectories. The quantitative analysis was performed by integrating the electron density or considering the volume associated with the relevant DORI domains defined by a given DORI isovalue (V_{iso}):

$$DORI_{int}(V_{iso}) = \int_{V_{iso}} \rho(\mathbf{r}) d\mathbf{r} \quad (5.3)$$

$$DORI_{vol}(V_{iso}) = \int_{V_{iso}} d\mathbf{r} \quad (5.4)$$

For all systems, DORI, $DORI_{int}$ and $DORI_{vol}$ were computed on a locally modified version of DGRID-4.6, with a precision of at least 10points/Bohr. The isovalue taken for each system was chosen such as the basin representative of the targeted interaction remains separated from the other domains. The quantitative analyses are thus dependent upon the chosen isovalue, but the robustness of the trends persists for any isovalue leading to similar domain separations. In the case of the dithiacyclophane (**1**) and rotor (**2**), the $DORI_{int}$ and $DORI_{vol}$ were computed on truncated frozen snapshot geometries saturated with hydrogen atoms, placing emphasis on the targeted interaction. While not mandatory, such a truncation accelerates the DORI analysis without modifying the relevant contributions to the targeted domains (see Figure C.1 in Appendix C for a detailed description).

The π -conjugation pattern within the dithiophene unit of the photochromic torsional switch²⁵⁵ was analyzed using $DORI_{\pi}$, corresponding to the DORI function based on the π -density only. The π -density was constructed as the sum of the density stemming from π -orbitals. The relevant orbitals were chosen using the Adaptive Natural Density Partitioning (AdNDP) proposed by Boldyrev and co-workers,^{267,267,268} which is ideally suited for this purpose (see Appendix C for the detailed procedure).

Finally, the conformational spaces of the molecular rotor and the photochromic torsional switch are depicted using the sketch-map dimensionality reduction algorithm (see Appendix C).^{269–271}

5.3 Results and Discussion

5.3.1 Thieno-[2,3-b]-thiophene

The π -stacked arrangement of (hetero)aromatic cores is a distinct packing motif associated with pronounced optical and semiconducting properties.²⁷² Previously, DORI was shown to be a useful descriptor of the “electronic compactness” in quaterthiophene crystals⁸ and one-dimensional nanofibrils.^{135,136} In these materials, solubilizing side chains, hydrogen-bond and dispersion-driven aggregators were exploited to achieve tight packing, which was conveniently probed using the integration of the electron density within the DORI intermolecular domains (DORI_{int}) (*i.e.*, electronic compactness). The DORI-based “electronic compactness”⁸ largely correlated with charge mobility albeit offering distinct information.¹³⁶

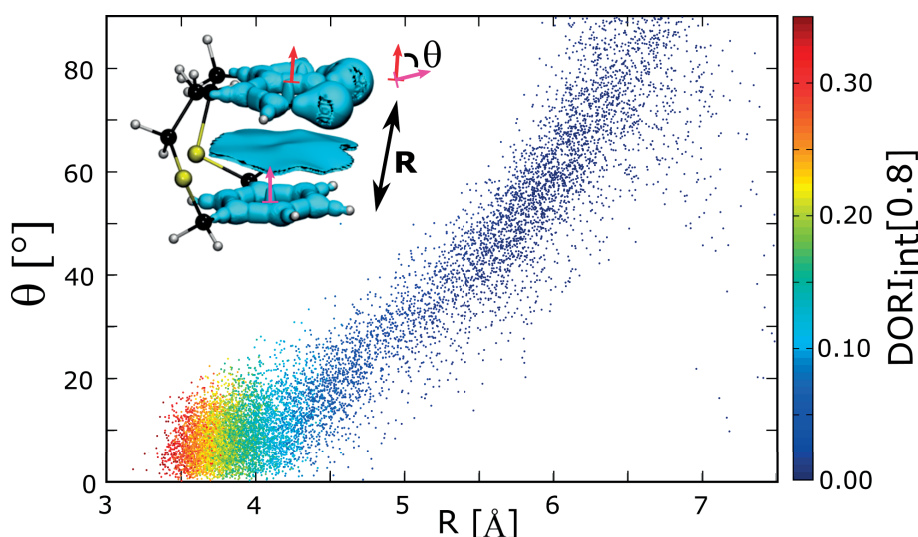


Figure 5.3 – Two-dimensional representation of the dithiacyclophane conformers color-coded with the integral of the electron density within the intramolecular DORI domain, $\text{DORI}_{int}[0.8]$. Conformers are extracted from the DFTB trajectory at 300K. The snapshots are described based on the distance between barycenters of the π -subsystems (R), and the angle between the two planes describing the π -systems (θ) mapped in the $[0,90]$ range. Conformers are color-coded using the integral of electron density in the intramolecular basin. DORI values are computed on electron densities relaxed at the PBE/6-31G* level on frozen DFTB3/3OB-UFF MD geometries.

Along the same line, the bridged asymmetrically polarized dithiacyclophane incorporating a thieno-[2,3-b]-thiophene (**1**),²⁵¹ possesses two low-lying $\pi - \pi$ stacked conformers.²⁷³ Thus, it is ideally suited for evaluating the advantages of DORI (over geometrical variables) in the anal-

ysis of packing fluctuations. Two geometrical collective variables characterize this “molecular packman”: the distance between the core and the angle between the normal to the plan (Figure 5.3). The relation between the geometrical criteria and the DORI_{int} value of 10'000 snapshots extracted from 54 independent NVT DFTB 300K molecular dynamic trajectories of 25ps (1.35ns in total) is visible in Figure 5.3. The “ π -stacked conformational region” corresponds to small R and θ values where the density overlap, *i.e.*, DORI_{int} , is significant (red, orange). Inversely, DORI_{int} vanishes when the molecule opens (*i.e.*, for large R and θ values) as the density overlap decrease towards zero (blue). Valuably, DORI encompasses all the structural and electronic features associated with the π -stacking pattern, into one single (DORI_{int}) value. For instance, it is clear from Figure 5.3 that the density overlap is more sensitive to R than to θ .

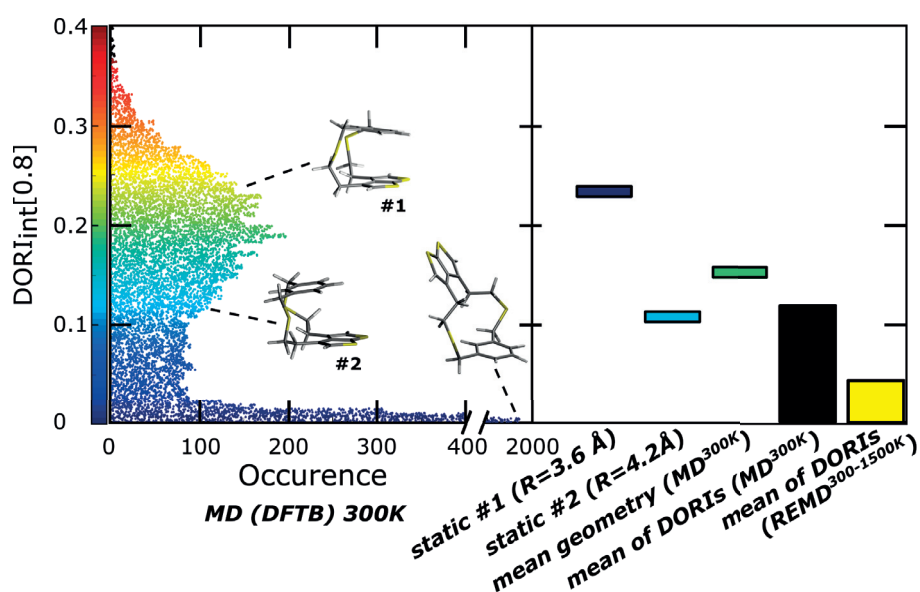


Figure 5.4 – Structure occurrence based on integral of the electron density ($\text{DORI}_{int}[0.8]$) within the intramolecular $\text{DORI}=0.8$ domain of the truncated dithiocyclophane, computed on the structures extracted from the MD (left). $\text{DORI}_{int}[0.8]$ of two optimized geometries (static # 1, # 2), the average MD geometry, and mean of DORIs from the standard MD at 300K, and from REMD@DFTB3³⁰⁰ K. DORI are computed on electron densities relaxed at the PBE/6-31G* level, on DFTB3/3OB-UFF (MD) geometries.

The comparison between the snapshots of the 300 K MD trajectories and the static gas phase geometry highlight the pronounced π -stacking fluctuations typical of this molecule. As mentioned earlier, two π -stacked minima having an interplane distance of 3.6 and 4.2 Å were found by static optimizations at the DFTB (or DFT).²⁵² These minima are within 2 kcal mol⁻¹ of one another (in favor of the former at the DFTB3/3OB level) and are associated with an electronic compactness, of 0.24 and 0.11 electrons, respectively (as measured by $\text{DORI}_{int}[0.8]$, see Figure 5.4). According to the DORI_{int} profile, the fluxional behavior of dithiacyclophane causes neither of the two static structures to be very representative of the molecule (see the time evolution of DORI_{int} in Figure C.3 in Appendix C). Within the timescale explored (1.35 ns), the molecule predominantly oscillates between these two conformations. Occasionally a third

region represented by an open conformation is also visible. The ensemble of DORI_{int} values shows a Gaussian distribution centered between the two closed conformations ($\text{DORI}_{int}=0.19$) but closer to the lower lying stacked minimum. A non-negligible contribution also arises from the open form ($\text{DORI}_{int} < 0.05$). For this flexible system, it was demonstrated that only a more efficient sampling technique, *e.g.*, REMD@DFTB3, permits a thorough exploration of the potential energy surface and reveals the presence of another dominant conformational “disarticulated” region.²⁵³ When the structures stemming from all three conformational regions are accounted for (*i.e.*, from REMD@DFTB3), the π -stacked conformations become less prevalent and the resulting mean DORI_{int} value is consequently much closer to zero. Taken together, this system clearly illustrates the importance of merging traditional quantum chemistry with accelerated sampling techniques prior to applying density-based descriptors that are capable of recognizing interaction patterns.

5.3.2 Molecular Rotor

Molecular rotors are one of the most illustrative class of fluxional systems. These molecules usually contain a fairly static component (the stator) and a more flexible and eventually switchable unit (the rotator). One of the computational and experimental challenge consists in understanding^{274,275} and controlling^{276,277} the molecular flexibility and the dynamic motion within the system such that more efficient rotors can be designed.²⁷⁸ One key factor influencing the rotor dynamics is the torsional potential, which is highly sensitive to the nature and strength of the non-covalent interactions occurring between the rotator and the stator.²⁷⁸ We illustrate this aspect by considering the dynamic motion of a recently synthesized molecular rotor (**2**), which features enthalpy driven conformational states stabilized by stator-rotor non-covalent interactions and more disordered (entropically favored) conformational states.²⁵⁴ In this system, the subtle interplay between the enthalpy and entropic factors was evaluated experimentally using variable-temperature NMR,²⁵⁴ and computationally by both a static²⁵⁴ and an REMD@DFTB²⁵⁹ picture. The structural motifs featuring the rotor and the stator throughout the fluxional process are schematically represented in Figure 5.5. Conveniently, the individual structural patterns have a specific DORI signature, contained in their associated non-covalent DORI domains. The characteristic volume of these domains, DORI_{vol} , can be monitored across the simulation such as to identify the dominant conformations. The histogram in Figure 5.5 displays the relative occurrence of each of these patterns sampled at 310 K (using REMD) in terms of DORI_{vol} . The figure reveals a clear dominance of the disordered conformations. The patterns range from a minority of very open-structures ($\text{DORI}_{vol} \sim 0\text{-}30 \text{ bohr}^3$) with nearly no overlap between the rotor and the two stators to the frequently visited and dominant entropically-driven structures that feature loose π - π or CH- π contacts visible for $\text{DORI}_{vol} < 70 \text{ bohr}^3$. The largest DORI_{vol} ($\text{DORI}_{vol} \sim 80\text{-}100 \text{ bohr}^3$) are associated with the reduced assortment of most compact enthalpy-driven conformations, which are characterized by substantial $\pi - \pi$ or CH- π contacts. The predominance of the entropic conformations is in line with experiment²⁵⁴ and with our alternative analysis of the REMD@DFTB results²⁵⁹ based on chemical shifts.

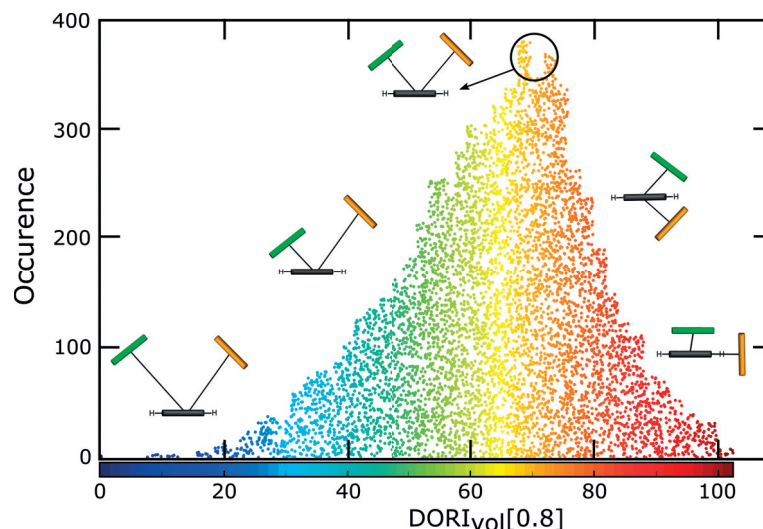


Figure 5.5 – Superimposed representations of the molecular rotor and its associated DORI[0.8] (blue) computed on the model system (a). Ranges of $\text{DORI}_{vol}[0.8]$ values for a given stator - rotator interaction (rotator considered for scheme colored in red) (b). Simultaneous visualization of the $\text{DORI}_{vol}[0.8]$ of the basins stemming from the two stator-rotator interactions, (I) and (II) (c). DORI are computed on electron densities relaxed at the PBE/6-31G* level on frozen DFTB3/3OB-UFF MD geometries.

Given the floppy nature of the systems discussed in this work, it is clear that many geometric parameters would be needed to fully characterize all of the different molecular fluctuations. DORI fingerprints, instead, provide a single value that captures the structural and electronic information of the different molecular conformers. In order to assess the extent to which this single parameter can characterize the complex structural landscape of fluxional molecules, it would be useful to juxtapose DORI with a data-driven low-dimensional representation of the structural landscape, rather than with few, more or less, arbitrarily selected collective variables. Fortunately, numerous algorithms have been developed for reducing the dimensionality of the representation of complex free-energy surfaces using linear (*e.g.*, principal component analysis^{279–281} and more elaborate non-linear projections (*e.g.*, ISOMAP,²⁸² Laplacian eigenmaps²⁸³, locally linear embedding²⁸⁴ or sketch-map^{269–271}). Here, the sketch-map technique specifically introduced by Ceriotti *et al.* was used to analyze atomistic data characterized by high dimensional thermal fluctuation.^{269,271}

Sketch-maps can be generated starting from any suitable high-dimensional representation of an atomistic configuration, and reduce this description to a low-dimensional (often, 2D) description in a way that preserves proximity between states: two points close on the sketch-maps share high structural resemblance in the high-dimensional space. Sketch-map has been successfully employed to describe the conformational space of proteins,^{271,285} extended solids,²⁸⁶ molecular and model clusters,^{270,286} to bias MD simulations,²⁷¹ or to classify (high-throughput) structural database.^{286,287} In this work, in order to avoid any bias in the construction of the low-dimensional representation, we do not select specific high-dimensional

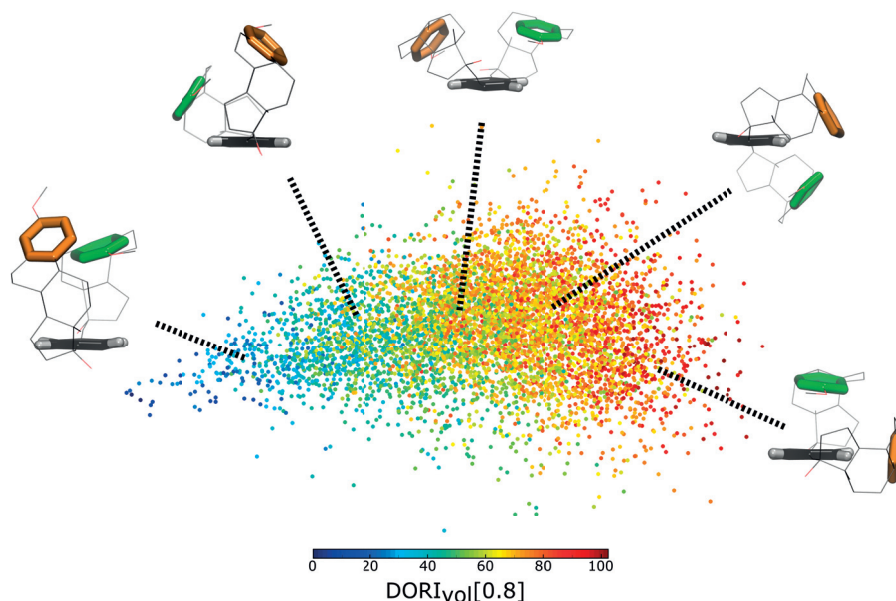


Figure 5.6 – Sketch-map representation of the molecular rotor, color-coded with the sum of the $\text{DORI}_{vol}[0.8]$ volumes stemming from interactions between the two stators and the rotator.

descriptors, but use a general measure of structural similarity²⁸⁶ that only relies on a combination of comparisons of local atomic environments. Owing to the highly flexible nature of the molecular rotor, **2**, no clear-cut free-energy basins emerge from the sketch-map analysis (see Figure 5.6). However, despite the breadth of the basin, structures with comparable interactions are projected close to each other in this representation. When the map is color-coded with $\text{DORI}_{vol}[0.8]$ values, it becomes clear that even without identifying separate structural clusters the sketch-map representation captures the essential features of the fluctuations of the rotor: a drift from high density overlap conformations (right, orange) to open forms of the rotor (left blue) is clearly visible. This observation demonstrates that sketch-map determines in an automatic, agnostic fashion structural features that are strongly connected with different levels of non-covalent bonding. Conversely, the excellent correlation between the main sketch-map variables and DORI prove that this density-based fingerprints can effectively capture the essential structural features of a highly fluxional system.

5.3.3 Photochromic Torsional Switch

In the previous examples, DORI was used to characterize only non-covalent interactions. Considering that the descriptor also capably distinguishes different bonding patterns, the final example uses DORI to gauge the extent of π -conjugation in a photochromic torsional switch (PTS) comprised of an azobenzene and a bithiophene subunit.²⁵⁵ In this PTS, a strong rearrangement upon photoisomerization modulates the π -conjugation within the bithiophene subunit.²⁵⁵ In short, the Z azobenzene configuration allows the bithiophene subunit to achieve a quasi-planar anti-conformation, whereas a twisted bithiophene dominates the E

azobenzene configuration. This torsion-planarization, which directly impacts the extent of π -conjugation, was probed experimentally by measuring the absorption spectra.²⁵⁵ Here, the conjugation strength is monitored by the $DORI_{\pi int}$ of the inter-thiophene bond (see Figure 5.7 and computational details).

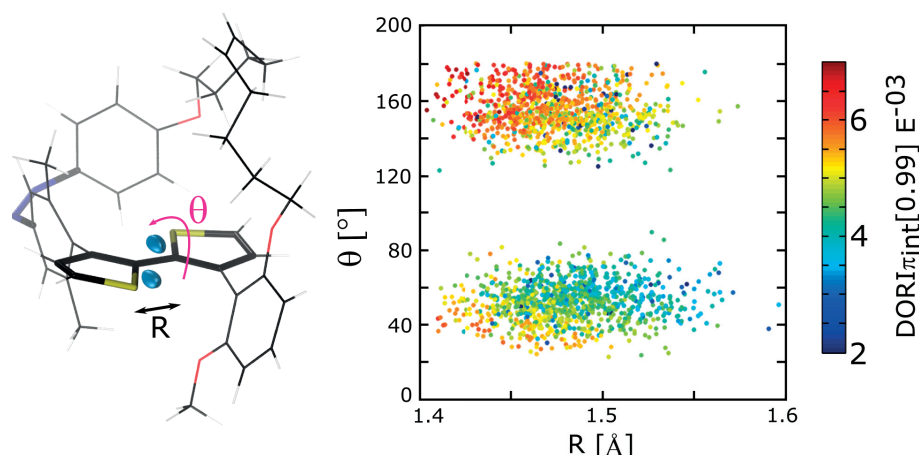


Figure 5.7 – Representations of the photochromic torsional switch and its associated $DORI_{\pi}[0.9]$ (in blue) for the inter-thiophene bond (left). Correlation of the $DORI_{\pi int}[0.99]$ with the inter-thiophene bond distance (R) and the inter-thiophene \angle SCCS dihedral angle (θ), mapped in the $[0,180]$ range. DORI are computed on electron densities relaxed at the PBE/6-31G(d) level on frozen DFTB3 / 3OB-UFF geometries from REMD.

In Figure 5.8, the sketch-map, which clearly separates the E from the Z-azobenzene configurations without using arbitrarily selecting collective variables, is enriched by a color coding based on the $DORI_{\pi int}$ values. The rather weak π -conjugation (coinciding with low $DORI_{\pi int}$ values, light blue-green) is distinctive of the E-azobenzene domain, which contrasts with the dominant red color (larger π -conjugation) of the Z-azobenzene conformational region. While this difference attests to the fact that this switch efficiently modulates the extent of π -conjugation within the bithiophene unit, the electronic information encoded in $DORI_{\pi int}$ is more comprehensive than the geometrical variables. As evident from Figure 5.7 (right), neither the \angle SCCS dihedral angle (Θ), nor the inter-thiophene carbon-carbon bond (R) completely describes the extent of delocalization. Both the Z and E configurations are affected by thermal fluctuations meaning that for a given dihedral angle (Θ) characteristic of the planar dithiophene (*i.e.*, Z-azobenzene configuration, inter-thiophene $\Theta \in [120, 180]$), the π -conjugation (*i.e.*, $DORI_{\pi int}$) decreases as the bond length increases. Similarly, for a fixed C-C bond length, the $DORI_{\pi int}$ weakens as the two thiophenes twist out of planarity. Hence, $DORI_{\pi int}$ decreases when the π -delocalization is reduced either by bond lengthening and/or deplanarization of the dithiophene. As expected, the final picture given by $DORI_{\pi int}$ for the PTS is an overall higher π -overlap for the Z-configuration, which correspond to experimental findings.²⁵⁵

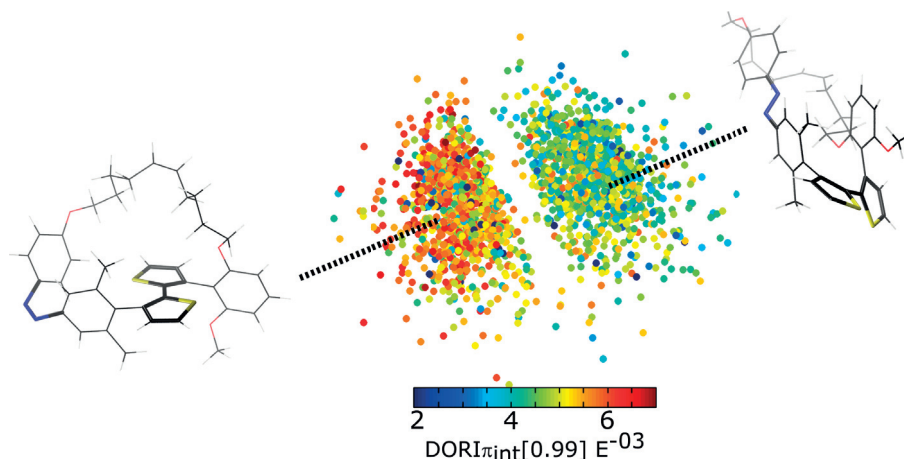


Figure 5.8 – Sketch-map representation of the photochromic torsional switch **3**, forming two distinct zones corresponding to the Z- and E-azobenzene configuration (left and right respectively). The map is color-coded with the electron density integral stemming from the $\text{DORI}\pi_{\text{int}}[0.99]$ basins of the dithiophene bridging bond (a), and with the free energy computed from the molecular dynamics occurrences (b).

5.4 Conclusion

In conclusion, we have shown that DORI provides unique insight into studies involving highly fluxional molecular systems. Using snapshots extracted from molecular dynamic simulations that exploited the efficiency of REMD@DFTB3, characteristic DORI-based electronic signatures were examined in tandem with a powerful data-driven low-dimensional representation of the structural landscapes. This procedure resulted in a picture that captured fluctuations arising from changes in bonding patterns and non-covalent interactions more clearly than with arbitrarily chosen geometrical collective variables. Thus, representations of complex conformational spaces and electronic processes can be described with no loss of structural information by using a single DORI-based variable.

The combination of DORI descriptors with sketch-map, a non-linear dimensionality reduction technique that strives to obtain a similarly general simplified description based on geometric parameters, cross-validates the two approaches. The strong correlation between the location of a configuration on a sketch-map and its corresponding DORI value (encoded with color) shows that DORI can distinguish structurally different conformations, and, vice versa, that sketch-map coordinates identify structural variables that are associated with marked changes in both covalent and non-covalent bonding. While, this work has focused on three illustrative systems characterized by specific fluctuating (non-)covalent interactions, similar analyses could be highly beneficial to better comprehend the massively different behavior types seen in chemistry and material sciences (*e.g.*, catalysis, supramolecular chemistry, amphidynamic crystals).

6 The Interplay between Covalent Bonding Patterns and Non-Covalent Interactions in Biscarbonyl[14] Annulene under Pressure

This chapter is based on following publication:

The Interplay between Covalent bonding Patterns and Non-Covalent Interactions in Biscarbonyl[14] Annulene under Pressure. Laurent Vannay, Benjamin Meyer, Benoit Guillot and Clémence Corminboeuf, *in preparation*

L. Vannay did the DORI analysis, B. Meyer did the literature research, B. Guillot refined the experimental electron densities.

6.1 Introduction

The behavior of matter under high pressure is historically the realm of geoscientists (*e.g.*, geodynamics^{288–290} and ice stability²⁹¹) and astrophysicists,²⁹² since most of the Earth's matter and extra-terrestrial environment are exposed to extreme conditions. In the laboratory, solid state scientists exploit pressure to enable (new) phase transitions,^{293,294} to trigger chemical reactions as well as^{295,296} conformational and structural modifications,²⁹⁷ or to explore polymorphisms.^{298,299} Pressure considerably contributes to a better understanding of many condensed-phase chemical phenomena,^{300–303} and assists in the development of superconductors and to generate structural phase transitions for metals^{304–306} and non-metallic elements.^{307,308} These significant modifications on the crystal environment induce unusual covalent patterns^{309–315} and dramatically alter electronic properties.^{316,317} Countless high pressure applications are in the spotlight, such as superhard materials^{318–320} (*e.g.*, for industrial applications in cutting or polishing tools), high energy density materials (HEDMs)^{321,322} (*e.g.*, for the synthesis of propellants and explosives) or molecular systems for hydrogen storage.^{323–325}

High pressure investigations of organic or organometallic molecular crystals are more rare, but are fundamentally important^{326,327} since they provide insights on the distortion of crystal packing,^{328–330} the switching of molecular conformations,^{331,332} or the mechanism of phase transitions, to cite a few.³³³ Such investigations are constantly employed in metal-

Chapter 6. The Interplay between Covalent Bonding Patterns and Non-Covalent Interactions in Biscarbonyl[14] Annulene under Pressure

organic frameworks,^{334–336} pressure-induced photomagnets,³³⁷ piezochromic switches,³³⁸ photovoltaic hybrid perovskites,^{339,340} and organic molecular crystals^{328–333,341,342} including pharmaceutical compounds,^{343,344} and amino acids.^{345–347}

Studies on molecular crystals reveal the striking effect of intermolecular interactions at high pressure, where they govern not only the molecular packing in crystals, but also the resulting electronic and optical properties.³⁴⁸ Non-covalent interactions, thus, directly impact the covalent region by changing the conformation and reactivity of chemical^{349,350} or biomolecular compounds.^{328,331,332} This peculiar interplay between covalent bonding and non-covalent interactions at high pressure is typically investigated through variable pressure experiments,^{351,352} which are characterized by their geometrical parameters (*e.g.*, interatomic distances, torsion and dihedral angles) and their stiffness exploiting diffraction techniques and vibrational spectroscopy, respectively.^{322,328,330–332,342,349,350,353–357} However, investigating the changes in the electronic structure itself, rather than its influence on geometry or spectroscopy, represent a more straightforward and sensitive way to analyze molecular interaction at high pressure.

Computational chemistry offers several tools to examine electronic structures, although the give-and-take type behavior between covalent bonding and non-covalent interactions are generally overlooked because of their relatively mild influence in the gas phase. One notable exception are the interactions of one or more aromatic rings with the surrounding environment, including π -stacking, cation- π , anion- π , XH- π or lone pair- π , playing a prominent role in many areas of chemistry,^{358,359} molecular biology,^{359,360} and material science.³⁶¹ For such systems, Wheeler and coworkers demonstrated that non-covalent interactions between substituted aromatic rings could modify the distribution of π -electron density within aromatic rings.^{22,362–365} Similarly, H-bonding interactions were shown to impact the aromatic character of π -conjugated heterocycles through π -electron polarization effects.³⁶⁶ The H-bond strength could be controlled by resonance-mediated cooperative interactions (anti)aromatic π -delocalization.^{367,368} Such mutual reinforcement concept helped to rationalize the stabilization of reactive oxyanion intermediates in enzyme catalysis³⁶⁹ and the self-assembling of 4-pyridone chains.³⁷⁰

Halogen bonds are attractive interactions widely exploited in crystal engineering,^{371–375} solid-state synthesis for material science^{376–384} and organocatalysis^{385–387} applications). The nature of the covalent bond between the donor site and the halogen directly influences the strength of its non-covalent interactions,^{388–391} which gives access to a wide range of non-covalent interaction energies^{392–402} by changing the magnitude of the σ -hole.³⁸⁸

The aforementioned applications illustrate several investigations on electronic structures changes due to the interplay between covalent bonding and non-covalent interactions. However, the employed gas phase systems differ from actual solid state crystals under high pressure, where the synergy between chemical interactions become prominent. One way to accurately consider the environment effects is to analyze experimental electron densities, obtained

from high resolution X-ray diffraction data.^{403–407} Pioneering work has indeed been conducted with the aim of detecting modifications to the electronic structure of molecules under compression.^{353,408–410}

Even if the determination of accurate molecular crystal electron density mapping is now possible, the analysis of the electron density alone struggles to properly describe chemical bonding and intermolecular interactions at both ambient and high pressures. The experimental data is, thus, preferably analyzed through quantum chemical topology, and/or molecular scalar fields. The topology analysis of the electron density, introduced by the Quantum Theory of Atoms in Molecules (QTAIM),²⁴ has nearly systematically been adopted for the past two decades⁴¹¹ but leads to cryptic real-space representations, in particular for non-directional interactions such as van der Waals.⁴ The electron Localization Function (ELF)^{5,51} and the Electron Localizability Indicator (ELI)⁹⁹ are more intuitive for visualizing atomic and molecular interactions and are applicable for experimental electron densities,^{85,86,412–414} yet they remain strongly dependent (need molecular orbital computations) on the X-ray constrained wavefunction method^{81,415} and its developments.^{416–418} Thus, such scalar fields are not suitable for analyzing non directional intermolecular interactions (van der Waals, cation- π , *etc.*),⁴ which are better revealed by alternative functions such as the Non-Covalent Interaction index (NCI)^{9,10,419–421}

Only one scalar field is, to date, able to simultaneously capture covalent bonding and non-covalent interactions in an intuitive manner using only the electron density, and its derivatives: the Density Overlap Region Indicator (DORI):⁸

$$DORI = \frac{\theta(\mathbf{r})}{1 + \theta(\mathbf{r})} \quad (6.1)$$

where

$$\theta(\mathbf{r}) = \frac{\left(\nabla \left(\frac{\nabla \rho(\mathbf{r})}{\rho(\mathbf{r})} \right)^2 \right)^2}{\left(\frac{\nabla \rho(\mathbf{r})}{\rho(\mathbf{r})} \right)^6} \quad (6.2)$$

DORI was recently introduced by De Silva and Corminboeuf as a modification of the Single Exponential Decay Detector (SEDD),¹²⁸ and captures regions of space corresponding to electron density overlaps between atomic shells, atoms or molecules. It has been successfully exploited by our group to construct local hybrid exchange-correlation functionals,^{130,134} to examine at electronic compactness in nanowires,¹³⁵ to investigate excited states^{12,207}, and to analyze fluxional molecular systems. However, applications of DORI, or any other visual scalar field, on molecules at high pressure remains *terra incognita*.

Our investigation focuses on a double bridge annulene, *syn*-1,6:8,13-biscarbonyl[14]annulene (BCA), one of the very small number of system for which accurate experimental electron

Chapter 6. The Interplay between Covalent Bonding Patterns and Non-Covalent Interactions in Biscarbonyl[14] Annulene under Pressure

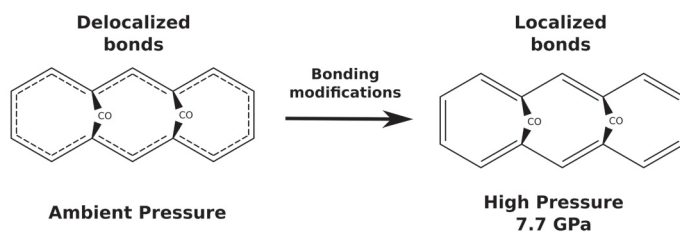


Figure 6.1 – Conceptual Lewis representation of the syn-1,6:8,13-biscarbonyl[14] annulene at ambient and at high pressure.

density at ambient⁴²² and high pressure⁴²³ are available. Macchi and co-workers observed high pressure modifications of the annulene, where the roughly C_{2v} molecular symmetry displayed at ambient pressure⁴²² evolves towards an asymmetric structure with considerably weakened electronic delocalization (see Figure 6.1). Another survey⁴²⁴ found that upon an increase in pressure the double bonds of the annulene ring become more localized, and adopt one of the two resonant configurations of the ideal aromatic system. Non-covalent interactions in the crystal environment and their impact on the covalent pattern were, however, not specifically considered in these investigations.

The present work investigates (i) pressure-induced modifications on electronic structures of molecular crystals and (ii) the interplay between covalent bonding and non-covalent interactions in high pressure conditions. The utility of the DORI scalar field is highlighted by, for the first time, rationalizing the bonding modifications that occur in BCA at high pressure. We show the unique ability of DORI to simultaneously capture covalent and non-covalent region is critical for understanding high pressure effects, that stem from the interplay between intra and intermolecular crystal interactions. In addition, this work represents the first application of DORI to experimental charge densities, providing a blueprint for electronic analysis of organic molecular crystals under pressure.

6.2 Computational Details

Theoretical electron densities were computed at the ω B97X and PBE0/6-311G(d,p) level^{181,425} on experimental X-ray geometries. Experimental electron densities and geometries were generated using ultra high resolution measurements from Destro *et al.* (0.44 Å) at ambient pressure,⁴²² and from Casati *et al.* (0.50 Å) at high pressure (7.7 GPa),⁴²³ found in the Cambridge Crystallographic Data Centre (CCDC) under deposition numbers 1022018 and 1438922, respectively. Those very high resolution X-ray diffraction data enabled us to exploit a full Hansen and Coppens multipolar model⁴²⁶ that consider the perturbations of the electron density due to chemical bonds and intermolecular interactions.

DORI was computed numerically using a local script (available on request) using electron densities stored on 20 points/Bohr grid meshes. Visual representations were generated from Visual Molecular Dynamics (VMD),⁴²⁷ and Paraview⁴²⁸ software, while integration of electron

density inside DORI basins was achieved using DGrid-5.0.⁴²⁹

As BCA is non planar, the DORI in-plane is obtained by taking three average planes passing through four atoms in each cycle. All three-dimensional representations exploit a truncated supercell which completely encompass one molecule, together with few atoms of all nearest neighbors to ensure that all intra- and intermolecular interactions are captured in a single snapshot. A minimal picture encompassing all possible interactions in the crystal might be formally obtained using the unit cell only. However, the unit cell representation cuts through molecules and interactions in an extended 3D environment, leading to rather cryptic pictures. The relevant DORI isovalue for intramolecular application was selected such that basins from C-C bond patterns are dissociated from atomic basins at both ambient and high pressure. The same isovalue was chosen at both pressure to ensure valid comparisons.

DORI quantitative analysis is performed by integrating the electron density within the covalent patterns defined by DORI isosurfaces:

$$DORI_{int}(V_{iso}) = \int_{V_{iso}} \rho(\mathbf{r}) d\mathbf{r} \quad (6.3)$$

6.3 Results and Discussions

The delocalized electronic structure of biscarbonyl[14] annulene (BCA) is perturbed by several factors. At ambient conditions, the BCA backbone planarity is disrupted by the presence of the two carbonyl bridges.⁴³⁰ This effect remains visible in the crystal, and is clearly captured by the in-plane DORI representation (see Figure 6.2) where carbons cross the DORI planes at different heights: eight carbons atoms show core regions (in red), while the rest lie below the plane, and display their valence-core separation region (in green). The overall BCA symmetry remains C_{2v} in the crystal at ambient pressure which corresponds to the symmetry the molecule in the gas phase.⁴²² Thus, the crystal perturbation on covalent region remains weak at ambient pressure.

At high pressure, the BCA electron delocalization is more perturbed. Casati *et al.* noted the asymmetry of the molecular geometry, visible in the 2D DORI representation. The gas phase C_{2v} symmetry is replaced by a distorted annulene skeleton that displays signs of compression (Figure 6.2). This compression is also visible in the intra ring (non-covalent) charge density clashes (blue ovoid shapes near ring centers) which enlarge because of larger intra-ring density overlaps. An electronic overlap develops between the carbons forming the pillars of the ketone bridge which hints a possible evolution into formal bonds at higher pressures.

Since BCA is non planar, 3D representations are required to investigate the bonding pattern. DORI three-dimensional isosurfaces display that each of the 14 C-C bonds have similar patterns at ambient pressure (see Figure 6.2), a sign of a partial electron delocalization over the

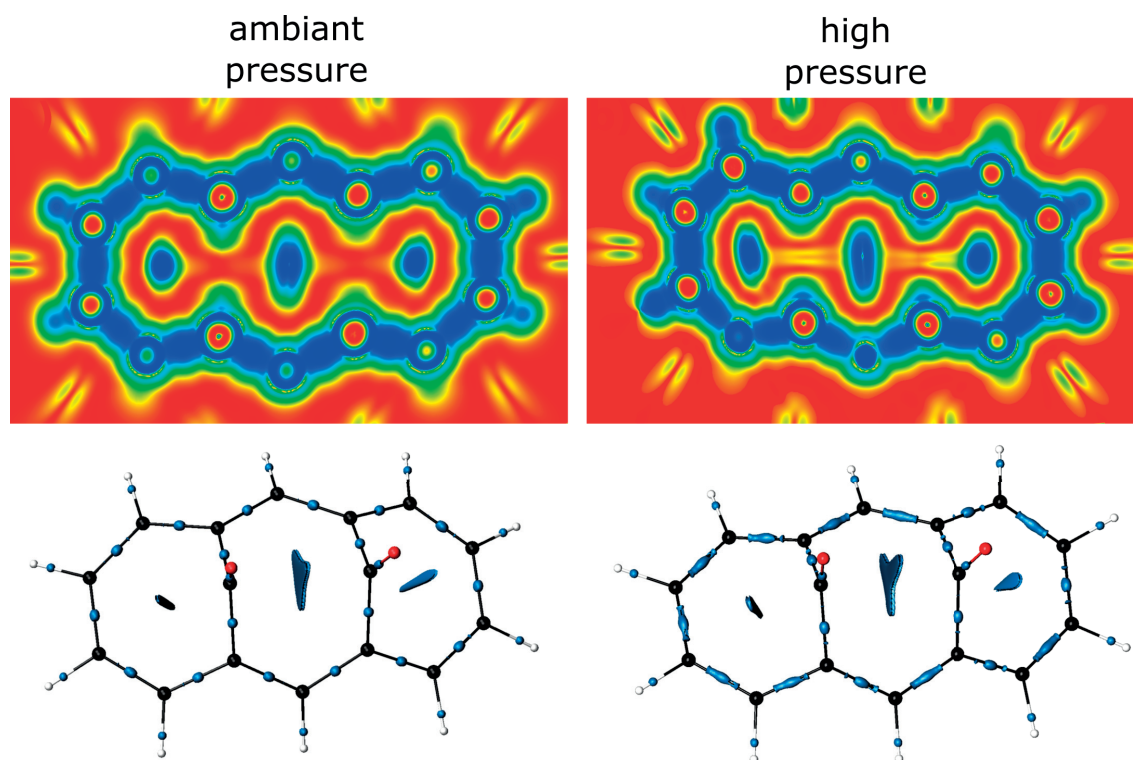


Figure 6.2 – Three superimposed two-dimensional DORI maps of the biscarbonyl [14] annulene (top, color-code from DORI=0 (red) to DORI=1 (blue)). DORI = 0.999 isosurfaces (blue) of the biscarbonyl [14] annulene (bottom). Both representations are given for ambient (left) and high pressure (7.7GPa, right).

annulene ring. Conversely, the high pressure clearly perturbs the electron delocalization and modifies the DORI patterns (see 6.2). This change in electronic structure can be considered as a first step that precedes the addition reactions that lead to polymerization. Similar reaction mechanisms were recently exploited to form polymeric ethylene,⁴³¹ triptycene,⁴³² as well as sp^3 carbon nanothread from benzene molecules^{433,434} through $[4\pi + 2\pi]$ cycloaddition reactions followed by a zipper cascade. Thus, it seems reasonable to imagine that biscarbonyl [14] annulene could also polymerize at higher pressure.

As noted by Casati *et al.*,⁴²³ charge density accumulation in specific bonds of the annulene ring attest the asymmetry of the biscarbonyl[14] annulene molecule at high pressure. The electron density integrals of the DORI covalent patterns represented in Figure 6.3 support that the biscarbonyl[14] annulene nearly has C_{2v} symmetry under ambient conditions (see Figure 6.3 a). At high pressure, this symmetry is broken and the DORI integrals are no longer similar. The electron density integrals within the annulene covalent patterns reveal a bond type alternation (single and double character) upon an increase in pressure that disrupts the electron delocalization in the molecule.

Similar pressure effects on electronic structures associated with a destabilization of the π

molecular orbitals, *i.e.*, a reduction of electron delocalization, were detected through two-photon spectroscopy for pyridine⁴³⁵ and s-triazine⁴³⁶ molecules in the crystal phase. The observed modifications on the π -conjugation covalent pattern were ascribed to the pressure driven enforcement of non-covalent interactions. In order to assess if, and to what extent, pressure induced electronic effects stemming from the crystal environment impact the electron delocalization in biscarbonyl[14] annulene, we compared integrals within DORI basins determined from the experimental electron density with those of an isolated molecule computed at DFT level using the same geometry. The theoretical computations, likewise, demonstrate that the electronic structure of one six-membered ring (C_1 - C_6) is more localized than the other (C_8 - C_{13} , see Figure 6.3 b,c). The integrals arising from the high pressure experimental electron density are numerically very different, while they remain similar at ambient pressure (see Figure 6.3 b,c), which indicates that DORI intrinsically captures the electronic constraints imposed by the crystal environment at high pressure. This effect is caused by the compression

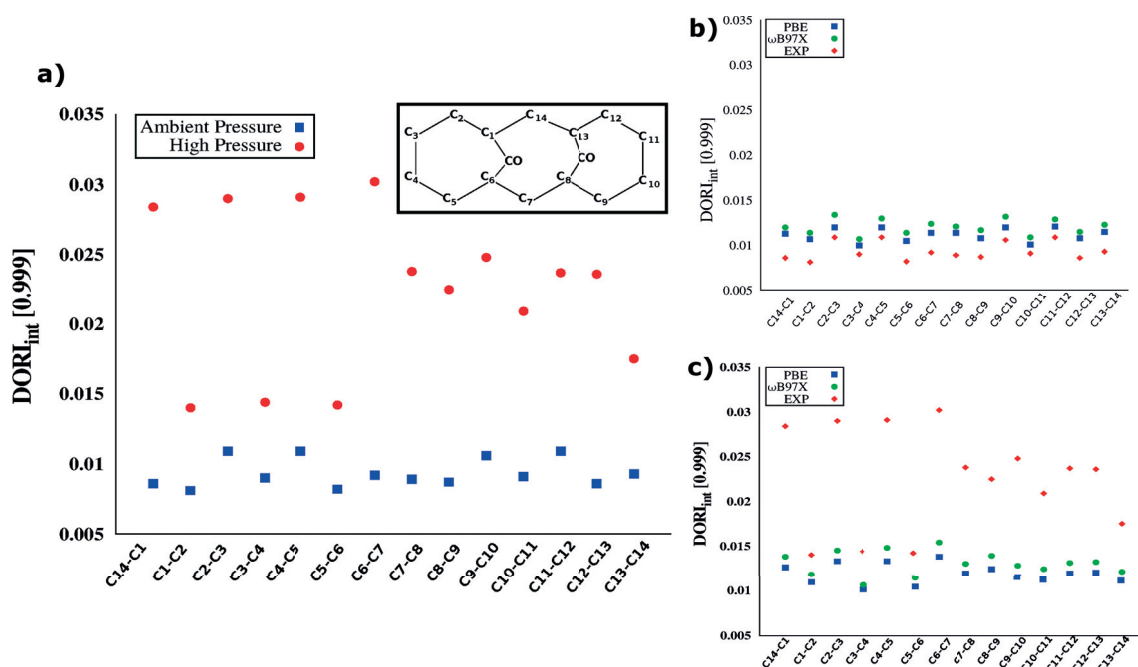


Figure 6.3 – Integral of the experimental electron density [a.u.] inside C-C bonding basin of the BCA molecule at ambient (blue) and high pressure (red), enclosed in the DORI=0.999 isosurfaces.

of the electronic structure at high pressure and occurs through the non-covalent interactions between molecules in the crystal. Indeed, the pressure produces an inhomogeneous contraction/expansion of the C-C bonds located on the annulene skeleton. The origin of the BCA asymmetrical behavior in the covalent domain at high pressure has never been clearly discussed, until now.

Intermolecular contacts generally mildly impact covalent bonding, and are thus often neglected when examining bonding patterns. At high pressure however, intermolecular interac-

Chapter 6. The Interplay between Covalent Bonding Patterns and Non-Covalent Interactions in Biscarbonyl[14] Annulene under Pressure

tions become crucial to rationalize covalent behavior.⁴³⁷ Applying pressure, the non-covalent patterns naturally deliver a response to this external stimulus. The strength and the directionality of the intermolecular interactions were proposed to rationalize the extent and the (iso-)anisotropy of the covalent pattern variations.³⁵⁶ Until now, pressure induced relations between covalent bonding and non-covalent interactions were only characterized by geometrical parameters,^{322,328,331,355,438} without exploiting experimental electron densities.

At ambient pressure, DORI captures a rich network of interactions around a single BCA molecule, which might be regrouped under CH–O interactions, pseudo $\pi - \pi$ stacks and hydrogen contacts. The seven non-redundant CH–O interactions present in the BCA crystal⁴²² are characterized by isolated discotic DORI basins, typical of hydrogen bonding.⁸ It was recently pointed out^{4,439} that non-directional interactions represent a significant portion of non-covalent interactions. This is nicely demonstrated by the many van der Waals basins encompass each of the BCA molecules at ambient and high pressure (see blue basins in Figure 6.4). Interestingly, while these omnidirectional interactions can be missed within the traditional QTAIM framework, they play a major role in the interacting patterns captured by DORI.

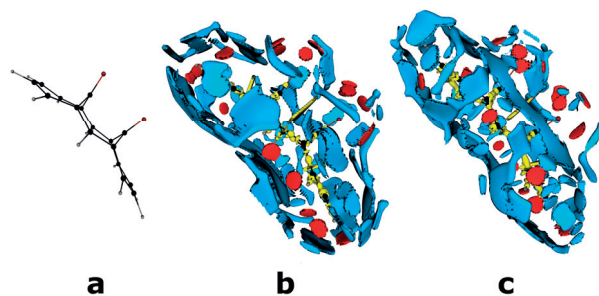


Figure 6.4 – BCA geometry (a), DORI=0.995 isosurfaces displaying the network of non-covalent interactions of one single BCA molecule in crystal environment at ambient (b) and high pressure (c). Van der Waals interactions colored in blue, CH–O in red, and intramolecular in yellow.

Under high pressure, the size of all basins stemming from van der Waals interaction grows around the molecule, as a logical consequence of the increase of density overlap between molecules forced closer to one another by an external stimulus (see Figure 6.4). This basin broadening takes its origin from the larger elasticity of van der Waals interactions, which are typically more compressible than directional interactions.⁴³⁷ Because of their higher elastic stiffness, directional non-covalent interactions like hydrogen bonds are significantly less compressible. Since the BCA crystal is dominated by van der Waals interactions, the net result is an overall compression of the interacting region around the annulene molecule (see Figure 6.4).

Directional interactions are fundamental for interpreting the anisotropy of lattice strain acting

on molecular crystals under compression.^{440,441} The observations of pressure induced covalent modifications due to pressure promoted formation of CH–O non-covalent interactions contributed in shedding new light on the exceptional elasticity of cellulose fibers,^{328,331} and on the stability of tetrahydrofuran at high pressure.

From the DORI viewpoint on the BCA crystal, CH–O non-covalent interactions are the key to rationalize the BCA covalent pattern. Indeed, as pressure is applied, several CH–O basin slide from the standard H–O to an unconventional $\begin{smallmatrix} \text{C} \\ | \\ \text{H} \end{smallmatrix} - \text{O}$, where the interacting basin now point to the carbon-hydrogen bond. In particular, two of these interactions occur out of the pseudo-plane of the BCA molecule, and pushes the neighboring carbon atom in opposite directions (see Figure 6.5). These interactions break the planarity in the covalent region of the BCA, which reduces electron delocalization. This interplay is captured with DORI, which shows both the covalent patterns and the inter-molecular interactions that are directly influenced.

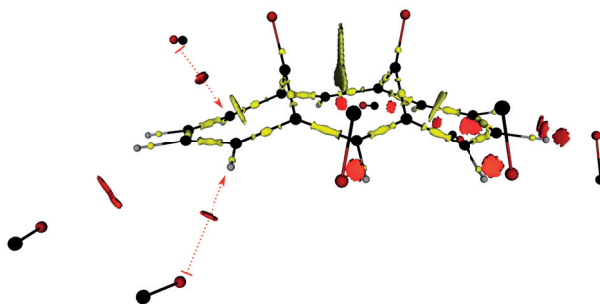


Figure 6.5 – DORI=0.999 isosurfaces capturing the CH–O interactions of one single BCA molecule in crystal environment at and high pressure. Red arrow pinpointing out-of-plane interactions.

At high pressure, the role of the crystal anisotropy becomes prominent in rationalizing covalent bonding patterns: the specific regions where non-covalent interactions significantly impact their covalent counterparts depend on the crystal packing. The crystal anisotropy rationalizes the observed changes in DORI bonding patterns occurring on one side of the BCA only: the specific out of plane $\begin{smallmatrix} \text{C} \\ | \\ \text{H} \end{smallmatrix} - \text{O}$ interactions only apply to the C₁-C₆ ring due to the crystal packing. Hence, at high pressure, the crystal anisotropy transfers into the covalent domain through the non-covalent interactions, breaking the C_{2v} symmetry of the BCA at ambient pressure.

Overall, it is very promising to see that DORI rationalizes this peculiar interplay between covalent bonding and non-covalent interactions at high pressure, exploiting actual experimental electron densities.

6.4 Conclusions

This work described the first application of DORI to high quality experimental densities of an organic crystal measured at ambient and high pressure. The simple visual DORI analysis could capture key effects induced by the high pressure conditions on the BCA crystal, including (i) peculiar covalent bonding behavior, (ii) the interplay between covalent bonding and non-covalent interactions and (iii) the transfer of crystal anisotropy into covalent regions, with all three aspects being entangled.

While non-covalent minimally influence the covalent region at ambient pressure, a strong interplay is observed at high pressure. In particular, non-covalent contacts disrupt BCA ring planarity through peculiar $\overset{\text{C}}{\text{H}} - \text{O}$ interactions. These crystal effects were shown to not only influence the geometry, but also to impact the actual electron density of the covalent region, an effect that could be captured by the density-dependent DORI.

The crystal anisotropy also becomes decisive in rationalizing the covalent patterns at high pressure. The disruption of electron delocalization occurring only on one aromatic ring of the BCA molecule stem from the different crystal environments of the otherwise symmetrical BCA rings. Hence, crystal anisotropy can change the actual symmetry of a molecule inside the crystal, allowing for selectively modifying *e.g.*, the reactivity of a given part of a molecule.

This work delivers a blueprint for the electronic analysis of organic molecular crystals under pressure using DORI and its unique ability to simultaneously capture covalent bonding and non-covalent interactions.

6.5 Proteins Exploit Non-covalent - Covalent Interplays

This work is done in collaboration with Prof. Dr. F. P. Seebeck who crystallized and analyzed the protein structures, and Dr. B. Meyer who computed electron densities and Hirshfeld charges. L. Vannay performed the DORI analysis.

Protein active sites are examples in which specific packing constraints influence the chemical behavior of functional groups. For example, the biosynthesis of ergothioneine, a potential entry molecule used for synthesizing antituberculosis drugs, begins by trimethylation of an α -amino group of histidine that is catalyzed by the ergothioneine biosynthetic methyltransferase EgtD. Recently, Seebeck and coworkers characterized the X-ray structure of EgtD at different stages of the trimethylation process.^{442,443} Notably, they identified each of the intermediary structures for the final methylation step, corresponding to EgtD complexed with dimethylhistidine (DMH), dimethylhistidine with S-adenosylmethionine (DMH_SAH), and trimethylhistidine (TMH), the final product. In order to discover which protein-ligand interactions favor this methylation reaction, we used DORI to analyze the DMH, DMH_SAH and TMH X-ray structures on electron densities computed at the PBE0/TZP level. For all complexes, DORI reveals a universal intermolecular N-CH₃-O interaction between the methylated

histidine and the Gly161 residue of methyltransferase EgtD (Figure 6.6). The reddish color at the center of the DORI isosurface suggests a slightly attractive directional interaction,⁸ with an electrostatic contribution that impacts the reactive properties of the methylated nitrogen. Indeed, the Hirshfeld charge analysis confirms that the N-CH₃-O interaction causes a slight reduction of the positive charge for the nitrogen (see Figure 6.6), which assists the methylation process. Thus, simply visualizing DORI, along with the $sgn(\lambda_2)\rho(r)$ color code, reveals specific protein-ligand interactions that influence the methylation reaction.

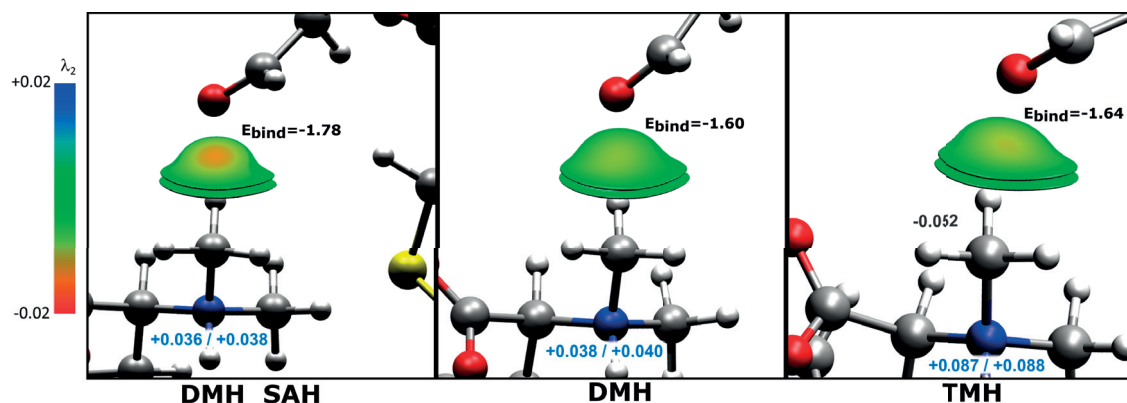


Figure 6.6 – DORI=0.9 isosurfaces color-coded with $sgn(\lambda_2)\rho(r)$ ranging from -0.02 au (red, attractive) to +0.02 au (blue, repulsive). The electron densities and binding energies (E_{bind} [kcal/mol]) between the glycine residue and the dimethylhistidine (for DMH and DMH_SAH), and the trimethylhistidine (TMH) were computed at the PBE0-dDsC/TZP level. Iterative Hirshfeld charges on nitrogen are depicted in the presence (left) or absence (right) of the Gly161 residue.

6.6 DORI Assessing Electron Densities

Ultra-high resolution experimental electron densities are now available for several crystals,^{407,444–448} which could serve as benchmarks for DFT and other computational methods. This includes methods that do not directly provide energies, such as fragment based approaches (proatomic densities, density embedding, *etc.*) Experimental benchmarks are particularly appealing for use as electron density parameters in developing new density functionals. As recently noted by Perdew *and co.*,⁴⁴⁹ fitting functionals without accounting for properties that depends strongly on the electron density (*e.g.*, dipole moments, charge distributions, ...) might lead to worsen the description of the electron density, especially in highly parametrized functionals such as the Minnesota family (M05, M06, ...).⁴⁴⁹ Here, DORI could be used to analyze the electron density differences stemming from different approaches. Comparison between DORIs specifically reveal variations in regions where chemical interactions occur. As such, DORI is positioned to become a formidable tool for assessing and improving fragment approaches and DFT methodologies. Here, we compare DORI computed on experimental electron densities with several theoretical methods ranging from crude proatomic densities to more sophisticated density functional approximations,

Chapter 6. The Interplay between Covalent Bonding Patterns and Non-Covalent Interactions in Biscarbonyl[14] Annulene under Pressure

computed on gas phase molecules at the ambient pressure BCA X-ray structure.

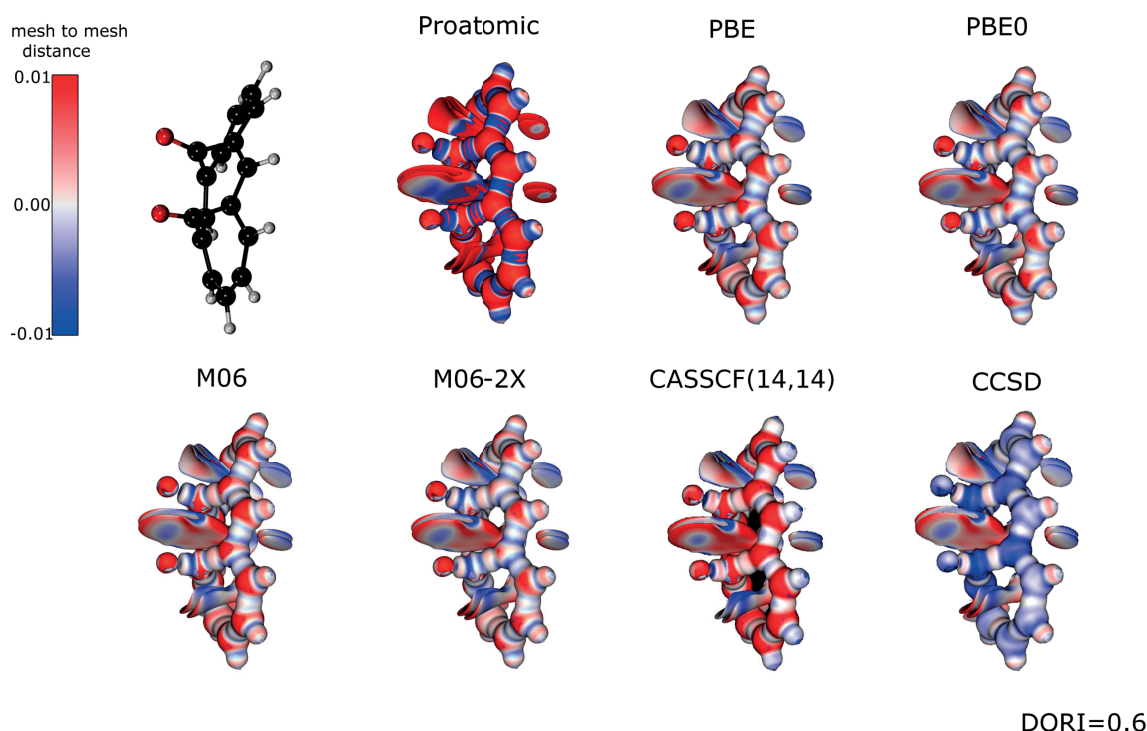


Figure 6.7 – Mesh to mesh Euclidian distances [au] between DORI=0.6 isosurfaces of the BCA using DORI computed on the experimental electron density as a reference.

Cheap proatomic densities are often used to qualitatively describe non-covalent interactions in large systems. For covalent regimes, however, they provide rather poor descriptions that indicate large deviations from experimental electron densities (Figure 6.7). Post-HF and DFT methods, on the other hand, provide accurate descriptions relative to proatomics. However, *ab initio* methods show discrepancies that persist across several DORI isovalues and different test molecules (*i.e.*, coumarin dye, and tetrafluoroterephthalonitrile, see Appendix D for the detailed figures). This suggests systematic differences between experimental and computed densities, the origin of which is currently under investigation. For the BCA, the inclusion of static correlation through CASSCF yields DORI[0.6] isosurfaces with marked differences close to atomic positions (red surfaces in Figure 6.7). Inclusion of dynamical correlation through CCSD result in non-uniform descriptions with the atomic centres located in the annulene staying in close agreement with experimental DORI, while the bridging atoms appear very different. Some preliminary explanations for the remaining differences between theoretical and experimental electron densities include: (i) the impact of the crystal environment, despite the seemingly weak effect on the intramolecular integrals (see Figure 6.7), and (ii) different basis sets used to model the density in experimental (multipole expansions) and theoretical (contracted gaussians) frameworks.

7 Conclusions and Outlooks

Many interesting and useful chemical problems go beyond the rigid, isolated, unperturbed molecular model, and involve systems under electronic and geometric fluctuations, in complex environments. Extensions of existing scalar fields to such tasks are typically hampered by (i) their ineptitude to simultaneously capture the full range of covalent and non-covalent chemical interactions, and (ii) their dependence on electron wavefunctions, not always available for the systems of interest. Both limitations were overcome by the Density Overlap Region Indicator (DORI), an interpretative function recently developed in our laboratory and able to describe both covalent and non-covalent interactions, using only the widely available electron density and its derivatives. De Silva *et al.* assessed DORI's behavior for the typical, unperturbed model systems, setting the basis for the present thesis, which specifically exploited DORI to extend the application scope of DORI, and of molecular scalar fields in general.

The first challenging systems were molecules in photoexcited states. Time-Dependent Density Functional Theory (TDDFT), the mainstream method for modelling excited state, does not retrieve excited state wavefunctions, only excited state densities. Unlike other popular wavefunction-dependent scalar fields, the density-dependent DORI is perfectly suited for analyzing excited states densities obtained with TDDFT. In this thesis, we identified the excitation characters (*e.g.*, charge transfer, excimer, Rydberg, ...) of organic and organometallic compounds using intuitive DORI representations in real space. Integration of the electron density within DORI basin enabled fast characterization of domains gaining or losing electrons upon excitations, allowing for a quantification of electronic changes during photoexcitation processes. These applications allowed to confidently rationalize the atypical excited state dynamics of BODIPY derivatives observed by Prlj *et al.*²⁰⁷ DORI revealed the key intramolecular CH–F interactions in tert-butyl-BODIPY, which both destabilize the Franck-Condon region and stabilize the crossing region, explaining the peculiar fluorescence quenching in this molecule.

This thesis also apprehended interactions in highly fluxional molecules - molecular machines and switches - that are well-described by enhanced sampling molecular dynamics. DORI provided more effective and simpler descriptions than those given by traditional geometrical descriptors, common in molecular dynamics. Both conformational and electronic features of

the different systems were condensed to a 1-dimensional DORI value, simplifying the complex, high-dimensional conformational space. DORI was synergistically used to color-code sketch-map representations, enabling effective characterization of conformational regions.

Final applications focused on interactions within and between molecules in condensed phases, including (i) crystals at ambient and high pressure, and (ii) ligand in protein environment. Applying high pressure to crystals triggers phase transitions, dramatic changes in electronic structures or even chemical reactions, posing an interesting challenge for bonding descriptors. The simple visual DORI analysis captured key variations of an organic crystal under pressure, including (i) changes in covalent bonding behavior, (ii) the strong interplay between covalent and non-covalent interactions, in sharp contrast with usual ambient pressure observations, and (iii) the transfer of crystal anisotropy into covalent regions. The comprehensive interaction analysis exploited actual experimental electron densities, pioneering the field of visual interaction descriptors in high-pressure organic materials. Protein environment also enforces peculiar orientations between binding pockets and their ligands. This feature was highlighted by a peculiar N-CH₃-O interaction occurring during the methylation process of the α -amino group of histidine. DORI effectively revealed the nature of this slightly attractive interaction, set up from geometrical constraints of the protein environment, and influencing the methylation reaction.

This thesis demonstrated DORI's efficiency in solving non-trivial chemical problems, and set the stage for applying it to other tantalizing, yet unexplored, domains.

Similarity measures for molecular databases With ever growing molecular databases (*e.g.*, 166.4 billion stable small organic molecules in GDB-17), the search for efficient descriptors able to discover patterns is thriving. Current measures typically rely on geometrical features (bond lengths, angles, ...), embedded in dimensionality reduction algorithms. DORI fingerprints could serve as alternative parameters based on actual electronic structures, providing consistent descriptions of chemical interactions. DORI was already applied on sets of fluxional molecules containing more than 10⁴ conformers on Chapter 5, demonstrating DORI's applicability to datasets. Multi-component characterization, *e.g.*, including several descriptors either derived from DORI or other sources (toxicity, color, ...), is achievable by implementing them in dimensionality reduction algorithms, such as the sketch-map presented in Chapter 5. Metal-organic frameworks (MOFs) represent ideal candidates for a DORI based approach. Indeed, MOFs properties are already rationalized with large databases⁴⁵⁰ using geometrical parameters including cavity size and shape.⁴⁵¹ However, the inclusion of electronic properties is desirable to properly account for the chemical properties of MOF, a task ably performed using DORI descriptors that capture simultaneously geometrical and electronic properties. However, such large-scale investigations necessary require fast and accurate methods to generate electron densities, which might come from improved fragment density libraries.

Improving libraries of density fragments As an efficient density descriptor, particularly in chemically relevant regions, DORI can be used to directly assess the quality of $\rho(\mathbf{r})$ stemming from various methods (fragments, DFT, experimental) with respect to a reference one. The availability of mesh comparison software enables comparing DORIs in real space (see section 6.6), which can be either visualized (mesh-to-mesh Euclidean/Hausdorff distances), or included in statistical approaches using numerical similarity measures (*e.g.*, real-space R factor, Walker-Mezey index, or earth mover’s distance). Such comparison could help in the development of more accurate fragment densities. In particular, proatomic densities, which despite being one of the most cost-effective ways to construct an approximate molecular electron density still lack a reliable description of covalent regions. This could be addressed by fitting coefficients of atom-centered basis functions (spherical harmonics, atomic orbitals, ...) to a fragmented, benchmark $\rho(\mathbf{r})$ (*e.g.*, computed by high level *ab initio* methods). The fitting procedure would serve as a training set for machine-learning algorithms, which could analyze the relation between the local atomic environment and the fitted coefficients to afterwards relax crude $\rho(\mathbf{r})$ fragments into molecular-like densities. The overall quality of the density description could then be assessed by comparing 3D DORI maps from the exact and from machine-learned densities, naturally placing the strongest focus on chemically relevant regions.

Exploiting density-based molecular partitioning Recently, Zheng *et al.* introduced a joint SEDD/DORI partitioning criterion for Quantum Mechanics/Molecular Mechanics (QM/MM),¹⁴⁰ which offers several advantages: (i) the use of actual electron densities which avoids the arbitrariness of *e.g.*, geometrical parameters, (ii) a partitioning based on intuitive chemical interactions, and (iii) a possible adaptive scheme with SEDD/DORI evaluating the relevant active space during the molecular dynamic trajectory. Using such partitioning, as well as its adaptive version, further extends the range of perspective DORI applications into the multi-scale modeling of nanomaterials and bio-systems. Chemical reactions in explicit environment (*e.g.*, solvents, surfaces or proteins) is one interesting application. CO₂ reduction, for example, typically occurs on copper (or gold-copper) surfaces. Here, the mobile, CO₂ molecule could be treated using quantum mechanical methods and the catalyst surface using MM. When a CO₂ molecule interacts with the surface, *i.e.*, when their electron densities overlap, DORI could indicate that a section of the catalytic surface be included in the QM region, which will allow for reaction to occur. In such applications, DORI simultaneously gives criteria for system partitioning and provides the descriptor that alters the theoretical level describing the chemical reaction.

Automation of DORI evaluation DORI’s strength is in the visual description of chemical interactions. This becomes unpractical when targeting big data applications where (i) numerous structures must be analyzed, (ii) multiple interactions are present, (iii) interactions are sensitive to the chosen DORI isovalue. For such situations, it would be desirable to have an automatic and objective way to characterize DORI domains. In molecular scalar fields, this is typically done through the topological analysis of the function. As an alternative to developing

Chapter 7. Conclusions and Outlooks

DORI topology, (machine learned) visual recognition algorithms could easily replace the chemist's eye to rapidly recover DORI characteristic bonding patterns.

Closing words The visualization of covalent and non-covalent patterns using DORI provides insights into chemical interactions in complex systems. This work demonstrated the versatility and interpretative power of the DORI descriptor in retrieving chemical intuition for non-trivial problems. Ending with my opening citation, "it is ... by intuition that we discover"; so let us continue to extend and apply DORI to regain intuition in quantum chemistry.

A Topological analysis in chemistry

Beside their intuitive representation in real space, molecular scalar fields are particularly interesting thanks to the whole set of mathematical tools able to interpret them, regrouped under the term of topological analysis. The formalism is based on the theory of dynamical systems, initiated by H. Poincaré.²³ Its use in chemistry was pioneered by R. Bader, who applied it extensively for the analysis of the electron density $\rho(\mathbf{r})$.²⁴ It is noteworthy to mention that these tools might be applied to any scalar field, and thus any real space bonding descriptor, including DORI. However, the interpretation of the mathematical expressions in terms of chemical concepts might differ for different bonding descriptors. In this appendix, the examples focus on the topology of $\rho(\mathbf{r})$.

A first standard method to apprehend a scalar field is to search and characterize its critical points (CP). This step is usually performed using the Hessian matrix of the scalar field:

$$\mathbf{H}f(\mathbf{r}) = \begin{pmatrix} \frac{\partial^2 f}{\partial x^2} & \frac{\partial^2 f}{\partial x \partial y} & \frac{\partial^2 f}{\partial x \partial z} \\ \frac{\partial^2 f}{\partial y \partial x} & \frac{\partial^2 f}{\partial y^2} & \frac{\partial^2 f}{\partial y \partial z} \\ \frac{\partial^2 f}{\partial z \partial x} & \frac{\partial^2 f}{\partial z \partial y} & \frac{\partial^2 f}{\partial z^2} \end{pmatrix} \quad (\text{A.1})$$

The diagonalization of $\mathbf{H}f(\mathbf{r})$ produces a set of eigenvalues and eigenvectors, which correspond to the extent of curvature of the scalar field, and to the direction of this curvature. A popular classification of CPs exploits the rank (ω , the number of non-zero eigenvalues) and the signature (σ , the sum of eigenvalues signs) of the Hessian matrix, usually noted as $\text{CP}(\omega, \sigma)$. In real space, critical points corresponding to maxima, 2-saddles, 1-saddles and minima are thus denoted by (3,-3), (3,-1), (3,-2) and (3,3), respectively. When related to $\rho(\mathbf{r})$, such maxima are found near nuclei. Similarly, (3,-1) CP of $\rho(\mathbf{r})$ are always found between two interacting atoms, which might be exploited to determine bond positions.

Besides CP evaluation, the Hessian matrix also provides for the Laplacian of the electron density:

$$L = \nabla^2 \rho = \frac{\partial^2 \rho}{\partial x^2} + \frac{\partial^2 \rho}{\partial y^2} + \frac{\partial^2 \rho}{\partial z^2} \quad (\text{A.2})$$

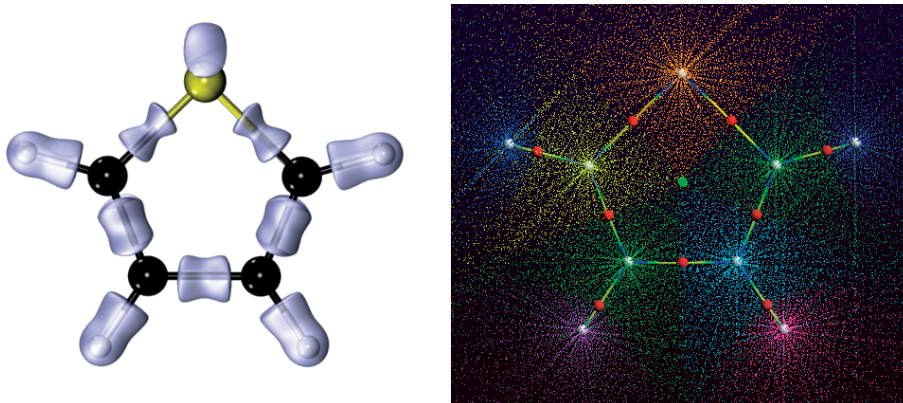


Figure A.1 – Isosurface of $\nabla^2\rho(\mathbf{r}) = -0.4$ (left) and QTAIM colored by basins for the thiophene molecule (right)

which is a local indicator of electron depletion or accumulation. $\nabla^2\rho$ can formally reveal atomic shell structures (for atoms below the 4th row¹¹⁴) as well as bonding regions and lone pairs. Besides, the three Hessian eigenvalues used to calculate the Laplacian, namely λ_1 , λ_2 and λ_3 , are ordered by magnitude. The sign of the second eigenvalue λ_2 is exploitable to determine if an observed interaction is of attractive or repulsive nature.²⁴ Another particularly valuable quantity is the gradient vector field $\nabla f(\mathbf{r})$ associated with a given scalar field $f(\mathbf{r})$. In $\nabla F(\mathbf{r})$, each vector is directed according to the steepest slope of the field lines, *i.e.*, lines where $f(\mathbf{r})$ remains constant. Furthermore, each trajectory going through $\mathbf{r} \neq \mathbf{r}_c$ is unique, and connect two extrema of $f(\mathbf{r})$. Generally, several trajectories of $\nabla f(\mathbf{r})$ end up at the same critical points. When the CP is a maximum of $f(\mathbf{r})$, the resulting set of vector fields ending at this CP define a basin Ω , and the CP is called an "attractor". Different basins are separated from each other by trajectories ending at a saddle point of $f(\mathbf{r})$ called separatrices. The net result of this association of trajectories is a complete partitioning of the real space into non-overlapping basins and separatrices. As in QTAIM the attractors are found near nuclei, the obtained basins can be attributed to a given atom.

One of the interest of such partitioning is the possibility to compute a property inside a given basin. In fact, any property computed by the normal expectation value $\langle O \rangle$ of a given (Hermitian) operator \hat{O} might be written as a sum over the basins Ω_X :

$$\langle O \rangle = \sum_{X=1}^n \langle \psi | \hat{O} | \psi \rangle_{\Omega_X} \quad (\text{A.3})$$

For example, it is possible to compute the volume of a given basin as the integral over the basin:

$$V(\Omega_X) = \int_{\Omega_X} dv \quad (\text{A.4})$$

Similarly, the electron population within a basin can be computed as:

$$V(\Omega_X) = \int_{\Omega_X} \rho(\mathbf{r}) d\mathbf{r} \quad (\text{A.5})$$

Such partitioning schemes allows for rigorous definitions of oxidation numbers and formal charges on atoms. Furthermore, the basins might be exploited to generate libraries of transferable atoms,⁴⁵² as well as for energy decomposition analysis.^{453,454}

It is noteworthy to mention at this point that a basin might also be defined using a given value f of the scalar field. The number and shape of the obtained basin will be greatly influenced by the chosen isovalue f , but an effective real space partitioning will nonetheless be obtained. The basins will be located around one or several maxima of $f(\mathbf{r})$. Despite their isovalue-dependent nature, f -localization domains may still be used to compute an average property inside the basin (*e.g.*, electronic population). This might also be used advantageously, as different partitioning of the real space might be targeted by different isovalues. At the limit $n \rightarrow \max(f(\mathbf{r}))$, the basin is restricted to a single point corresponding to the CP. Despite the highly local nature of the CP, it is also possible to evaluate a given quantity at this point. This feature was widely exploited within the QTAIM framework to rationalize *e.g.*, bond ionicity, covalency, reactivity, electron delocalization, as well as for less conventional MSF domains such as statistical quantitative structure-to-activity measures (QSAR)⁴⁵⁵ and drug development.⁴⁵⁶

The range of QTAIM applications is incredibly broad, and has been the topic of several reviews and book chapters. However, the formal mathematical description of QTAIM is not always compatible with chemical thinking. A famous example is the difference between QTAIM bond path and "chemical bonds", as expressed in the Lewis picture. The former is linked with the idea of electron charge accumulation between pair of atoms, which also happen between atoms sharing van der Waals interactions, while the latter is dominated by the electron pair concept, *i.e.*, a covalent bond. This fundamental difference led to several controversies and misinterpretations of QTAIM bonds in terms of chemical bonds.^{25–28}

Beside the sometimes cryptic nature of QTAIM mathematical representations, one should also mention the rapidly increasing computational cost of evaluating the Hessian matrix for large systems. Finally, the 3D-representation of QTAIM are usually rather unintuitive for the casual user.

B Supplementary Information for Visualizing and Quantifying Interactions in the Excited State

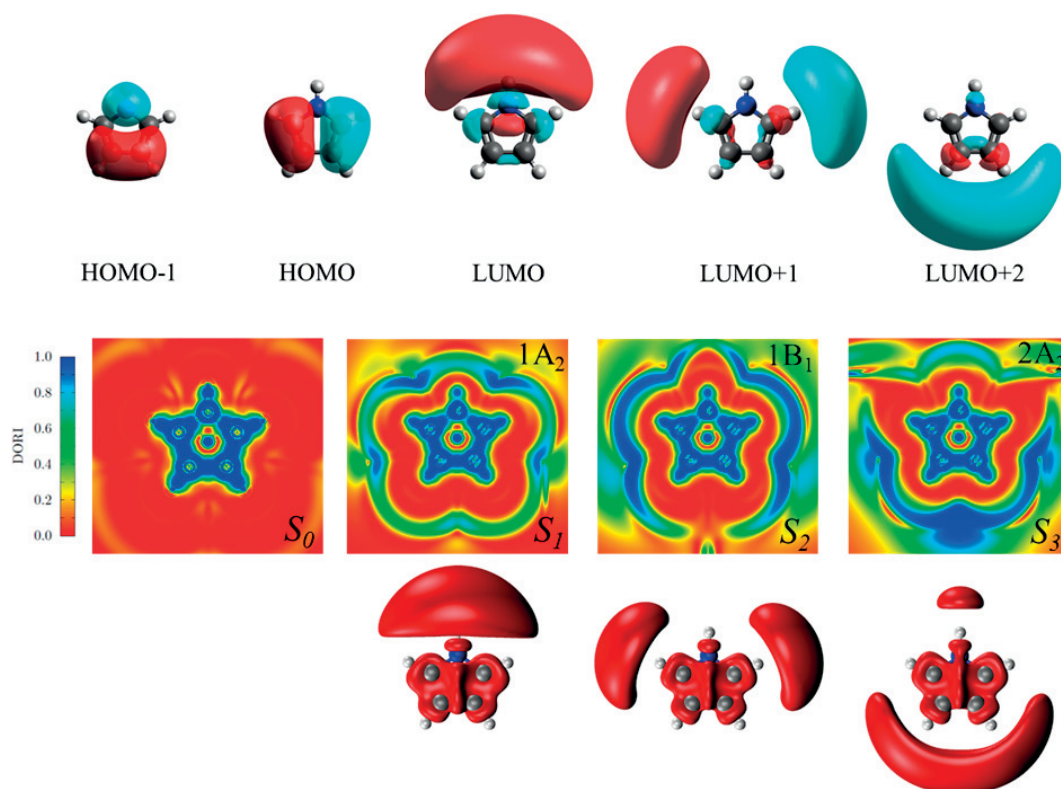


Figure B.1 – (top) Canonical orbitals participating to the S_1 - S_3 singlet excitations (isovalues = ± 0.02), (center) DORI map in the molecular plane, (bottom) electron gain regions after excitation based on the relaxed electron density difference ($\rho(S_n) - \rho(S_0)$) computed at the (TD-)PBE0/def2-TZVP-aug level (isovalue = $+0.0005$ a.u.) on the ground state ω B97X-D/cc-pVDZ optimized geometry.

Appendix B. Supplementary Information for Visualizing and Quantifying Interactions in the Excited State

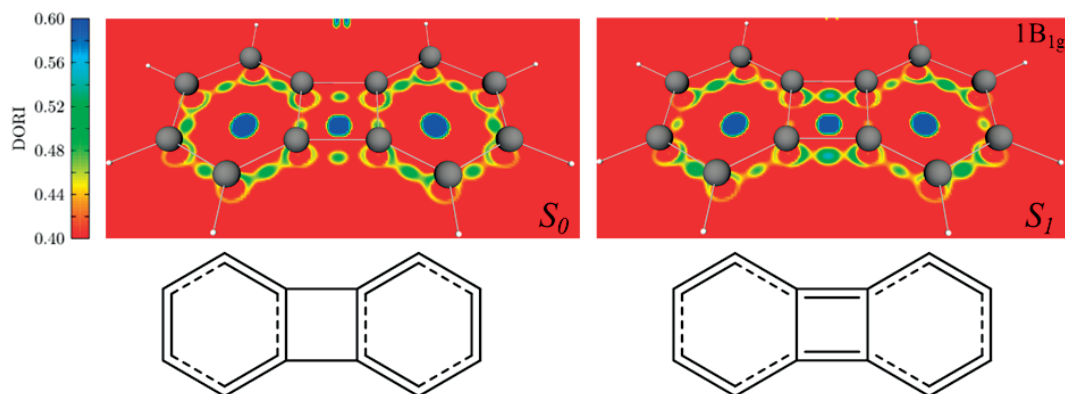


Figure B.2 – (Top) DORI map in the π -region (0.5\AA below the molecular plane) for biphenylene at the (TD-)B3LYP/TZP level in the B3LYP/TZP ground state geometry for the ground (left) and first singlet excited state (right). Bottom: Lewis structures based on DORI behavior

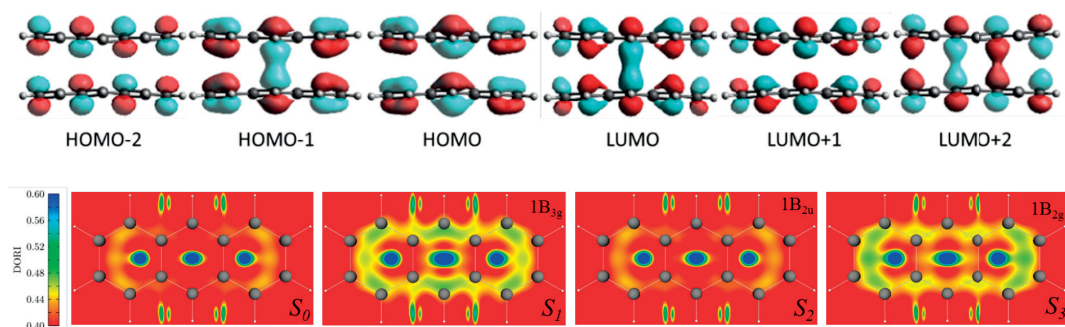


Figure B.3 – (Top) Orbitals participating to the S_1 - S_3 singlet excitations (isovalues= ± 0.03) and (bottom) DORI maps in intermolecular plane for the anthracene-anthracene dimer at the (TD-)PBE0/TZP level in its S_1 excimer TD- ω B97X-D/def2-SVP optimized geometry.

| method | transition | sym. | E [eV] | f | excitation | contrib. (%) |
|-----------|------------|------|--------|--------|---------------------------|--------------|
| CAM-B3LYP | S_1 | 1A | 3.11 | 0.0000 | HOMO \rightarrow LUMO | 100 |
| | S_2 | 2A | 3.23 | 0.0629 | HOMO-1 \rightarrow LUMO | 100 |
| | S_3 | 3A | 4.65 | 0.2727 | HOMO-2 \rightarrow LUMO | 97 |

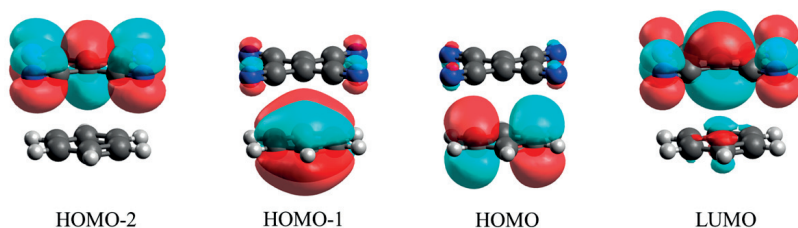
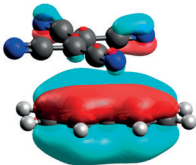
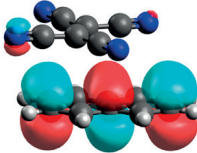
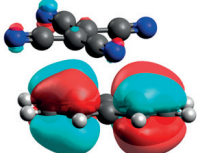
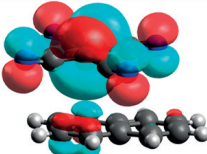


Figure B.4 – Excitation energies, oscillator strengths, orbital contributions and representations (isovalue= ± 0.02) at the TD-CAM-B3LYP for the first three singlet excitations using a cc-pVDZ basis set for the tetracyanoethylene-benzene charge transfer complex in its ground state ω B97X-D/def2-SVP optimized geometry.

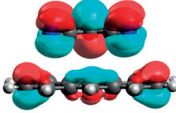
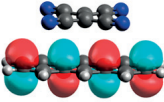
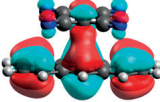
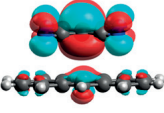
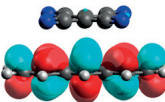
| method | transition | sym. | E [eV] | f | excitation | | contrib. (%) |
|-----------|------------|------|--------|--------|------------|--------|--------------|
| CAM-B3LYP | S_1 | 1A | 2.36 | 0.0571 | HOMO | → LUMO | 99 |
| | S_2 | 2A | 3.01 | 0.0190 | HOMO-1 | → LUMO | 99 |
| | S_3 | 3A | 4.26 | 0.0196 | HOMO-2 | → LUMO | 98 |

HOMO-2
HOMO-1
HOMO
LUMO

Figure B.5 – Excitation energies, oscillator strengths, orbital contributions and representations (isovalue= ± 0.02) at the TD-CAM-B3LYP for the first three singlet excitations using a cc-pVDZ basis set for the tetracyanoethylene-naphtalene charge transfer complex in its ground state ω B97X-D/def2-SVP optimized geometry.

| method | transition | sym. | E [eV] | f | excitation | | contrib. (%) |
|-----------|------------|------|--------|--------|------------|----------|--------------|
| CAM-B3LYP | S_1 | 1A | 2.22 | 0.1421 | HOMO | → LUMO | 100 |
| | S_2 | 2A | 3.11 | 0.0000 | HOMO-1 | → LUMO | 99 |
| | S_3 | 3A | 3.61 | 0.0348 | HOMO-3 | → LUMO | 96 |
| | | | | | HOMO-1 | → LUMO+1 | 2 |

HOMO-3
HOMO-1
HOMO
LUMO
LUMO+1

Figure B.6 – Excitation energies, oscillator strengths, orbital contributions and representations (isovalue= ± 0.02) at the TD-CAM-B3LYP for the first three singlet excitations using a cc-pVDZ basis set for the tetracyanoethylene-anthracene charge transfer complex in its ground state ω B97X-D/def2-SVP optimized geometry.

Appendix B. Supplementary Information for Visualizing and Quantifying Interactions in the Excited State

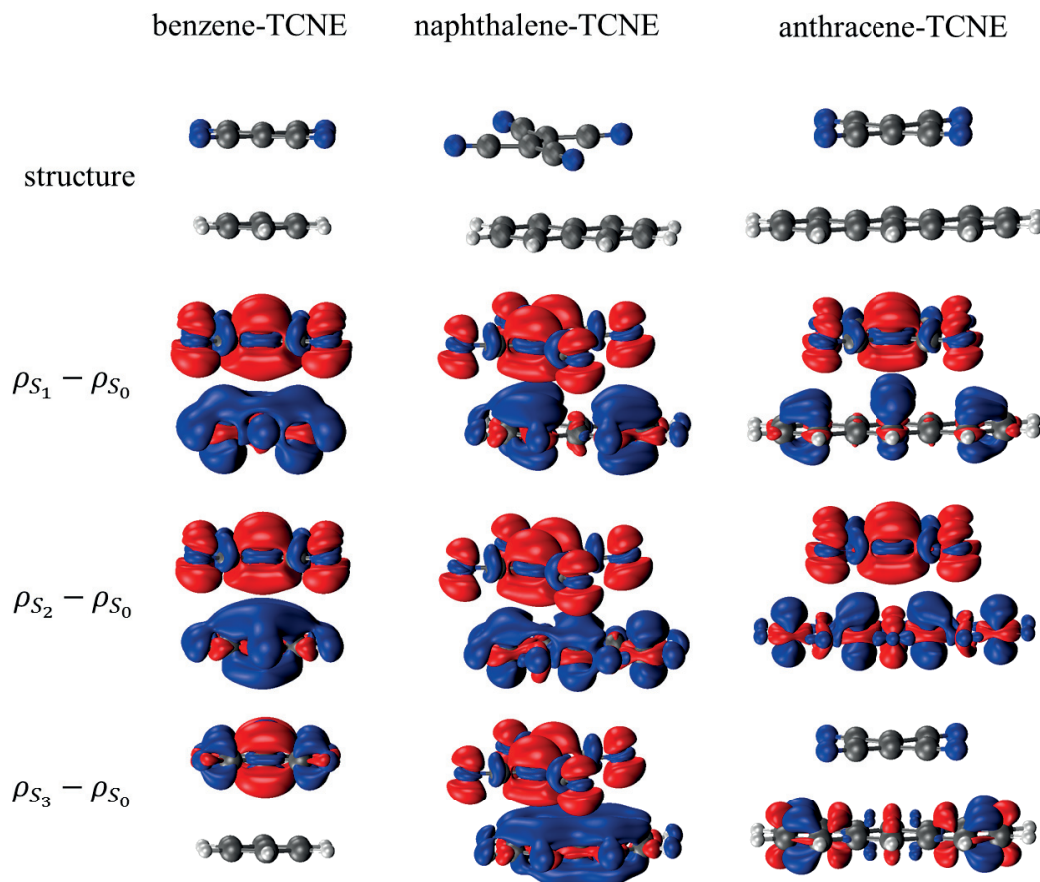


Figure B.7 – Density differences ($\rho_{S_n} - \rho_{S_0}$, $n \in \{1, 2, 3\}$) at the (TD-)CAM-B3LYP/ccpVDZ level for (top) benzene-TCNE (isovalue= 0.005), (middle) naphthalene- TCNE (isovalue= 0.005), and (bottom) anthracene-TCNE (isovalue=0.0015). Positive values in red, negative in blue.

| transition | sym. | E[eV] | f | excitation | contribution % | |
|----------------|------|-------|--------|---------------|----------------|----|
| S ₁ | B | 3.6 | 0.0719 | HOMO → LUMO | | 87 |
| T ₁ | A | 2.1 | 0.0000 | HOMO → LUMO | | 48 |
| | | | | HOMO-2 → LUMO | | 29 |
| | | | | HOMO-1 → LUMO | | 13 |

Figure B.8 – Transition energy, oscillator strength and orbital contribution for the singlet excitations for the FIr(acac) complex at the TD-CAMB3LYP/cc-pVDZ LANL2DZ level in the ground state and triplet (TD-)ωB97X-D/def2-SVP LANL2DZ optimized geometry

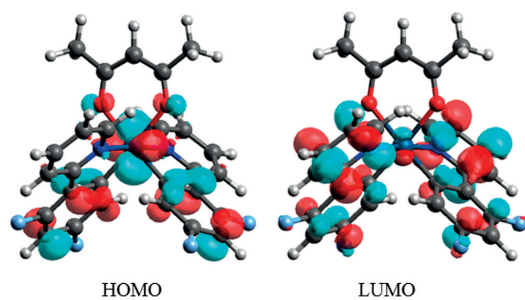


Figure B.9 – Orbital representations (isovalue= ± 0.04) at the CAM-B3LYP level for the first singlet excitation using a cc-pVDZ and LANL2DZ basis set (Ir) for the FIr(acac) complex in its ground state ω B97X-D/def2-SVP optimized geometry

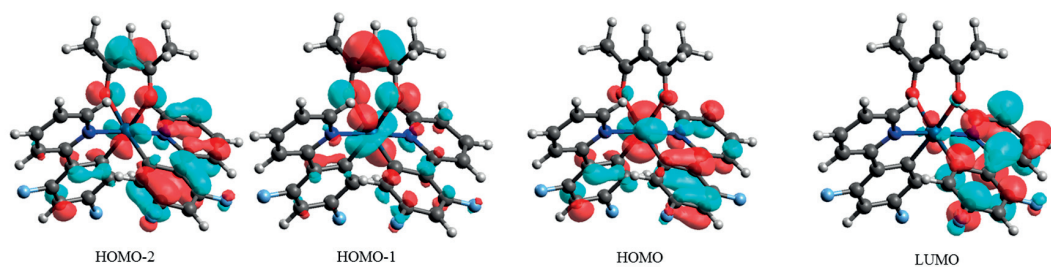


Figure B.10 – Orbital representations (isovalue= ± 0.04) at the CAM-B3LYP level for the first triplet excitation using a cc-pVDZ and LANL2DZ basis set for the FIr(acac) complex in the TD- ω B97XD/def2-SVP optimized T_1 geometry

C Supplementary Information for Analyzing Fluxional Molecules using DORI

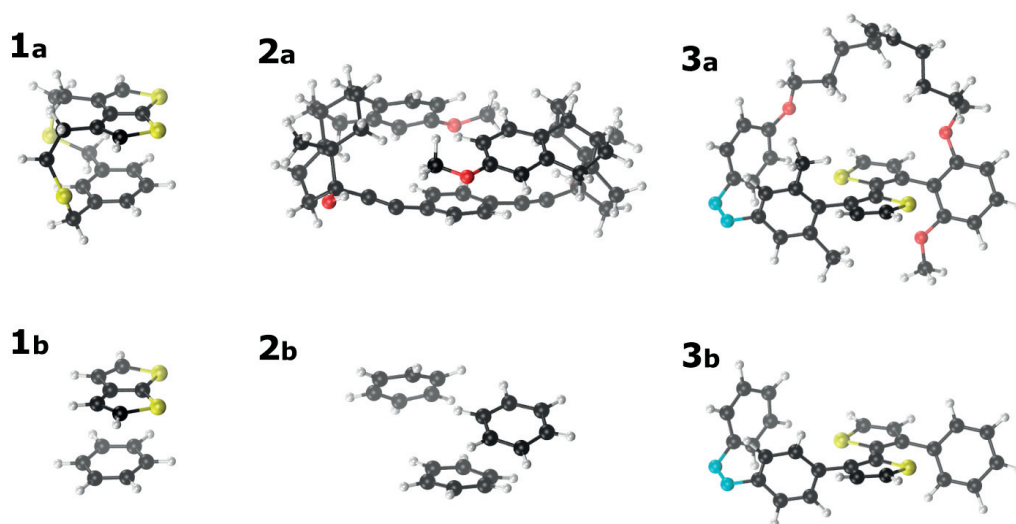


Figure C.1 – Three dimensional representation of Thieno-[2,3-b]-thiophene (1), the molecular rotor (2) and the photochromic torsional switch (3). Molecular dynamics trajectories were run on full systems (a), DORI was computed on truncated systems (b), to accelerate the DORI analysis.

Adaptive Natural Density Partitioning We exploited the Adaptive Natural Density Partitioning (AdNDP) to localize σ and π molecular orbitals on the Photochromic Torsional Switch (PTS) system. This partitioning represents the electronic structure in terms of n -center (nc) two-electron (nc-2e) bonding patterns. The AdNDP method is able to retrieve both conventional Lewis types (*e.g.*, core electron, lone pairs (1c-2e), covalent bond (2c-2e)) and

delocalized bonding pattern (*e.g.*, π -conjugation) spanning the interval from one to the total amount of atoms in a molecular system. The PTS model system is composed by 110 electronic pairs. Exploiting the AdNDP method, we obtained 42 one-center two-electrons (1c-2e) cores and lone pairs electronic pairs with an occupation number threshold of 0.2e, 52 two-center two-electrons (2c-2e) localized bonds with a threshold of 0.042e and 16 delocalized bonding patterns (48c-2e, threshold of 0.01e) corresponding to the π -conjugation of the PTS system.

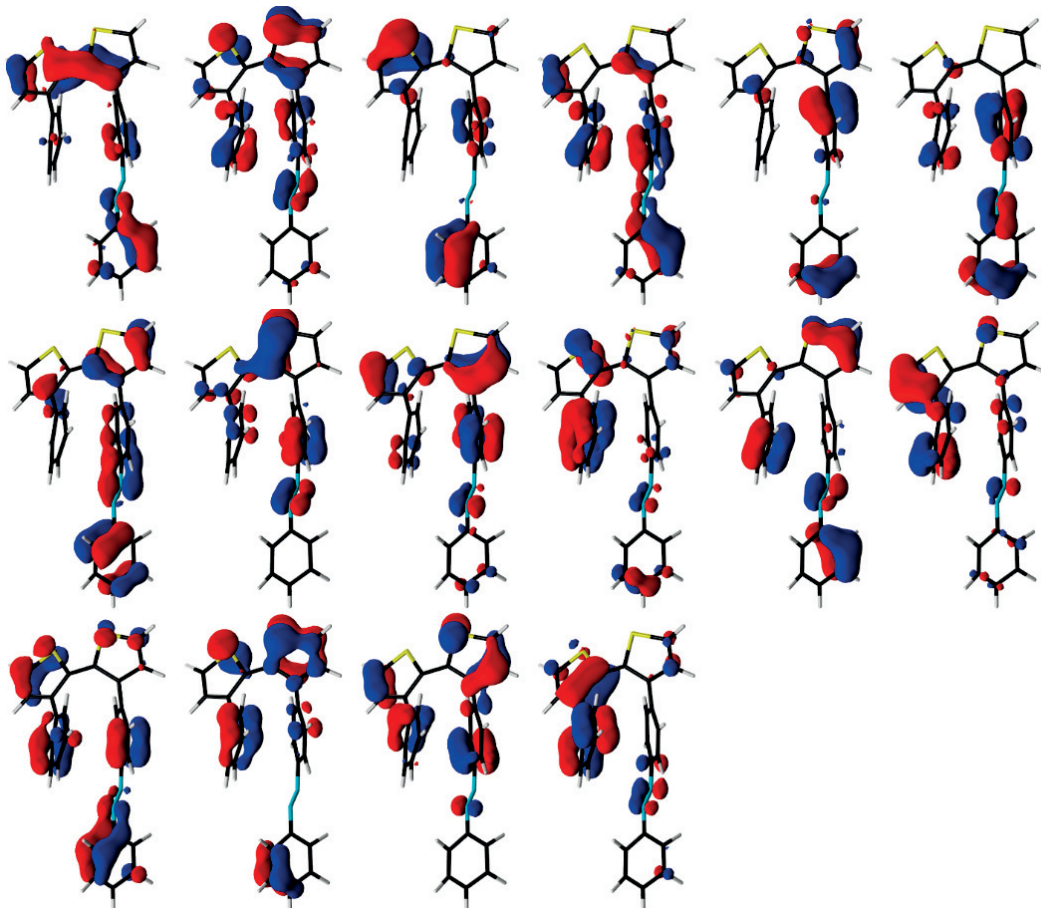


Figure C.2 – All sixteen AdNDP π -orbitals of the PTS system used for DORI π computations. Orbital order is arbitrary within AdNDP framework.

Sketch-map The sketch-map iteratively optimize the objective function:

$$S^2 = \sum [i, j] [F[D(X_i, X_j)] - f[d(x_i, x_j)]]^2 \quad (\text{C.1})$$

measuring the mismatch between similarities in atomic configurations $D(X_i, X_j)$, and similarities in the low-dimensional projection $d(x_i, x_j)$. The transformations F and f are non-linear sigmoid functions of the form:

$$f(r) = 1 - \left(1 + (2^{a/b} - 1) \left(\frac{r}{\sigma} \right)^a \right)^{(-b/a)} \quad (\text{C.2})$$

For each system, parameters were carefully chosen following the procedure detailed in²⁷⁰. For the photoswitch, the parameters were chosen as ($\sigma = 0.02$, $A = 4$, $B = 4$, $a = 2$, $b = 4$), where A and B are the exponents used for the high-dimensionality representation F , a and b are the exponents used for the low-dimensionality representation f , and σ is the threshold for the switching function. For the rotor, the set of chosen parameters are ($\sigma = 0.05$, $A = 4$, $B = 2$, $a = 2$, $b = 2$).

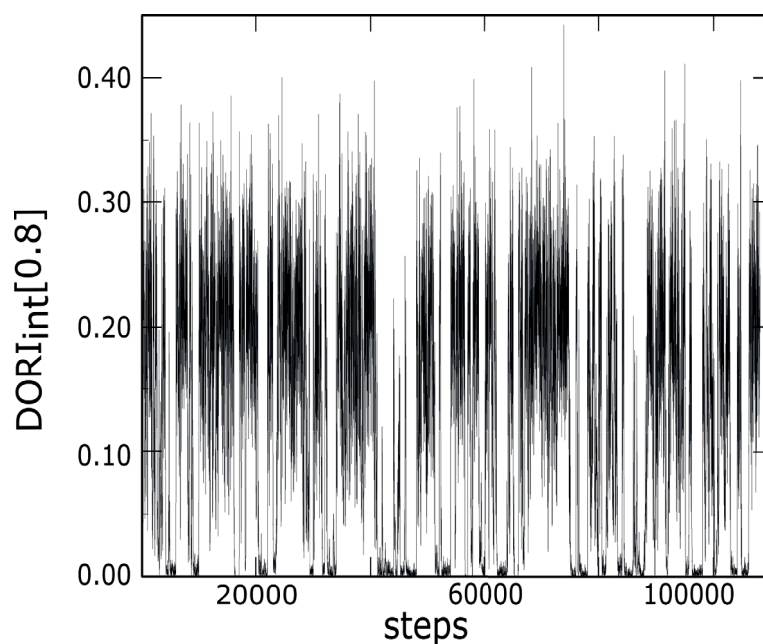


Figure C.3 – Integral of the electron density ($\text{DORI}_{int}[0.8]$) within the intramolecular $\text{DORI}=0.8$ domain of the truncated dithiocyclophane, for all 54 MD trajectories merged together. DORI are computed on electron densities relaxed at the PBE/6-31G* level, on frozen DFTB3/3OB-UFF MD geometries.

D Supplementary Information for DORI Assessing Electron Densities

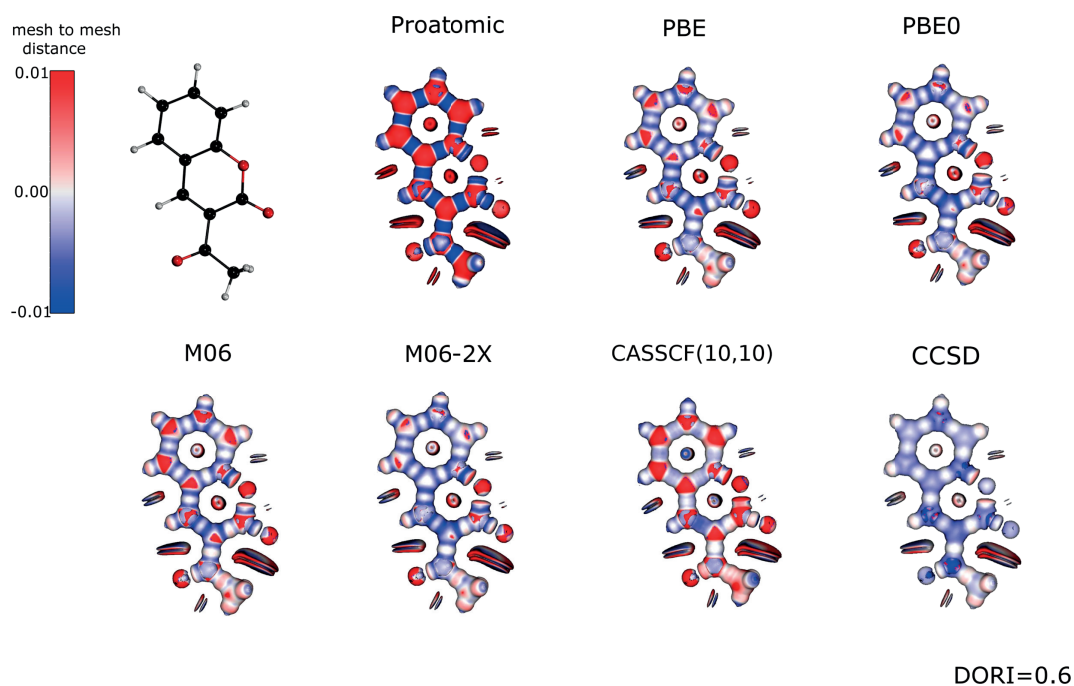


Figure D.1 – Mesh to mesh Euclidian distances [au] between DORI=0.6 isosurfaces of the 3-acetylcoumarin using DORI computed on the experimental electron density as a reference.

Appendix D. Supplementary Information for DORI Assessing Electron Densities

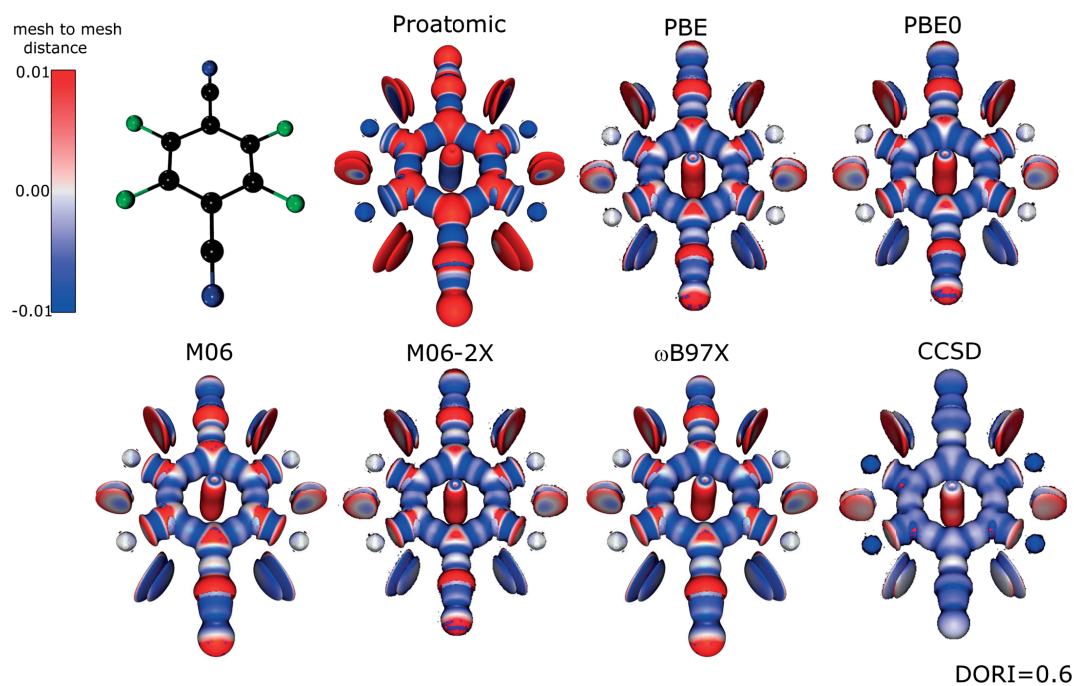


Figure D.2 – Mesh to mesh Euclidian distances [au] between DORI=0.6 isosurfaces of the tetrafluoroterephthalonitrile using DORI computed on the experimental electron density as a reference.

Bibliography

- [1] Parr, R. G. *Density Functional Theory in Chemistry*; Springer US, 1985.
- [2] Parr, R. G.; Donnelly, R. A.; Levy, M.; Palke, W. E. *J. Chem. Phys.* **1978**, *68*, 3801–3807.
- [3] Gonthier, J. E.; Steinmann, S. N.; Wodrich, M. D.; Corminboeuf, C. *Chem. Soc. Rev.* **2012**, *41*, 4671–87.
- [4] Pastorczak, E.; Corminboeuf, C. *J. Chem. Phys.* **2017**, *146*, 120901.
- [5] Becke, A. D.; Edgecombe, K. E. *J. Chem. Phys.* **1990**, *92*, 5397.
- [6] Silvi, B.; Savin, A. *Nature* **1994**, *371*, 683–686.
- [7] Ayers, P. L. et al. *Comput. Theor. Chem.* **2015**, *1053*, 2–16.
- [8] de Silva, P.; Corminboeuf, C. *J. Chem. Theory Comput.* **2014**, *10*, 3745–3756.
- [9] Johnson, E. R.; Keinan, S.; Mori-Sanchez, P.; Contreras-Garcia, J.; Cohen, A. J.; Yang, W. *J. Am. Chem. Soc.* **2010**, *132*, 6498–506.
- [10] Contreras-Garcia, J.; Yang, W.; Johnson, E. R. *J. Phys. Chem. A* **2011**, *115*, 12983–12990.
- [11] de Silva, P.; Korchowiec, J.; Wesolowski, T. A. *ChemPhysChem* **2012**, *13*, 3462–5.
- [12] Vannay, L.; Brémond, E.; de Silva, P.; Corminboeuf, C. *Chem. - A Eur. J.* **2016**, *22*, 18442–18449.
- [13] Hohenberg, P. *Phys. Rev.* **1964**, *136*, B864–B871.
- [14] Ferri, N.; DiStasio, R. A.; Ambrosetti, A.; Car, R.; Tkatchenko, A. *Phys. Rev. Lett.* **2015**, *114*, 176802.
- [15] Politzer, P.; Laurence, P. R.; Jayasuriya, K. *Environ. Health Perspect.* **1985**, *61*, 191–202.
- [16] Politzer, P.; Murray, J. S.; Peralta-Inga, Z. *Int. J. Quantum Chem.* **2001**, *85*, 676–684.
- [17] Khan, I.; Panini, P.; Khan, S. U.-D.; Rana, U. A.; Andleeb, H.; Chopra, D.; Hameed, S.; Simpson, J. *Cryst. Growth Des.* **2016**, *16*, 1371–1386.
- [18] Duarte, D. J. R.; de las Vallejos, M. M.; Peruchena, N. M. *J. Mol. Model.* **2010**, *16*, 737–748.
- [19] Taylor, M. S. *Nat. Chem.* **2014**, *6*, 1029–1031.
- [20] Sinnokrot, M. O.; Sherrill, C. D. *J. Am. Chem. Soc.* **2004**, *126*, 7690–7697.
- [21] Sinnokrot, M. O.; Sherrill, C. D. *J. Phys. Chem. A* **2006**, *110*, 10656–10668.
- [22] Wheeler, S. E.; Bloom, J. W. G. *J. Phys. Chem. A* **2014**, *118*, 6133–6147.
- [23] Poincaré, H. *Les Méthodes Nouvelles de la Mécanique Céleste*; Gauthier-Villars, 1899.
- [24] Bader, R. F. W. *Atoms in Molecules: A Quantum Theory*; Oxford University Press, 1990.
- [25] Grimme, S.; Mück-Lichtenfeld, C.; Erker, G.; Kehr, G.; Wang, H.; Beckers, H.; Willner, H. *Angew. Chem. Int. Ed.* **2009**, *48*, 2592–2595.
- [26] Cerpa, E.; Krapp, A.; Vela, A.; Merino, G. *Chem. - A Eur. J.* **2008**, *14*, 10232–10234.

Bibliography

- [27] Cerpa, E.; Krapp, A.; Flores-Moreno, R.; Donald, K. J.; Merino, G. *Chem. - A Eur. J.* **2009**, *15*, 1985–1990.
- [28] Bader, R. F. W. *J. Phys. Chem. A* **2009**, *113*, 10391–10396.
- [29] Grin, Y.; Savin, A.; Silvi, B. In *The ELF Perspective of chemical bonding, in The Chemical Bond : Fundamental Aspects of Chemical Bonding*; Wiley-VCH, Ed.; 2014.
- [30] Daudel, R. *C R Hebd Seances Acad Sci* **1953**, *237*, 601–603.
- [31] Daudel, R.; Brion, H.; Odier, S. *J. Chem. Phys.* **1955**, *23*, 2080–2083.
- [32] Bader, R.; Stephens, M. *Chem. Phys. Lett.* **1974**, *26*, 445–449.
- [33] Bader, R. F. W.; Stephens, M. E. *J. Am. Chem. Soc.* **1975**, *97*, 7391–7399.
- [34] Savin, A. *Probability Distributions and Valence Shells in Atoms. In: Reviews of Modern Quantum Chemistry, A Celebration of the Contributions of Robert G Parr*; World scientific, 2002.
- [35] Gallegos, A.; Carbó-Dorca, R.; Lodier, E.; Cancès, E.; Savin, A. *J. Comput. Chem.* **2005**, *26*, 455–460.
- [36] Menendez, M.; Martin Pendas, A.; Braïda, B.; Savin, A. *Comput. Theor. Chem.* **2015**, *1053*, 142–149.
- [37] Scemama, A.; Caffarel, M.; Savin, A. *J. Comput. Chem.* **2007**, *28*, 442–454.
- [38] Causà, M.; Savin, A. *J. Phys. Chem. A* **2011**, *115*, 13139–13148.
- [39] Savin, A.; Cancès, E.; Keriven, R.; Lodier, F. *Theor. Chem. Acc.* **2004**, *111*, 373–380.
- [40] Lüchow, A.; Petz, R. *J. Comput. Chem.* **2011**, *32*, 2619–2626.
- [41] Becke, A. D. *Int. J. Quantum Chem.* **1983**, *23*, 1915–1922.
- [42] Becke, A. D. *Int. J. Quantum Chem.* **1985**, *27*, 585–594.
- [43] Bader, R. F. W.; Gillespie, R. J.; MacDougall, P. J. *J. Am. Chem. Soc.* **1988**, *110*, 7329–7336.
- [44] Luken, W. L.; Beratan, D. N. *Theor. Chim. Acta* **1982**, *61*, 265–281.
- [45] Dobson, J. F. *J. Chem. Phys.* **1991**, *94*, 4328–4333.
- [46] Savin, A. *J. Chem. Sci.* **2005**, *117*, 473–475.
- [47] Burdett, J. K.; McCormick, T. A. *J. Phys. Chem. A* **1998**, *102*, 6366–6372.
- [48] Nalewajski, R. F.; Köster, A. M.; Escalante, S. *J. Phys. Chem. A* **2005**, *109*, 10038–10043.
- [49] Li Manni, G.; Carlson, R. K.; Luo, S.; Ma, D.; Olsen, J.; Truhlar, D. G.; Gagliardi, L. *J. Chem. Theory Comput.* **2014**, *10*, 3669–3680.
- [50] Gagliardi, L.; Truhlar, D. G.; Li Manni, G.; Carlson, R. K.; Hoyer, C. E.; Bao, J. L. *Acc. Chem. Res.* **2017**, *50*, 66–73.
- [51] Savin, A.; Becke, A. D.; Flad, J.; Nesper, R.; Preuss, H.; von Schnering, H. G. *Angew. Chem. Int. Ed.* **1991**, *30*, 409–412.
- [52] Savin, A.; Jepsen, O.; Flad, J.; Andersen, O. K.; Preuss, H.; von Schnering, H. G. *Angew. Chem. Int. Ed.* **1992**, *31*, 187–188.
- [53] Savin, A.; Nesper, R.; Wengert, S.; Fässler, T. F. *Angew. Chem. Int. Ed.* **1997**, *36*, 1808–1832.
- [54] Savin, A.; Silvi, B.; Colonna, E.; Coionna, F. *Can. J. Chem.* **1996**, *74*, 1088–1096.
- [55] Andrés, J.; Berski, S.; Silvi, B. *Chem. Commun.* **2016**, *52*, 8183–8195.
- [56] Chesnut, D. *Chem. Phys.* **2001**, *271*, 9–16.
- [57] Raub, S.; Jansen, G. *Theor. Chem. Acc.* **2001**, *106*, 223–232.
- [58] Poater, J.; Duran, M.; Solà, M.; Silvi, B. *Chem. Rev.* **2005**, *105*, 3911–3947.

- [59] Steinmann, S. N.; Corminboeuf, C. *J. Chem. Phys.* **2011**, *134*, 44117.
- [60] Feixas, F.; Matito, E.; Poater, J.; Solà, M. *Chem. Soc. Rev.* **2015**, *44*, 6434–6451.
- [61] Fourré, I.; Silvi, B.; Sevin, A.; Chevreau, H. *J. Phys. Chem. A* **2002**, *106*, 2561–2571.
- [62] Fourré, I.; Silvi, B. *Heteroat. Chem.* **2007**, *18*, 135–160.
- [63] Shaik, S.; Danovich, D.; Silvi, B.; Lauvergnat, D. L.; Hiberty, P. C. *Chemistry* **2005**, *11*, 6358–6371.
- [64] Llusar, R.; Beltrán, A.; Andrés, J.; Fuster, F.; Silvi, B. *J. Phys. Chem. A* **2001**, *105*, 9460–9466.
- [65] Andrés, J.; Feliz, M.; Fraxedas, J.; Hernández, V.; López-Navarrete, J. T.; Llusar, R.; Sauthier, G.; Sensato, F. R.; Silvi, B.; Bo, C.; Campanera, J. M. *Inorg. Chem.* **2007**, *46*, 2159–2166.
- [66] Gillespie, R. *Coord. Chem. Rev.* **2002**, *233–234*, 53–62.
- [67] Silvi, B. *Phys. Chem. Chem. Phys.* **2004**, *6*, 256–260.
- [68] Grabowski, S. J. *Chem. Rev.* **2011**, *111*, 2597–2625.
- [69] Fuster, F.; Silvi, B. *Theor. Chem. Acc.* **2000**, *104*, 13–21.
- [70] Gutiérrez-Oliva, S.; Joubert, L.; Adamo, C.; Bulat, F. A.; Zagal, J. H.; Toro-Labbé, A. *J. Phys. Chem. A* **2006**, *110*, 5102–5107.
- [71] Fuster, F.; Grabowski, S. J. *J. Phys. Chem. A* **2011**, *115*, 10078–10086.
- [72] Silvi, B.; Fourré, I.; Alikhani, M. E. *Monatshefte für Chemie - Chem. Mon.* **2005**, *136*, 855–879.
- [73] Silvi, B. *The Relevance of the ELF Topological Approach to the Lewis, Kossel, and Langmuir Bond Model. In: The Chemical Bond II. Structure and Bonding, vol 170*; Springer, 2015.
- [74] Kohout, M.; Pernal, K.; Wagner, F. R.; Grin, Y. *Theor. Chem. Acc.* **2004**, *112*, 453–459.
- [75] Bader, R. F. W.; Johnson, S.; Tang, T.-H.; Popelier, P. L. A. *J. Phys. Chem.* **1996**, *100*, 15398–15415.
- [76] Kohout, M. *Electron Pairs in Position Space. In: The Chemical Bond II. Structure and Bonding, vol 170*; Springer, 2015.
- [77] Wiberg, K. B.; Hadad, C. M.; Foresman, J. B.; Chupka, W. A. *J. Phys. Chem.* **1992**, *96*, 10756–10768.
- [78] Handy, N. C.; Schaefer, H. F. *J. Chem. Phys.* **1984**, *81*, 5031.
- [79] Wang, Y. A.; Govind, N.; Carter, E. A. *Phys. Rev. B* **1999**, *60*, 16350–16358.
- [80] Xia, J.; Huang, C.; Shin, I.; Carter, E. A. *J. Chem. Phys.* **2012**, *136*, 084102.
- [81] Jayatilaka, D. *Phys. Rev. Lett.* **1998**, *80*, 798–801.
- [82] Grimwood, D. J.; Jayatilaka, D. *Acta Crystallogr. Sect. A Found. Crystallogr.* **2001**, *57*, 87–100.
- [83] Jayatilaka, D.; Grimwood, D. J. *Acta Crystallogr. Sect. A Found. Crystallogr.* **2001**, *57*, 76–86.
- [84] Jayatilaka, D.; Grimwood, D. *Acta Crystallogr. Sect. A Found. Crystallogr.* **2004**, *60*, 111–119.
- [85] Grabowsky, S.; Weber, M.; Jayatilaka, D.; Chen, Y.-S.; Grabowski, M. T.; Brehme, R.; Hesse, M.; Schirmeister, T.; Luger, P. *J. Phys. Chem. A* **2011**, *115*, 12715–12732.
- [86] Chęcińska, L.; Mebs, S.; Ośmiałowski, B.; Zakrzewska, A.; Ejsmont, K.; Kohout, M. *ChemPhysChem* **2016**, *17*, 2395–2406.

Bibliography

- [87] Genoni, A.; Dos Santos, L. H. R.; Meyer, B.; Macchi, P. *IUCrJ* **2017**, *4*, 136–146.
- [88] Almbladh, C. O.; Pedroza, A. C. *Phys. Rev. A* **1984**, *29*, 2322–2330.
- [89] Kohout, M.; Savin, A. *J. Comput. Chem.* **1997**, *18*, 1431–1439.
- [90] Gadre, S. R.; Kulkarni, S. A.; Pathak, R. K. *J. Chem. Phys.* **1993**, *98*, 3574–3576.
- [91] Alonso, J.; Girifalco, L. *Solid State Commun.* **1977**, *24*, 135–138.
- [92] Fuentealba, P. *Int. J. Quantum Chem.* **1998**, *69*, 559–565.
- [93] Tsirelson, V.; Stash, A. *Chem. Phys. Lett.* **2002**, *351*, 142–148.
- [94] Ayers, P. W. *J. Chem. Sci.* **2005**, *117*, 441–454.
- [95] Silvi, B. *J. Phys. Chem. A* **2003**, *107*, 3081–3085.
- [96] Matito, E.; Silvi, B.; Duran, M.; Solà, M. *J. Chem. Phys.* **2006**, *125*, 24301.
- [97] Scemama, A.; Caffarel, M.; Chaudret, R.; Piquemal, J.-P. *J. Chem. Theory Comput.* **2011**, *7*, 618–624.
- [98] Feixas, F.; Matito, E.; Duran, M.; Solà, M.; Silvi, B. *J. Chem. Theory Comput.* **2010**, *6*, 2736–2742.
- [99] Kohout, M. *Int. J. Quantum Chem.* **2004**, *97*, 651–658.
- [100] Kohout, M.; Wagner, F. R.; Grin, Y. *Int. J. Quantum Chem.* **2006**, *106*, 1499–1507.
- [101] Kohout, M.; Wagner, F. R.; Grin, Y. *Theor. Chem. Acc.* **2008**, *119*, 413–420.
- [102] Wagner, F. R.; Bezugly, V.; Kohout, M.; Grin, Y. *Chem. - A Eur. J.* **2007**, *13*, 5724–5741.
- [103] Bezugly, V.; Wielgus, P.; Kohout, M.; Wagner, F. R. *J. Comput. Chem.* **2010**, 2273–2285.
- [104] Scemama, A.; Chaquin, P.; Caffarel, M. *J. Chem. Phys.* **2004**, *121*, 1725–1735.
- [105] Amador-Bedolla, C.; Salomón-Ferrer, R.; Lester, W. A.; Vázquez-Martínez, J. A.; Aspuru-Guzik, A. *J. Chem. Phys.* **2007**, *126*, 204308.
- [106] Ponec, R. *J. Math. Chem.* **1997**, *21*, 323–333.
- [107] Ponec, R.; Cooper, D. L. *J. Phys. Chem. A* **2007**, *111*, 11294–11301.
- [108] Ponec, R.; Duben, A. J. *J. Comput. Chem.* **1999**, *20*, 760.
- [109] Ponec, R.; Roithová, J. *Theor. Chem. Acc.* **2001**, *105*, 383–392.
- [110] Schmider, H. L.; Becke, A. D. *J. Mol. Struct. THEOCHEM* **2000**, *527*, 51–61.
- [111] Finzel, K. *Int. J. Quantum Chem.* **2014**, *114*, 1546–1558.
- [112] Jacobsen, H. *J. Comput. Chem.* **2009**, *30*, 1093–1102.
- [113] Jacobsen, H. *Dalt. Trans.* **2010**, *39*, 5426–5428.
- [114] Kohout, M.; Savin, A.; Preuss, H. *J. Chem. Phys.* **1991**, *95*, 1928–1942.
- [115] Nagy, A.; March, N. H. *Mol. Phys.* **1997**, *90*, 271–276.
- [116] Bohórquez, H. J.; Boyd, R. J. *J. Chem. Phys.* **2008**, *129*, 024110.
- [117] Nagy, Á.; Liu, S. *Phys. Lett. A* **2008**, *372*, 1654–1656.
- [118] Bohórquez, H. J.; Boyd, R. J. *Theor. Chem. Acc.* **2010**, *127*, 393–400.
- [119] Sahni, V.; Gruenebaum, J.; Perdew, J. P. *Phys. Rev. B* **1982**, *26*, 4371–4377.
- [120] Perdew, J. P.; Burke, K.; Ernzerhof, M. *Phys. Rev. Lett.* **1996**, *77*, 3865–3868.
- [121] Tognetti, V.; Cortona, P.; Adamo, C. *J. Chem. Phys.* **2008**, *128*, 034101.
- [122] Zupan, A.; Burke, K.; Ernzerhof, M.; Perdew, J. P. *J. Chem. Phys.* **1997**, *106*, 10184–10193.
- [123] Contreras-Garcia, J.; Johnson, E. R.; Keinan, S.; Chaudret, R.; Piquemal, J.-P.; Beratan, D. N.; Yang, W. *J. Chem. Theory Comput.* **2011**, *7*, 625–632.

- [124] Boto, R. A.; Contreras-Garcia, J.; Tierny, J.; Piquemal, J.-P. *Mol. Phys.* **2016**, *114*, 1406–1414.
- [125] Gillet, N.; Chaudret, R.; Contreras-Garcia, J.; Yang, W.; Silvi, B.; Piquemal, J.-P. *J. Chem. Theory Comput.* **2012**, *8*, 3993–3997.
- [126] Fang, D.; Chaudret, R.; Piquemal, J.-P.; Cisneros, G. A. *J. Chem. Theory Comput.* **2013**, *9*, 2156–2160.
- [127] de Silva, P.; Korchowiec, J.; Wesolowski, T. A. *J. Chem. Phys.* **2014**, *140*, 164301.
- [128] de Silva, P.; Korchowiec, J.; Ram J. S., N.; Wesolowski, T. A. *Chim. Int. J. Chem.* **2013**, *67*, 253–256.
- [129] Finzel, K. *Theor. Chem. Acc.* **2016**, *135*, 148.
- [130] de Silva, P.; Corminboeuf, C. *J. Chem. Phys.* **2015**, *143*, 111105.
- [131] Kato, T. *Commun. Pure Appl. Math.* **1957**, *10*, 151–177.
- [132] Morrell, M. M.; Parr, R. G.; Levy, M. *J. Chem. Phys.* **1975**, *62*, 549.
- [133] Marx, D.; Savin, A. *Angew. Chem. Int. Ed.* **1997**, *36*, 2077–2080.
- [134] de Silva, P.; Corminboeuf, C. *J. Chem. Phys.* **2015**, *142*, 074112.
- [135] Nicolaï, A.; Liu, H.; Petraglia, R.; Corminboeuf, C. *J. Phys. Chem. Lett.* **2015**, *6*, 4422–4428.
- [136] Gryn'ova, G.; Nicolaï, A.; Prlj, A.; Ollitrault, P.; Andrienko, D.; Corminboeuf, C. *J. Mater. Chem. C* **2017**, *5*, 350–361.
- [137] de Lima Batista, A. P.; de Oliveira-Filho, A. G. S.; Galembeck, S. E. *ChemistrySelect* **2017**, *2*, 4648–4654.
- [138] Cormanich, R. A.; Bühl, M.; Rittner, R. *Org. Biomol. Chem.* **2015**, *13*, 9206–9213.
- [139] Mebs, S. *Chem. Phys. Lett.* **2016**, *651*, 172–177.
- [140] Zheng, M.; Kuriappan, J. A.; Waller, M. P. *Int. J. Quantum Chem.* **2017**, *117*, e25336.
- [141] Fourré, I.; Silvi, B.; Chaquin, P.; Sevin, A. *J. Comput. Chem.* **1999**, *20*, 897–910.
- [142] Chevreau, H.; Moreira, I. d. P. R.; Silvi, B.; Illas, F. *J. Phys. Chem. A* **2001**, *105*, 3570–3577.
- [143] Villaume, S.; Fogarty, H. A.; Ottosson, H. *ChemPhysChem* **2008**, *9*, 257–64.
- [144] Dahlstrand, C.; Rosenberg, M.; Kilså, K.; Ottosson, H. *J. Phys. Chem. A* **2012**, *116*, 5008–5017.
- [145] Jara-Cortés, J.; Rocha-Rinza, T.; Hernández-Trujillo, J. *Comput. Theor. Chem.* **2015**, *1053*, 220–228.
- [146] Popelier, P. *Coord. Chem. Rev.* **2000**, *197*, 169–189.
- [147] Schmider, H. *J. Chem. Phys.* **1996**, *105*, 11134.
- [148] Wang, Y.-G.; Wiberg, K. B.; Werstiuk, N. H. *J. Phys. Chem. A* **2007**, *111*, 3592–601.
- [149] Ferro-Costas, D.; Pendas, A. M.; Gonzalez, L.; Mosquera, R. A. *Phys. Chem. Chem. Phys.* **2014**, *16*, 9249–9258.
- [150] Tognetti, V.; Joubert, L. *Theor. Chem. Acc.* **2016**, *135*, 124.
- [151] Kadantsev, E. S.; Schmider, H. L. *Int. J. Quantum Chem.* **2008**, *108*, 1–14.
- [152] Burnus, T.; Marques, M.; Gross, E. *Phys. Rev. A* **2005**, *71*, 010501.
- [153] Cullen, J.; Krykunov, M.; Ziegler, T. *Chem. Phys.* **2011**, *391*, 11–18.
- [154] Ziegler, T.; Krykunov, M.; Cullen, J. *J. Chem. Phys.* **2012**, *136*, 124107.
- [155] Baerends, E. J.; Gritsenko, O. V.; van Meer, R. *Phys. Chem. Chem. Phys.* **2013**, *15*, 16408–16425.

Bibliography

- [156] Luzanov, A. V.; Sukhorukov, A. A.; Umanskii, V. E. *Theor. Exp. Chem.* **1976**, *10*, 354–361.
- [157] Martin, R. L. *J. Chem. Phys.* **2003**, *118*, 4775.
- [158] Mayer, I. *Chem. Phys. Lett.* **2007**, *437*, 284–286.
- [159] Head-Gordon, M.; Grana, A. M.; Maurice, D.; White, C. A. *J. Phys. Chem.* **1995**, *99*, 14261–14270.
- [160] Plasser, F.; Bäppler, S. A.; Wormit, M.; Dreuw, A. *J. Chem. Phys.* **2014**, *141*, 024106.
- [161] Plasser, F.; Wormit, M.; Dreuw, A. *J. Chem. Phys.* **2014**, *141*, 024106.
- [162] Luzanov, A. V. *Russ. Chem. Rev.* **1980**, *49*, 1033–1048.
- [163] Luzanov, A. V.; Zhikol, O. A. *Int. J. Quantum Chem.* **2009**, *110*, 902–924.
- [164] Tognetti, V.; Morell, C.; Ayers, P. W.; Joubert, L.; Chermette, H. *Phys. Chem. Chem. Phys.* **2013**, *15*, 14465–14475.
- [165] Rosenberg, M.; Dahlstrand, C.; Kilså, K.; Ottosson, H. *Chem. Rev.* **2014**, *114*, 5379–5425.
- [166] Runge, E.; Gross, E. K. U. *Phys. Rev. Lett.* **1984**, *52*, 997–1000.
- [167] Chai, J.-D.; Head-Gordon, M. *Phys. Chem. Chem. Phys.* **2008**, *10*, 6615–6620.
- [168] Weigend, F.; Ahlrichs, R. *Phys. Chem. Chem. Phys.* **2005**, *7*, 3297–305.
- [169] Frisch, M. J. et al. Gaussian09 Revision D.01. 2009.
- [170] Bickelhaupt, F. M.; te Velde, G.; Bickelhaupt, F. M.; Baerends, E. J.; Fonseca Guerra, C.; van Gisbergen, S. J. A.; Snijders, J. G.; Ziegler, T. *J. Comput. Chem.* **2001**, *22*, 931–967.
- [171] Fonseca Guerra, C.; Snijders, J. G.; te Velde, G.; Baerends, E. J. *Theor. Chem. Acc.* **1998**, *99*, 391–403.
- [172] ADF2013, SCM, Theoretical Chemistry, Vrije Universiteit, Amsterdam, The Netherlands, <http://www.scm.com>.
- [173] Becke, A. D. *J. Chem. Phys.* **1993**, *98*, 5648.
- [174] Van Lenthe, E.; Baerends, E. J. *J. Comput. Chem.* **2003**, *24*, 1142–56.
- [175] Wiberg, K. B.; Hadad, C. M.; LePage, T. J.; Breneman, C. M.; Frisch, M. J. *J. Phys. Chem.* **1992**, *96*, 671–679.
- [176] Henderson, A.; Ahrens, J.; Law, C. *The ParaView Guide ; Kitware Clifton Park, NY*; 2004.
- [177] ADF2016, SCM, Theoretical Chemistry, Vrije Universiteit, Amsterdam, The Netherlands, <http://www.scm.com>.
- [178] Roos, B.; Malmqvist, P.-A.; Molina, V.; Serrano-Andres, L.; Merchan, M. *J. Chem. Phys.* **2002**, *116*, 7526.
- [179] Li, X.; Paldus, J. *J. Phys. Chem. A* **2010**, *114*, 8591–8600.
- [180] Barbatti, M.; Pittner, J.; Pederzoli, M.; Werner, U.; Mitrić, R.; Bonačić-Koutecký, V.; Lischka, H. *Chem. Phys.* **2010**, *375*, 26–34.
- [181] Adamo, C.; Barone, V. *J. Chem. Phys.* **1999**, *110*, 6158.
- [182] Christiansen, O.; Gauss, J.; Stanton, J. F.; Jorgensen, P. *J. Chem. Phys.* **1999**, *111*, 525.
- [183] Baird, N. C. *J. Am. Chem. Soc.* **1972**, *94*, 4941–4948.
- [184] Samanta, A.; Devadoss, C.; Fessenden, R. W. *Chem. Phys. Lett.* **1990**, *169*, 421–426.
- [185] Maksic, Z. B.; Kovacek, D.; Eckert-Maksic, M.; Bockmann, M.; Klessinger, M. *J. Phys. Chem.* **1995**, *99*, 6410–6416.
- [186] Stanger, A. *J. Am. Chem. Soc.* **1991**, *113*, 8277–8280.
- [187] Steiner, E.; Fowler, P. W. *Int. J. Quantum Chem.* **1996**, *60*, 609–616.

- [188] Steinmann, S. N.; Jana, D. E.; Wu, J. I.-C.; Schleyer, P. v. R.; Mo, Y.; Corminboeuf, C. *Angew. Chem. Int. Ed. Engl.* **2009**, *48*, 9828–33.
- [189] Winnik, F. M. *Chem. Rev.* **1993**, *93*, 587–614.
- [190] Birks, J. *Photophysics of Aromatic Molecules*; Wiley, London, 1970.
- [191] Parac, M.; Grimme, S. *Chem. Phys.* **2003**, *292*, 11–21.
- [192] Amicangelo, J. C. *J. Phys. Chem. A* **2005**, *109*, 9174–82.
- [193] Rocha-Rinza, T.; De Vico, L.; Veryazov, V.; Roos, B. O. *Chem. Phys. Lett.* **2006**, *426*, 268–272.
- [194] Huenerbein, R.; Grimme, S. *Chem. Phys.* **2008**, *343*, 362–371.
- [195] Rocha-Rinza, T.; Christiansen, O. *Chem. Phys. Lett.* **2009**, *482*, 44–49.
- [196] Shirai, S.; Iwata, S.; Tani, T.; Inagaki, S. *J. Phys. Chem. A* **2011**, *115*, 7687–99.
- [197] Diri, K.; Krylov, A. I. *J. Phys. Chem. A* **2012**, *116*, 653–62.
- [198] Kołaski, M.; Arunkumar, C. R.; Kim, K. S. *J. Chem. Theory Comput.* **2013**, *9*, 847–856.
- [199] Peach, M. J. G.; Benfield, P.; Helgaker, T.; Tozer, D. J. *J. Chem. Phys.* **2008**, *128*, 044118.
- [200] Le Bahers, T.; Adamo, C.; Ciofini, I. *J. Chem. Theory Comput.* **2011**, *7*, 2498–2506.
- [201] Guido, C. A.; Cortona, P.; Mennucci, B.; Adamo, C. *J. Chem. Theory Comput.* **2013**, *9*, 3118–3126.
- [202] Guido, C. A.; Cortona, P.; Adamo, C. *J. Chem. Phys.* **2014**, *140*, 104101.
- [203] Etienne, T.; Assfeld, X.; Monari, A. *J. Chem. Theory Comput.* **2014**, *10*, 3906–3914.
- [204] Adamo, C.; Le Bahers, T.; Savarese, M.; Wilbraham, L.; García, G.; Fukuda, R.; Ehara, M.; Rega, N.; Ciofini, I. *Coord. Chem. Rev.* **2015**, *304–305*, 166–178.
- [205] Frey, J.; Curchod, B. F. E.; Scopelliti, R.; Tavernelli, I.; Rothlisberger, U.; Nazeeruddin, M. K.; Baranoff, E. *Dalt. Trans.* **2014**, *43*, 5667–5679.
- [206] Jiao, L.; Yu, C.; Wang, J.; Briggs, E. A.; Besley, N. A.; Robinson, D.; Ruedas-Rama, M. J.; Orte, A.; Crovetto, L.; Talavera, E. M.; Alvarez-Pez, J. M.; Van der Auweraer, M.; Boens, N. *RSC Adv.* **2015**, *5*, 89375–89388.
- [207] Prlj, A.; Vannay, L.; Corminboeuf, C. *Helv. Chim. Acta* **2017**, *100*, e1700093.
- [208] Anderson, J. S. M.; Melin, J.; Ayers, P. W. *J. Chem. Theory Comput.* **2007**, *3*, 358–374.
- [209] Bultinck, P.; Van Alsenoy, C.; Ayers, P. W.; Carbó-Dorca, R. *J. Chem. Phys.* **2007**, *126*, 144111.
- [210] Alvarez, S.; Hoffmann, R.; Mealli, C. *Chem. - A Eur. J.* **2009**, *15*, 8358–8373.
- [211] Ball, P. *Nature* **2011**, *469*, 26–28.
- [212] von Schleyer, P. R.; Jiao, H. *Pure Appl. Chem.* **1996**, *68*, 209–218.
- [213] Jansen, M.; Wedig, U. *Angew. Chem. Int. Ed.* **2008**, *47*, 10026–10029.
- [214] Schmider, H. L.; Becke, A. D. *J. Chem. Phys.* **2002**, *116*, 3184.
- [215] Bader, R. F. W.; Essén, H. *J. Chem. Phys.* **1984**, *80*, 1943–1960.
- [216] Vannay, L.; Meyer, B.; Guillot, B.; Corminboeuf, C. *The Interplay between Covalent bonding Patterns and Non-Covalent Interactions in Biscarbonyl[14] Annulene under Pressure, in preparation.*
- [217] Tiana, D.; Francisco, E.; Macchi, P.; Sironi, A.; Martín Pendás, A. *J. Phys. Chem. A* **2015**, *119*, 2153–2160.

Bibliography

- [218] Butovskii, M. V.; Döring, C.; Bezugly, V.; Wagner, F. R.; Grin, Y.; Kempe, R. *Nat. Chem.* **2010**, *2*, 741–744.
- [219] Vidal, I.; Melchor, S.; Dobado, J. A. *J. Phys. Chem. A* **2005**, *109*, 7500–7508.
- [220] Tiana, D.; Francisco, E.; Blanco, M. A.; Macchi, P.; Sironi, A.; Martin Pendas, A. *J. Chem. Theory Comput.* **2010**, *6*, 1064–1074.
- [221] Sánchez-Sanz, G.; Trujillo, C.; Solimannejad, M.; Alkorta, I.; Elguero, J. *Phys. Chem. Chem. Phys.* **2013**, *15*, 14310–14318.
- [222] Fradera, X.; Austen, M. A.; Bader, R. F. W. *J. Phys. Chem. A* **1999**, *103*, 304–314.
- [223] Cortesguzman, F.; Bader, R. *Coord. Chem. Rev.* **2005**, *249*, 633–662.
- [224] Amezaga, N. J. M.; Pamies, S. C.; Peruchena, N. M.; Sosa, G. L. *J. Phys. Chem. A* **2010**, *114*, 552–562.
- [225] Syzgantseva, O. A.; Tognetti, V.; Joubert, L. *J. Phys. Chem. A* **2013**, *117*, 8969–8980.
- [226] Bartashevich, E. V.; Pendas, A. M.; Tsirelson, V. G. *Phys. Chem. Chem. Phys.* **2014**, *16*, 16780–16789.
- [227] Johansson, M. P.; Swart, M. *Phys. Chem. Chem. Phys.* **2013**, *15*, 11543–11553.
- [228] Polo, V.; Andres, J.; Castillo, R.; Berski, S.; Silvi, B. *Chem. - A Eur. J.* **2004**, *10*, 5165–5172.
- [229] Berski, S.; Andrés, J.; Silvi, B.; Domingo, L. R. *J. Phys. Chem. A* **2006**, *110*, 13939–13947.
- [230] Kalinowski, J.; Berski, S.; Gordon, A. J. *J. Phys. Chem. A* **2011**, *115*, 13513–13522.
- [231] Lee, R.; Gryn'ova, G.; Ingold, K. U.; Coote, M. L. *Phys. Chem. Chem. Phys.* **2016**, *18*, 23673–23679.
- [232] Polo, V.; Andres, J.; Berski, S.; Domingo, L. R.; Silvi, B. *J. Phys. Chem. A* **2008**, *112*, 7128–7136.
- [233] Chaudry, U. A.; Popelier, P. L. A. *J. Phys. Chem. A* **2003**, *107*, 4578–4582.
- [234] Andrés, J.; Gracia, L.; González-Navarrete, P.; Safont, V. S. *Comput. Theor. Chem.* **2015**, *1053*, 17–30.
- [235] Chattaraj, P. K.; Roy, D. R.; Elango, M.; Subramanian, V. *J. Phys. Chem. A* **2005**, *109*, 9590–9597.
- [236] Bürgi, T.; Baiker, A. *J. Am. Chem. Soc.* **1998**, *120*, 12920–12926.
- [237] Feringa, B. L.; Koumura, N.; Zijlstra, R. W. J.; van Delden, R. A.; Harada, N. *Nature* **1999**, *401*, 152–155.
- [238] Ashton, P. R.; Ballardini, R.; Balzani, V.; Credi, A.; Dress, K. R.; Ishow, E.; Kleverlaan, C. J.; Kocian, O.; Preece, J. A.; Spencer, N.; Stoddart, J. F.; Venturi, M.; Wenger, S. *Chem. - A Eur. J.* **2000**, *6*, 3558–3574.
- [239] Shin, J.-S.; Pierce, N. A. *J. Am. Chem. Soc.* **2004**, *126*, 10834–10835.
- [240] Holland, N. B.; Hugel, T.; Neuert, G.; Cattani-Scholz, A.; Renner, C.; Oesterheld, D.; Moroder, L.; Seitz, M.; Gaub, H. E. *Macromolecules* **2003**, *36*, 2015–2023.
- [241] Russew, M.-M.; Hecht, S. *Adv. Mater.* **2010**, *22*, 3348–3360.
- [242] Beharry, A. A.; Woolley, G. A. *Chem. Soc. Rev.* **2011**, *40*, 4422–4437.
- [243] Tian, H.; Yang, S. *Chem. Soc. Rev.* **2004**, *33*, 85–97.
- [244] Krokidis, X.; Noury, S.; Silvi, B. *J. Phys. Chem. A* **1997**, *101*, 7277–7282.
- [245] Krokidis, X.; Silvi, B.; Alikhani, M. *Chem. Phys. Lett.* **1998**, *292*, 35–45.
- [246] Thom, R. *Nature* **1977**, *270*, 658–658.

- [247] Andres, J.; Berski, S.; R. Domingo, L.; Polo, V.; Silvi, B. *Curr. Org. Chem.* **2011**, *15*, 3566–3575.
- [248] Andrés, J.; González-Navarrete, P.; Safont, V. S. *Int. J. Quantum Chem.* **2014**, *114*, 1239–1252.
- [249] Wu, P.; Chaudret, R.; Hu, X.; Yang, W. *J. Chem. Theory Comput.* **2013**, *9*, 2226–2234.
- [250] Joubert, L.; Pavone, M.; Barone, V.; Adamo, C. *J. Chem. Theory Comput.* **2006**, *2*, 1220–1227.
- [251] Mashraqui, S. H.; Sangvikar, Y. S.; Meetsma, A. *Tetrahedron Lett.* **2006**, *47*, 5599–5602.
- [252] Brémond, É.; Golubev, N.; Steinmann, S. N.; Corminboeuf, C. *J. Chem. Phys.* **2014**, *140*, 18A516.
- [253] Petraglia, R.; Nicolai, A.; Wodrich, M. D.; Ceriotti, M.; Corminboeuf, C. *J. Comput. Chem.* **2016**, *37*, 83–92.
- [254] Perez-Estrada, S.; Rodriguez-Molina, B.; Xiao, L.; Santillan, R.; Jimenez-Oses, G.; Houk, K. N.; Garcia-Garibay, M. A. *J. Am. Chem. Soc.* **2015**, *137*, 2175–2178.
- [255] Maciejewski, J.; Sobczuk, A.; Claveau, A.; Nicolai, A.; Petraglia, R.; Cervini, L.; Baudat, E.; Miéville, P.; Fazzi, D.; Corminboeuf, C.; Sforazzini, G. *Chem. Sci.* **2017**, *8*, 361–365.
- [256] Elstner, M.; Porezag, D.; Jungnickel, G.; Elsner, J.; Haugk, M.; Frauenheim, T.; Suhai, S.; Seifert, G. *Phys. Rev. B* **1998**, *58*, 7260–7268.
- [257] Porezag, D.; Frauenheim, T.; Köhler, T.; Seifert, G.; Kaschner, R. *Phys. Rev. B* **1995**, *51*, 12947–12957.
- [258] Yang, Y.; Yu, H.; York, D.; Cui, Q.; Elstner, M. *J. Phys. Chem. A* **2007**, *111*, 10861–10873.
- [259] Petraglia, R.; Nicolai, A.; Wodrich, M. D.; Ceriotti, M.; Corminboeuf, C. *J. Comput. Chem.* **2016**, *37*, 83–92.
- [260] Aradi, B.; Hourahine, B.; Frauenheim, T. *J. Phys. Chem. A* **2007**, *111*, 5678–5684.
- [261] Sugita, Y.; Okamoto, Y. *Chem. Phys. Lett.* **1999**, *314*, 141–151.
- [262] Ceriotti, M.; More, J.; Manolopoulos, D. E. *Comput. Phys. Commun.* **2014**, *185*, 1019–1026.
- [263] Ceriotti, M.; Bussi, G.; Parrinello, M. *J. Chem. Theory Comput.* **2010**, *6*, 1170–1180.
- [264] Gaus, M.; Goez, A.; Elstner, M. *J. Chem. Theory Comput.* **2013**, *9*, 338–354.
- [265] Gaus, M.; Lu, X.; Elstner, M.; Cui, Q. *J. Chem. Theory Comput.* **2014**, *10*, 1518–1537.
- [266] Dolgonos, G.; Aradi, B.; Moreira, N. H.; Frauenheim, T. *J. Chem. Theory Comput.* **2010**, *6*, 266–278.
- [267] Zubarev, D. Y.; Boldyrev, A. I. *J. Org. Chem.* **2008**, *73*, 9251–9258.
- [268] Foster, J. P.; Weinhold, F. *J. Am. Chem. Soc.* **1980**, *102*, 7211–7218.
- [269] Ceriotti, M.; Tribello, G. A.; Parrinello, M. *Proc. Natl. Acad. Sci.* **2011**, *108*, 13023–13028.
- [270] Ceriotti, M.; Tribello, G. A.; Parrinello, M. *J. Chem. Theory Comput.* **2013**, *9*, 1521–1532.
- [271] Tribello, G. A.; Ceriotti, M.; Parrinello, M. *Proc. Natl. Acad. Sci.* **2012**, *109*, 5196–5201.
- [272] Bashir, A.; Heck, A.; Narita, A.; Feng, X.; Nefedov, A.; Rohwerder, M.; Müllen, K.; Elstner, M.; Wöll, C. *Phys. Chem. Chem. Phys.* **2015**, *17*, 21988–21996.
- [273] Gleiter, R., H. H. *Modern Cyclophane Chemistry*; Wiley-VCH, 2004.
- [274] Garcia-Garibay, M. A. *Proc. Natl. Acad. Sci.* **2005**, *102*, 10771–10776.
- [275] Nawara, A. J.; Shima, T.; Hampel, F.; Gladysz, J. A. *J. Am. Chem. Soc.* **2006**, *128*, 4962–4963.

Bibliography

- [276] Hawthorne, M. F. *Science* **2004**, 303, 1849–1851.
- [277] Rapenne, G. *Org. Biomol. Chem.* **2005**, 3, 1165–1169.
- [278] Kottas, G. S.; Clarke, L. I.; Horinek, D.; Michl, J. *Chem. Rev.* **2005**, 105, 1281–1376.
- [279] Wold, S.; Esbensen, K.; Geladi, P. *Chemom. Intell. Lab. Syst.* **1987**, 2, 37–52.
- [280] Sittel, F.; Jain, A.; Stock, G. *J. Chem. Phys.* **2014**, 141, 014111.
- [281] Garcia, A. E. *Phys. Rev. Lett.* **1992**, 68, 2696–2699.
- [282] Tenenbaum, J. B. *Science* **2000**, 290, 2319–2323.
- [283] Belkin, M.; Niyogi, P. *Neural Comput.* **2003**, 15, 1373–1396.
- [284] Roweis, S. T. *Science* **2000**, 290, 2323–2326.
- [285] Ardevol, A.; Tribello, G. A.; Ceriotti, M.; Parrinello, M. *J. Chem. Theory Comput.* **2015**, 11, 1086–1093.
- [286] De, S.; Bartók, A. P.; Csányi, G.; Ceriotti, M. *Phys. Chem. Chem. Phys.* **2016**, 18, 13754–13769.
- [287] De, S.; Musil, F.; Ingram, T.; Baldauf, C.; Ceriotti, M. *J. Cheminform.* **2017**, 9, 1–14.
- [288] Rozel, A. B.; Golabek, G. J.; Jain, C.; Tackley, P. J.; Gerya, T. *Nature* **2017**, 545, 332–335.
- [289] Ohta, K.; Kuwayama, Y.; Hirose, K.; Shimizu, K.; Ohishi, Y. *Nature* **2016**, 534, 95–98.
- [290] Nishi, M.; Kuwayama, Y.; Tsuchiya, J.; Tsuchiya, T. *Nature* **2017**, 547, 205–208.
- [291] Algara-Siller, G.; Lehtinen, O.; Wang, F. C.; Nair, R. R.; Kaiser, U.; Wu, H. A.; Geim, A. K.; Grigorieva, I. V. *Nature* **2015**, 519, 443–445.
- [292] Bertrand, T.; Forget, F. *Nature* **2016**, 540, 86–89.
- [293] Huang, Q.; Yu, D.; Xu, B.; Hu, W.; Ma, Y.; Wang, Y.; Zhao, Z.; Wen, B.; He, J.; Liu, Z.; Tian, Y. *Nature* **2014**, 510, 250–253.
- [294] Tian, Y.; Xu, B.; Yu, D.; Ma, Y.; Wang, Y.; Jiang, Y.; Hu, W.; Tang, C.; Gao, Y.; Luo, K.; Zhao, Z.; Wang, L.-M.; Wen, B.; He, J.; Liu, Z. *Nature* **2013**, 493, 385–388.
- [295] Palasyuk, T.; Troyan, I.; Eremets, M.; Drozd, V.; Medvedev, S.; Zaleski-Ejgierd, P.; Magos-Palasyuk, E.; Wang, H.; Bonev, S. A.; Dudenko, D.; Naumov, P. *Nat. Commun.* **2014**, 5.
- [296] Bini, R.; Ceppatelli, M.; Citroni, M.; Schettino, V. *Chem. Phys.* **2012**, 398, 262–268.
- [297] Paliwoda, D.; Kowalska, K.; Hanfland, M.; Katrusiak, A. *J. Phys. Chem. Lett.* **2013**, 4, 4032–4037.
- [298] Li, Q.; Ma, Y.; Oganov, A. R.; Wang, H.; Wang, H.; Xu, Y.; Cui, T.; Mao, H.-K.; Zou, G. *Phys. Rev. Lett.* **2009**, 102, 175506.
- [299] Pickard, C. J.; Salamat, A.; Bojdys, M. J.; Needs, R. J.; McMillan, P. F. *Phys. Rev. B* **2016**, 94, 094104.
- [300] Zhang, L.; Wang, Y.; Lv, J.; Ma, Y. *Nat. Rev. Mater.* **2017**, 2, 17005–17021.
- [301] Hemley, R. J. *Annu. Rev. Phys. Chem.* **2000**, 51, 763–800.
- [302] McMillan, P. F. *Chem. Soc. Rev.* **2006**, 35, 855–857.
- [303] Grochala, W.; Hoffmann, R.; Feng, J.; Ashcroft, N. W. *Angew. Chem. Int. Ed.* **2007**, 46, 3620–3642.
- [304] Chen, X.-J.; Struzhkin, V. V.; Yu, Y.; Goncharov, A. F.; Lin, C.-T.; Mao, H.-k.; Hemley, R. J. *Nature* **2010**, 466, 950–953.
- [305] Prakash, O.; Kumar, A.; Thamizhavel, A.; Ramakrishnan, S. *Science* **2017**, 355, 52–55.

- [306] Sun, L. et al. *Nature* **2012**, 483, 67–69.
- [307] Errea, I.; Calandra, M.; Pickard, C. J.; Nelson, J. R.; Needs, R. J.; Li, Y.; Liu, H.; Zhang, Y.; Ma, Y.; Mauri, F. *Nature* **2016**, 532, 81–84.
- [308] Drozdov, A. P.; Eremets, M. I.; Troyan, I. A.; Ksenofontov, V.; Shylin, S. I. *Nature* **2015**, 525, 73–76.
- [309] Li, Y.-L.; Wang, S.-N.; Oganov, A. R.; Gou, H.; Smith, J. S.; Strobel, T. A. *Nat. Commun.* **2015**, 6, 6974.
- [310] Dong, X. et al. *Nat. Chem.* **2017**, 9, 440–445.
- [311] Yang, G.; Wang, Y.; Peng, F.; Bergara, A.; Ma, Y. *J. Am. Chem. Soc.* **2016**, 138, 4046–4052.
- [312] Botana, J.; Wang, X.; Hou, C.; Yan, D.; Lin, H.; Ma, Y.; Miao, M.-s. *Angew. Chem. Int. Ed.* **2015**, 54, 9280–9283.
- [313] Eremets, M. I.; Gavriliuk, A. G.; Trojan, I. A.; Dzivenko, D. A.; Boehler, R. *Nat. Mater.* **2004**, 3, 558–563.
- [314] Lipp, M. J.; Evans, W. J.; Baer, B. J.; Yoo, C.-S. *Nat. Mater.* **2005**, 4, 211–215.
- [315] Santoro, M.; Gorelli, F. A. *Chem. Soc. Rev.* **2006**, 35, 918.
- [316] Pickard, C. J.; Needs, R. J. *Nat. Mater.* **2008**, 7, 775–779.
- [317] Wang, Y.; Liu, H.; Lv, J.; Zhu, L.; Wang, H.; Ma, Y. *Nat. Commun.* **2011**, 2, 563.
- [318] Ghiringhelli, G. et al. *Science* **2012**, 337, 821–825.
- [319] Zhang, M.; Liu, H.; Li, Q.; Gao, B.; Wang, Y.; Li, H.; Chen, C.; Ma, Y. *Phys. Rev. Lett.* **2015**, 114.
- [320] Zhao, Z.; Xu, B.; Tian, Y. *Annu. Rev. Mater. Res.* **2016**, 46, 383–406.
- [321] Peng, F.; Yao, Y.; Liu, H.; Ma, Y. *J. Phys. Chem. Lett.* **2015**, 6, 2363–2366.
- [322] Spaulding, D. K.; Weck, G.; Loubeyre, P.; Datchi, F.; Dumas, P.; Hanfland, M. *Nat. Commun.* **2014**, 5, 5739.
- [323] Song, Y. *Phys. Chem. Chem. Phys.* **2013**, 15, 14524–14547.
- [324] Pepin, C. M.; Dewaele, A.; Geneste, G.; Loubeyre, P.; Mezouar, M. *Phys. Rev. Lett.* **2014**, 113.
- [325] Scheler, T.; Marqués, M.; Konôpková, Z.; Guillaume, C. L.; Howie, R. T.; Gregoryanz, E. *Phys. Rev. Lett.* **2013**, 111.
- [326] Resnati, G.; Boldyreva, E.; Bombicz, P.; Kawano, M. *IUCrJ* **2015**, 2, 675–690.
- [327] Hejny, C.; Minkov, V. S. *IUCrJ* **2015**, 2, 218–229.
- [328] Patyk, E.; Skumiel, J.; Podsiadlo, M.; Katrusiak, A. *Angew. Chem. Int. Ed.* **2012**, 51, 2146–2150.
- [329] Gajda, R.; Katrusiak, A.; Crassous, J. *CrystEngComm* **2009**, 11, 2668–2676.
- [330] Dziubek, K. F.; Jeęczminski, D.; Katrusiak, A. *J. Phys. Chem. Lett.* **2010**, 1, 844–849.
- [331] Patyk, E.; Katrusiak, A. *Chem. Sci.* **2015**, 6, 1991–1995.
- [332] Patyk, E.; Jenczak, A.; Katrusiak, A. *Phys. Chem. Chem. Phys.* **2016**, 18, 11474–11479.
- [333] Podsiadlo, M.; Bujak, M.; Katrusiak, A. *CrystEngComm* **2012**, 14, 4496–4500.
- [334] Patyk-Kazmierczak, E.; Warren, M. R.; Allan, D. R.; Katrusiak, A. *Phys. Chem. Chem. Phys.* **2017**, 19, 9086–9091.
- [335] Cai, W.; Gladysiak, A.; Aniola, M.; Smith, V. J.; Barbour, L. J.; Katrusiak, A. *J. Am. Chem. Soc.* **2015**, 137, 9296–9301.

Bibliography

- [336] Andrzejewski, M.; Katrusiak, A. *J. Phys. Chem. Lett.* **2017**, *8*, 279–284.
- [337] Pinkowicz, D.; Rams, M.; Mišek, M.; Kamenev, K. V.; Tomkowiak, H.; Katrusiak, A.; Sieklucka, B. *J. Am. Chem. Soc.* **2015**, *137*, 8795–8802.
- [338] Andrzejewski, M.; Katrusiak, A. *J. Phys. Chem. Lett.* **2017**, *8*, 929–935.
- [339] Szafranski, M.; Katrusiak, A. *J. Phys. Chem. Lett.* **2016**, *7*, 3458–3466.
- [340] Szafranski, M.; Katrusiak, A. *J. Phys. Chem. Lett.* **2017**, *8*, 2496–2506.
- [341] Katrusiak, A.; Szafranski, M. *J. Am. Chem. Soc.* **2006**, *128*, 15775–15785.
- [342] Dziubek, K.; Podsiadlo, M.; Katrusiak, A. *J. Am. Chem. Soc.* **2007**, *129*, 12620–12621.
- [343] Minkov, V. S.; Boldyreva, E. V. *J. Phys. Chem. B* **2013**, *117*, 14247–14260.
- [344] Boldyreva, E. V.; Dmitriev, V.; Hancock, B. C. *Int. J. Pharm.* **2006**, *327*, 51–57.
- [345] Boldyreva, E.; Sowa, H.; Seryotkin, Y.; Drebuschak, T.; Ahsbahs, H.; Chernyshev, V.; Dmitriev, V. *Chem. Phys. Lett.* **2006**, *429*, 474–478.
- [346] Minkov, V. S.; Boldyreva, E. V.; Drebuschak, T. N.; Görbitz, C. H. *CrystEngComm* **2012**, *14*, 5943–5954.
- [347] Boldyreva, E. V. *Phase Transitions* **2009**, *82*, 303–321.
- [348] Sutton, C.; Risko, C.; Brédas, J.-L. *Chem. Mater.* **2016**, *28*, 3–16.
- [349] Scherer, W.; Dunbar, A. C.; Barquera-Lozada, J. E.; Schmitz, D.; Eickerling, G.; Kratzert, D.; Stalke, D.; Lanza, A.; Macchi, P.; Casati, N. P. M.; Ebad-Allah, J.; Kuntscher, C. *Angew. Chem. Int. Ed.* **2015**, *54*, 2505–2509.
- [350] Casati, N.; Macchi, P.; Sironi, A. *Chem. - A Eur. J.* **2009**, *15*, 4446–4457.
- [351] Boldyreva, E. V. *Acta Crystallogr. Sect. A Found. Crystallogr.* **2008**, *64*, 218–231.
- [352] Katrusiak, A. *Acta Crystallogr. Sect. A Found. Crystallogr.* **2008**, *64*, 135–148.
- [353] Macchi, P.; Casati, N. *Acta Crystallogr. A* **2011**, C163–C164.
- [354] Naumov, P.; Chizhik, S.; Panda, M. K.; Nath, N. K.; Boldyreva, E. *Chem. Rev.* **2015**, *115*, 12440–12490.
- [355] Boldyreva, E. V. *J. Mol. Struct.* **2003**, *647*, 159–179.
- [356] Boldyreva, E. V. *J. Mol. Struct.* **2004**, *700*, 151–155.
- [357] Tomkowiak, H.; Katrusiak, A. *J. Phys. Chem. C* **2017**, *34*, 18830–18836.
- [358] Neel, A. J.; Hilton, M. J.; Sigman, M. S.; Toste, F. D. *Nature* **2017**, *543*, 637–646.
- [359] Riley, K. E.; Hobza, P. *Acc. Chem. Res.* **2013**, *46*, 927–936.
- [360] Salonen, L. M.; Ellermann, M.; Diederich, F. *Angew. Chem. Int. Ed.* **2011**, *50*, 4808–4842.
- [361] Sutton, C.; Marshall, M. S.; Sherrill, C. D.; Risko, C.; Brédas, J.-L. *J. Am. Chem. Soc.* **2015**, *137*, 8775–8782.
- [362] Wheeler, S. E.; Houk, K. N. *J. Am. Chem. Soc.* **2008**, *130*, 10854–10855.
- [363] Parrish, R. M.; Sherrill, C. D. *J. Am. Chem. Soc.* **2014**, *136*, 17386–17389.
- [364] Wheeler, S. E. *J. Am. Chem. Soc.* **2011**, *133*, 10262–10274.
- [365] Wheeler, S. E. *Acc. Chem. Res.* **2013**, *46*, 1029–1038.
- [366] Wu, J. I.; Jackson, J. E.; Schleyer, P. v. R. *J. Am. Chem. Soc.* **2014**, *136*, 13526–13529.
- [367] Kakeshpour, T.; Wu, J. I.; Jackson, J. E. *J. Am. Chem. Soc.* **2016**, *138*, 3427–3432.
- [368] Kakeshpour, T.; Bailey, J. P.; Jenner, M. R.; Howell, D. E.; Staples, R. J.; Holmes, D.; Wu, J. I.; Jackson, J. E. *Angew. Chem. Int. Ed.* **33**, 9842–9846.
- [369] Wu, C.-H.; Ito, K.; Buytendyk, A.; Bowen, K. H.; Wu, J. I. *Biochemistry* **2017**,

- [370] Anand, M.; Fernández, I.; Schaefer, H. E.; Wu, J. I.-C. *J. Comput. Chem.* **2016**, *37*, 59–63.
- [371] Metrangolo, P.; Carcenac, Y.; Lahtinen, M.; Pilati, T.; Rissanen, K.; Vij, A.; Resnati, G. *Science* **2009**, *323*, 1461–1464.
- [372] Takezawa, H.; Murase, T.; Resnati, G.; Metrangolo, P.; Fujita, M. *J. Am. Chem. Soc.* **2014**, *136*, 1786–1788.
- [373] Yang, D.; Zhao, J.; Zhao, Y.; Lei, Y.; Cao, L.; Yang, X.-J.; Davi, M.; de Sousa Amadeu, N.; Janiak, C.; Zhang, Z.; Wang, Y.-Y.; Wu, B. *Angew. Chem. Int. Ed.* **2015**, *54*, 8658–8661.
- [374] Takezawa, H.; Murase, T.; Resnati, G.; Metrangolo, P.; Fujita, M. *Angew. Chem. Int. Ed.* **2015**, *54*, 8411–8414.
- [375] Beyeh, N. K.; Pan, F.; Rissanen, K. *Angew. Chem. Int. Ed.* **2015**, *127*, 7411–7415.
- [376] Caronna, T.; Liantonio, R.; Logothetis, T. A.; Metrangolo, P.; Pilati, T.; Resnati, G. *J. Am. Chem. Soc.* **2004**, *126*, 4500–4501.
- [377] Wilhelm, C.; Boyd, S. A.; Chawda, S.; Fowler, F. W.; Goroff, N. S.; Halada, G. P.; Grey, C. P.; Lauher, J. W.; Luo, L.; Martin, C. D.; Parise, J. B.; Tarabrella, C.; Webb, J. A. *J. Am. Chem. Soc.* **2008**, *130*, 4415–4420.
- [378] Rosi, N. L. *Science* **2006**, *312*, 1027–1030.
- [379] Saccone, M.; Dichiarante, V.; Forni, A.; Goulet-Hanssens, A.; Cavallo, G.; Vapaavuori, J.; Terraneo, G.; Barrett, C. J.; Resnati, G.; Metrangolo, P.; Priimagi, A. *J. Mater. Chem. C* **2015**, *3*, 759–768.
- [380] Presang, C.; Nguyen, H. L.; Horton, P. N.; Whitwood, A. C.; Bruce, D. W. *Chem. Commun.* **2008**, 6164–6166.
- [381] McAllister, L. J.; Präsang, C.; Wong, J. P.-W.; Thatcher, R. J.; Whitwood, A. C.; Donnio, B.; O'Brien, P.; Karadakov, P. B.; Bruce, D. W. *Chem. Commun.* **2013**, *49*, 3946.
- [382] Vanderkooy, A.; Taylor, M. S. *J. Am. Chem. Soc.* **2015**, *137*, 5080–5086.
- [383] Canevet, D.; Sallé, M.; Zhang, G.; Zhang, D.; Zhu, D. *Chem. Commun.* **2009**, 2245–2269.
- [384] Ranganathan, A.; El-Ghayoury, A.; Mézière, C.; Harté, E.; Clérac, R.; Batail, P. *Chem. Commun.* **2006**, 2878–2880.
- [385] Walter, S. M.; Kniep, F.; Rout, L.; Schmidtchen, F. P.; Herdtweck, E.; Huber, S. M. *J. Am. Chem. Soc.* **2012**, *134*, 8507–8512.
- [386] Jungbauer, S. H.; Walter, S. M.; Schindler, S.; Rout, L.; Kniep, F.; Huber, S. M. *Chem. Commun.* **2014**, *50*, 6281–6284.
- [387] Zhang, Z.; Schreiner, P. R. *Chem. Soc. Rev.* **2009**, *38*, 1187.
- [388] Wang, H.; Wang, W.; Jin, W. J. *Chem. Rev.* **2016**, *116*, 5072–5104.
- [389] Metrangolo, P.; Meyer, F.; Pilati, T.; Resnati, G.; Terraneo, G. *Angew. Chem. Int. Ed.* **2008**, *47*, 6114–6127.
- [390] Politzer, P.; Murray, J. S.; Clark, T. *Phys. Chem. Chem. Phys.* **2010**, *12*, 7748–7757.
- [391] Parisini, E.; Metrangolo, P.; Pilati, T.; Resnati, G.; Terraneo, G. *Chem. Soc. Rev.* **2011**, *40*, 2267.
- [392] Xu, K.; Ho, D. M.; Pascal Jr, R. A. *J. Am. Chem. Soc.* **1994**, *116*, 105–110.
- [393] Muller, M.; Albrecht, M.; Gossen, V.; Peters, T.; Hoffmann, A.; Raabe, G.; Valkonen, A.; Rissanen, K. *Chem. - A Eur. J.* **2010**, *16*, 12446–12453.

Bibliography

- [394] Metrangolo, P.; Murray, J. S.; Pilati, T.; Politzer, P.; Resnati, G.; Terraneo, G. *Cryst. Growth Des.* **2011**, *11*, 4238–4246.
- [395] Pavan, M. S.; Durga Prasad, K.; Guru Row, T. N. *Chem. Commun.* **2013**, 49, 7558.
- [396] Cametti, M.; Crousse, B.; Metrangolo, P.; Milani, R.; Resnati, G. *Chem. Soc. Rev.* **2012**, *41*, 31–42.
- [397] Henkel, S.; Costa, P.; Klute, L.; Sokkar, P.; Fernandez-Oliva, M.; Thiel, W.; Sanchez-Garcia, E.; Sander, W. *J. Am. Chem. Soc.* **2016**, *138*, 1689–1697.
- [398] Carlsson, A.-C. C.; Mehmeti, K.; Uhrbom, M.; Karim, A.; Bedin, M.; Puttreddy, R.; Kleinmaier, R.; Neverov, A. A.; Nekoueishahraki, B.; Gräfenstein, J.; Rissanen, K.; Erdélyi, M. *J. Am. Chem. Soc.* **2016**, *138*, 9853–9863.
- [399] Nicolas, I.; Barrière, F.; Jeannin, O.; Fourmigué, M. *Cryst. Growth Des.* **2016**, *16*, 2963–2971.
- [400] Aakeröy, C. B.; Wijethunga, T. K.; Desper, J.; Đaković, M. *Cryst. Growth Des.* **2015**, *15*, 3853–3861.
- [401] Aakeröy, C. B.; Wijethunga, T. K.; Desper, J.; Đaković, M. *Cryst. Growth Des.* **2016**, *16*, 2662–2670.
- [402] Mukherjee, A.; Desiraju, G. R. *IUCrJ* **2014**, *1*, 49–60.
- [403] Bragg, W. H.; Bragg, W. L. *Proc. R. Soc. A Math. Phys. Eng. Sci.* **1913**, *88*, 428–438.
- [404] Thomas, J. M. *Angew. Chem. Int. Ed.* **2012**, *51*, 12946–12958.
- [405] Thomas, J. M. *Nature* **2012**, *491*, 186–187.
- [406] Coppens, P. *Acta Crystallogr. Sect. A Found. Crystallogr.* **1998**, *54*, 779–788.
- [407] Coppens, P. *Angew. Chem. Int. Ed.* **2005**, *44*, 6810–6811.
- [408] Tse, J. S.; Klug, D. D.; Patchkovskii, S.; Ma, Y.; Dewhurst, J. K. *J. Phys. Chem. B* **2006**, *110*, 3721–3726.
- [409] Yamanaka, T.; Okada, T.; Nakamoto, Y. *Phys. Rev. B* **2009**, *80*, 094108.
- [410] Fabbiani, F. P. A.; Dittrich, B.; Pulham, C. R.; Warren, J. E. *Acta Crystallogr. Sect. A Found. Crystallogr.* **2011**, *67*, C376–C376.
- [411] Koritsanszky, T. S.; Coppens, P. *Chem. Rev.* **2001**, *101*, 1583–1628.
- [412] Jayatilaka, D.; Grimwood, D. *Acta Crystallogr. Sect. A Found. Crystallogr.* **2004**, *60*, 111–119.
- [413] Grabowsky, S.; Jayatilaka, D.; Mebs, S.; Luger, P. *Chem. - A Eur. J.* **2010**, *16*, 12818–12821.
- [414] Grabowsky, S.; Luger, P.; Buschmann, J.; Schneider, T.; Schirmeister, T.; Sobolev, A. N.; Jayatilaka, D. *Angew. Chem. Int. Ed.* **2012**, *51*, 6776–6779.
- [415] Jayatilaka, D.; Grimwood, D. J. *Acta Crystallogr. Sect. A Found. Crystallogr.* **2001**, *57*, 76–86.
- [416] Genoni, A. *J. Phys. Chem. Lett.* **2013**, *4*, 1093–1099.
- [417] Genoni, A. *J. Chem. Theory Comput.* **2013**, *9*, 3004–3019.
- [418] Genoni, A. *Acta Crystallogr. Sect. A Found. Adv.* **2017**, *73*, 312–316.
- [419] Saleh, G.; Lo Presti, L.; Gatti, C.; Ceresoli, D. *J. Appl. Crystallogr.* **2013**, *46*, 1513–1517.
- [420] Saleh, G.; Gatti, C.; Lo Presti, L.; Contreras-García, J. *Chem. - A Eur. J.* **2012**, *18*, 15523–15536.
- [421] Saleh, G.; Gatti, C.; Lo Presti, L. *Comput. Theor. Chem.* **2012**, *998*, 148–163.

- [422] Destro, R.; Merati, F. *Acta Crystallogr. Sect. B Struct. Sci.* **1995**, *51*, 559–570.
- [423] Casati, N.; Kleppe, A.; Jephcoat, A. P.; Macchi, P. *Nat. Commun.* **2016**, *7*, 10901.
- [424] Casati, N.; Genoni, A.; Meyer, B.; Krawczuk, A.; Macchi, P. *Acta Crystallogr. Sect. B Struct. Sci. Cryst. Eng. Mater.* **2017**, *73*, 584–597.
- [425] Chai, J.-D.; Head-Gordon, M. *Phys. Chem. Chem. Phys.* **2008**, *10*, 6615–6620.
- [426] Hansen, N. K.; Coppens, P. *Acta Crystallogr. Sect. A Cryst. Physics, Diffraction, Theor. Gen. Crystallogr.* **1978**, *34*, 909–921.
- [427] Humphrey, W.; Dalke, A.; Schulten, K. *J. Mol. Graph.* **1996**, *14*, 33–38.
- [428] Ayachit, U. *The ParaView Guide: A Parallel Visualization Application*; Kitware, Inc.: USA, 2015.
- [429] Kohout, M. *DGrid*; 2017.
- [430] Destro, R.; Pilati, T.; Simonetta, M. *Tetrahedron* **1980**, *36*, 3301–3304.
- [431] Scelta, D.; Ceppatelli, M.; Bini, R. *J. Chem. Phys.* **2016**, *145*, 164504.
- [432] Ray, P.; Gray, J. L.; Badding, J. V.; Lueking, A. D. *J. Phys. Chem. B* **2016**, *120*, 11035–11042.
- [433] Wen, X.-D.; Hoffmann, R.; Ashcroft, N. W. *J. Am. Chem. Soc.* **2011**, *133*, 9023–9035.
- [434] Fitzgibbons, T. C.; Guthrie, M.; Xu, E.-s.; Crespi, V. H.; Davidowski, S. K.; Cody, G. D.; Alem, N.; Badding, J. V. *Nat. Mater.* **2014**, *14*, 43–47.
- [435] Fanetti, S.; Citroni, M.; Bini, R. *J. Phys. Chem. B* **2011**, *115*, 12051–12058.
- [436] Fanetti, S.; Citroni, M.; Bini, R. *J. Phys. Chem. C* **2014**, *118*, 13764–13768.
- [437] Boldyreva, E.; Dera, P. *High-Pressure Crystallography, From Fundamental Phenomena to Technological Applications*; Springer, 2009.
- [438] Casati, N.; Macchi, P.; Sironi, A. *Chem. Commun.* **2009**, 2679.
- [439] Dittrich, B. *Acta Crystallogr. Sect. B Struct. Sci. Cryst. Eng. Mater.* **2017**, *73*, 325–329.
- [440] Kapustin, E. A.; Minkov, V. S.; Boldyreva, E. V. *Acta Crystallogr. Sect. B Struct. Sci. Cryst. Eng. Mater.* **2014**, *70*, 517–532.
- [441] Kapustin, E. A.; Minkov, V. S.; Boldyreva, E. V. *Phys. Chem. Chem. Phys.* **2015**, *17*, 3534–3543.
- [442] Vit, A.; Misson, L.; Blankenfeldt, W.; Seebeck, F. P. *Acta Crystallogr. Sect. F Struct. Biol. Commun.* **2014**, *70*, 676–680.
- [443] Vit, A.; Misson, L.; Blankenfeldt, W.; Seebeck, F. P. *ChemBioChem* **2015**, *16*, 119–125.
- [444] Nichols, D. A.; Hargis, J. C.; Sanishvili, R.; Jaishankar, P.; Defrees, K.; Smith, E. W.; Wang, K. K.; Prati, F.; Renslo, A. R.; Woodcock, H. L.; Chen, Y. *J. Am. Chem. Soc.* **2015**, *137*, 8086–8095.
- [445] Liebschner, D.; Elias, M.; Moniot, S.; Fournier, B.; Scott, K.; Jelsch, C.; Guillot, B.; Lecomte, C.; Chabrieàre, E. *J. Am. Chem. Soc.* **2009**, *131*, 7879–7886.
- [446] Fournier, B.; Bendeif, E.-E.; Guillot, B.; Podjarny, A.; Lecomte, C.; Jelsch, C. *J. Am. Chem. Soc.* **2009**, *131*, 10929–10941.
- [447] Ogata, H.; Nishikawa, K.; Lubitz, W. *Nature* **2015**, *520*, 571–574.
- [448] Hirano, Y.; Takeda, K.; Miki, K. *Nature* **2016**,
- [449] Medvedev, M. G.; Bushmarinov, I. S.; Sun, J.; Perdew, J. P.; Lyssenko, K. A. *Science* **2017**, *355*, 49–52.

Bibliography

- [450] Simon, C. M.; Kim, J.; Gomez-Gualdron, D. A.; Camp, J. S.; Chung, Y. G.; Martin, R. L.; Mercado, R.; Deem, M. W.; Gunter, D.; Haranczyk, M.; Sholl, D. S.; Snurr, R. Q.; Smit, B. *Energy Environ. Sci.* **2015**, *8*, 1190–1199.
- [451] Lee, Y.; Barthel, S. D.; Dłotko, P.; Moosavi, S. M.; Hess, K.; Smit, B. *Nat. Commun.* **2017**, *8*, 15396.
- [452] Maxwell, P.; Popelier, P. L. *Mol. Phys.* **2016**, *114*, 1304–1316.
- [453] Blanco, M. A.; Martín Pendás, A.; Francisco, E. *J. Chem. Theory Comput.* **2005**, *1*, 1096–1109.
- [454] Maxwell, P.; Pendas, A. M.; Popelier, P. L. A. *Phys. Chem. Chem. Phys.* **2016**, *18*, 20986–21000.
- [455] Matta, C. F. *J. Comput. Chem.* **2003**, *24*, 453–463.
- [456] Abramov, Y. A. *J. Phys. Chem. A* **2011**, *115*, 12809–12817.

Laurent Vannay

Curriculum Vitae

EPFL SB ISIC LCMD

CH-1015 Lausanne

+41 (77) 439 9194

lvannay@yahoo.fr

Birth date: August 24, 1987

Education

- 2013 – Now **Ph.D. in Theoretical Chemistry**, EPFL, Lausanne, Switzerland.
Title: “ Extending the Scope of the Density Overlap Region Indicator”
Director: Prof. Dr. C. Corminboeuf.
- 2011 – 2013 **M.Sc. in Chemistry**, University of Fribourg, Fribourg, Switzerland.
Orientation: Theoretical and Physical Chemistry.
Master Thesis: “Modelling Electronic Structure and Magnetic Behaviours of Clusters Containing Open Shell d-electrons Using LFDFT and Broken Symmetry Approaches”
Director: Prof. Dr. Claude A. E. Daul.
- 2006 – 2011 **B.Sc. in Chemistry, bilingual (french-german)**, EPFL and University of Fribourg, Lausanne and Fribourg, Switzerland.

Scientific Presentations

- 2016 **Talk** : “**Visualizing and quantifying molecular excited state interactions with DORI**”, *European Symposium on Chemical Bonding (ESCB1)*, Rouens, France.
- 2017 **Poster** : “**Bringing DORI to analyze and understand fluxional molecules**”, *WATOC*, Munich, Germany, and *STC*, Basel, Switzerland.
- 2014 **Poster** : “**Visualizing and quantifying molecular excited state interactions with scalar fields**”, *Swiss Chemical Society, Fall Meeting*, Zurich, Switzerland.

Teaching Experience

Lecturer

- 2017-now **Lecturer**, *General chemistry*, HEIG-VD, Yverdon-les-bains.

Teaching Assistant (>800h)

- 2014,2016 **Lecturer**, *Introduction to computational chemistry (high school)*, EPFL, Lausanne.
- 2017 **Lecturer**, *Introduction to computational chemistry (11 to 13 years old girls' camp)*, EPFL, Lausanne.
- 2016–2017 **Supervisor**, *Project of computational chemistry: DORI on experimental densities*, EPFL, Lausanne.
- 2015–2016 **Supervisor**, *Project in molecular sciences: Python scripting for geometrical construction of molecular electronics*, EPFL, Lausanne.
- 2015–2016 **Supervisor**, *Project of computational chemistry: Python scripting for input/output management*, EPFL, Lausanne.

- 2014–2015 **Supervisor**, *Interdisciplinary project for chemical master: Protein modifications effects on ligand docking*, EPFL, Lausanne.
- 2015–2016 **Preparation of the practical work “Chemistry Laboratory Work II: Structure and chemical bonding”**, EPFL, Lausanne.
- 2013–2017 **Assistant**, *Lecture : “Atoms, ions, molecules and functions”*, EPFL, Lausanne.
- 2013–2014 **Assistant**, *Lecture : “Advanced general chemistry”*, EPFL, Lausanne.
- 2013–2014 **Assistant**, *Lecture : “Introduction to organic chemistry I”*, EPFL, Lausanne.
- 2013–2016 **Assistant**, *Lecture : “Coordination chemistry”*, EPFL, Lausanne.
- 2014–2016 **Assistant**, *Practical work : “Chemistry laboratory work II”*, EPFL, Lausanne.
- 2012–2014 **Assistant**, *Practical work : “General chemistry”*, University of Fribourg, Fribourg.
- 2013–2014 **Assistant**, *assigned private teacher for T. Worley (ski world champion 2013, 2017)*, University of Fribourg, Fribourg.

Awards & Grants

- 2017 **Teaching Excellence Award**, EPFL.
- 2014 **Teaching Excellence Award**, EPFL.
- 2013 **BASF award**, *Best Average Grade In Chemistry (Master)*, University of Fribourg.
- 2013 **COST Short Term Scientific Mission**, *Theoretical chemistry*, Paristech, Paris.

Languages

- French Native speaker
- English Fluent (oral, writing)
- German Excellent command (oral, writing)
- Spanish Excellent command (oral)

Computer Skills

- Modelization Gaussian, ADF, Gamess, Q-Chem, Turbomole, Molpro, DGRID
- Visualization VMD, Paraview, CloudCompare, Meshlab
- Editing Blender, Gimp, Inkscape
- Coding Python, C++, Matlab, Bash, sed, awk
- Workstations hardware build, installation/management of operating systems: Windows (XP, 7, 10), Linux (Ubuntu, Mint, Debian)

Publications

1. L. Vannay, B. Meyer, B. Guillot and C. Corminboeuf. *The Interplay between Covalent Bonding Patterns and Non-Covalent Interactions in Biscarbonyl[14] Annulene under Pressure* in preparation.
2. L. Rivier, L. Vannay, M. A. Mendez, P. Peljo, H. Vrubel, C. Corminboeuf, M. D. Scanlon, and H. Girault. *Photo-generation of Hydrogen by Decamethylruthenocene: a non-sacrificial electron donor and sensitizer* in preparation.
3. L. Vannay, B. Meyer, R. Petraglia, G. Sforazzini, M. Ceriotti and C. Corminboeuf. *Analyzing*

Fluxional Molecules using DORI submitted.

4. L. Peterhans, E. Alloa, Y. Sheima, L. Vannay, M. Leclerc, C. Corminboeuf, S. C. Hayes and N. Banerji. *Salt-Induced Thermochromism of a Conjugated Polyelectrolyte*. Phys. Chem. Chem. Phys., **2017**, 19, 28853
5. A. Prlj, L. Vannay and C. Corminboeuf, *Fluorescence Quenching in BODIPY Dyes: The Role of Intramolecular Interactions and Charge Transfer* Helv. Chim. Acta, **2017**, 100, e1700093
6. L. Rivier, P. Peljo, L. Vannay, G. C. Gschwend, M. A. Mendez, C. Corminboeuf, M. D. Scanlon and H. H. Girault. *Photoproduction of Hydrogen by Decamethylruthenocene Combined with Electrochemical Recycling* Angew. Chemie Int. Ed., **2017**, 56, 2324.
7. L. Y. M. Eymann, A. G. Tskhovrebov, A. Sienkiewicz, J. L. Bila, I. Zivkovic, H. M. Ronnow, M. D. Wodrich, L. Vannay, C. Corminboeuf, P. Pattison, E. Solari, R. Scopelliti and K. Severin. *Neutral Aminyl Radicals Derived from Azoimidazolium Dyes* J. Am. Chem. Soc., **2016**, 138, 15126.
8. L. Vannay, E. Bremond, P. de Silva and C. Corminboeuf, *Visualizing and Quantifying Interactions in the Excited State*, Chem. - A Eur. J., **2016**, 22, 18442

Interests

Sports Jive and acrobatic Rock'n Roll (dancer and teacher), alpinism
Hobbies Piano